Research in Astron. Astrophys. **2012** Vol. **12** No. **10**, 1313–1380
http://www.raa-journal.org *http://www.iop.org/journals/raa*

Research in Astronomy and Astrophysics

INVITED REVIEWS

Nuclear Planetology: Especially Concerning the Moon and Mars

Kyeong Ja Kim[1] and Nobuyuki Hasebe[1,2]

[1] Korea Institute of Geoscience and Mineral Resources, Daejeon, 305-350 Korea; *kjkim@kigam.re.kr*
[2] Research Institute for Science and Engineering, Waseda University, Shinjuku, Tokyo 169-8555 Japan; *nhasebe@waseda.jp*

Received 2012 May 14; accepted 2012 July 5

Abstract To approach basic scientific questions on the origin and evolution of planetary bodies such as planets, their satellites and asteroids, one needs data on their chemical composition. The measurements of gamma-rays, X-rays and neutrons emitted from their surface materials provide information on abundances of major elements and naturally radioactive gamma-ray emitters. Neutron spectroscopy can provide sensitive maps of hydrogen- and carbon-containing compounds, even if buried, and can uniquely identify layers of carbon-dioxide frost. Nuclear spectroscopy, as a means of compositional analysis, has been applied via orbital and lander spacecraft to extraterrestrial planetary bodies: the Moon, Venus, Mars, Mercury and asteroids. The knowledge of their chemical abundances, especially concerning the Moon and Mars, has greatly increased in recent years. This paper describes the principle of nuclear spectroscopy, nuclear planetary instruments carried on planetary missions so far, and the nature of observational results and findings of the Moon and Mars, recently obtained by nuclear spectroscopy.

Key words: nuclear planetology: planetary remote sensing — elemental mapping — nuclear science payloads — chemical abundance

1 INTRODUCTION

The Moon, Mars and asteroids are neighboring celestial bodies to our planet, the Earth. Determining the distribution of major elements (Fe, Ti, Ca, Si, Mg, Al, O etc.), natural radioactive elements (K, Th and U) in the surface materials of celestial bodies with little or no atmosphere such as the Moon, Mars and asteroids, and volatile elements such as water ice in polar regions provides important clues about the conditions during the formation and evolution of these celestial bodies (Warren 1985; Warren & Wasson 1979; Wilhelms et al. 1987; Feldman et al. 1998; Wieczorek & Zuber 2004; Hiesinger & Head 2006; Mitrofanov et al. 2010). The global measurement of neutrons, gamma-rays and X-rays provides a powerful method for remotely measuring the absolute chemical abundances on their surfaces (Bielefeld et al. 1976; Adler & Trombka 1977, 1980; Feldman et al. 1999; Boynton et al. 2004; D'Uston et al. 2005; Hasebe et al. 2008, 2009).

Surface materials of those celestial bodies are always exposed to cosmic rays (CRs) if there is no or only a thin atmosphere. As a result of nuclear interactions of CRs with these celestial bodies, neutrons are produced almost constantly and are expelled from the interaction sites and escape into space or hit other nuclei. These neutrons can excite atomic nuclei through inelastic scatterings. Such excited atoms emit gamma-rays. A part of neutrons and gamma-rays produced in the materials leaks from their surface so that nuclear spectrometers can decipher which elements are present. Major elements excited by CRs, along with naturally radioactive elements, can be measured by nuclear instruments in orbit (Reedy et al. 1973; Reedy 1978; Yamashita et al. 2010).

Natural nuclear emission from those celestial bodies has been measured by remote nuclear sensing from orbit. Historically, Apollo and Luna pioneered these investigations of the Moon in the 1960s (Vinogradov et al. 1966; Metzger et al. 1973). The Lunar Prospector mission in the late 1990s and Mars Observer in the early 2000s performed global orbital imaging of lunar and Martian emission of gamma-rays and neutrons, which provided the first maps of a distribution of radioisotopes and soil constituting major elements over the entire lunar and Martian surfaces, respectively (Boynton et al. 2002; Feldman et al. 1998). Another important finding of these missions was the discovery of a high content of water ice in the shallow subsurface of the Moon and Mars (Feldman et al. 2001, 2002; Boynton et al. 2002; Mitrofanov et al. 2002). In the late 2000s, Japan (SELENE/Kaguya, Kato et al. 2008), China (Chang'E, Chin et al. 2007) and India (Chandrayaan, Goswami & Annadurai 2008) launched lunar missions after the Apollo, Luna and Lunar Prospector missions (Vinogradov et al. 1966; Metzger et al. 1973; Lawrence et al. 1998). X-ray and gamma-ray spectrometers (GRSs) were onboard those spacecraft. The scientific data from Mars Odyssey and SELENE (Kaguya) GRSs with a high purity Ge detector have demonstrated the necessity of high spectral resolution for reliably mapping key elements over the surface, but spatial accuracy of these maps has been limited by poor spatial resolution with the scale obtainable from an orbital altitude (Boynton et al. 2004; Hasebe et al. 2008, 2009; Kobayashi et al. 2010). Presently, another GRS employing Ge is onboard the spacecraft Messenger orbiting Mercury (Peplowski et al. 2011b; Goldsten et al. 2007; Nittler et al. 2011).

The scientific study of planets, moons, and planetary systems, in particular the study of the processes of their formation and evolution, is called planetology. Similarly, the geology of the Moon, and lunar science in general, is called selenology. Therefore, nuclear planetology and selenology apply the methodology of nuclear radiation detection to geosciences, geochemistry and planetology. In other words, we measure X-rays, gamma-rays and neutrons emitted from planetary/lunar bodies with a thin or no atmosphere. Here, we include not only gamma-ray and neutron spectroscopy but also X-ray spectroscopy in order to obtain information about chemicals in planetary/lunar bodies with nuclear planetology and selenology. Hereafter we simply call nuclear planetology/selenology "nuclear planetology."

This method can be divided into two classes: remote sensing and in-situ measurements. Remote nuclear planetology is the study of a planet by passively measuring isotopes, induced by Galactic CRs (GCRs) and those that occur naturally, from an orbiter or a fly-by mission (Boynton et al. 2004; Hasebe et al. 2008). Secondly, in-situ nuclear planetology is the science done with a landing/roving mission by passively measuring isotopes which are induced by GCRs or occur naturally and/or actively combining a neutron/X-ray source (Mitrofanov et al. 2009; Akkurt et al. 2005; Parsons et al. 2011; Hasebe et al. 2010; Gellert et al. 2004; Rieder et al. 1997; Toulmin et al. 1976).

Nuclear planetology provides unique opportunities to study planets and small bodies in the solar system, which are not possible with any other methods of investigation. Space experiments with nuclear instruments onboard orbiters and landers have the following features (Mitrofanov et al. 2009; Hasebe et al. 2010): 1) the determination of the concentration of major elements and natural radioisotopes in the material of different planets and celestial bodies in the solar system to understand their origin and evolution, 2) the study of the distribution of volatile materials such as H_2O, CO_2, SO_2 etc. in the subsurface of Mars, the Moon and Mercury in some particular regions on their surfaces,

and 3) the investigation of radiation conditions in interplanetary space and on the surface of planets, to determine potential radiation hazards during a long-duration space flight and long-duration stay on the Moon or Mars.

Developments in nuclear physics and computational simulation and analysis were introduced to nuclear geophysics. Today, these techniques that were developed in nuclear geophysics are also used in planetology and astrophysics. Nuclear planetology is the key to future In-Situ Resource Utilization (ISRU). ISRU enables this type of research and significantly reduces the mass and cost to produce materials and the risk of short-term and long-term exploration (Wieczorek et al. 2006; Spudis & Taylor 1992; Schrunk et al. 2008). In order to search for important surface elements on the subsurface of the Moon, Mars and asteroids, a neutron generator is an alternative source of GCRs and the active method combining X-ray, gamma-ray and neutron spectroscopy with an X-ray generator and a neutron generator can be applied for future landing missions on these celestial bodies (Mitrofanov et al. 2009; Akkurt et al. 2005; Parsons et al. 2011; Hasebe et al. 2010).

The main direction of further development of the method of nuclear remote sensing is thought to be the improvement of spatial resolution in measurements from orbit in order to identify features in images of nuclear emission with particular landscape features on the surface. Therefore, in the case of an orbital mission, it is necessary to have a spatial resolution for these measurements of about 10–30 km.

In remote nuclear planetology, CRs play an important role for the emission of gamma-rays and neutrons. Instead of CRs as incident projectiles, X-ray and neutron irradiation by the active use of radiation generation enables us to measure major elements, and the content of water ice/carbon dioxide in the polar soil over a short measurement interval (Mitrofanov et al. 2009; Akkurt et al. 2005; Parsons et al. 2011; Hasebe et al. 2010; Gellert et al. 2004; Rieder et al. 1997; Toulmin et al. 1976). Moreover, the instrumental design should be based on the increased spatial resolution for surface mapping of X-ray, gamma-ray and neutron emission with high spectral resolution and high sensitivity along the path of the rover within about one meter.

Before the Apollo and Luna missions, the state of understanding the Moon was a subject of almost unlimited speculation. Both studies of lunar samples and remote sensing data obtained by those programs gave us a broad outline of the nature, geologic and geochemical history of the Moon. Now we know that the Moon is made of rocky material that has been melted in various places, experienced volcanic eruptions, and pummeled by meteorite impacts. The Moon possesses a thick crust and a fairly uniform lithosphere, and a small iron core at the bottom of the asthenosphere. Some rocks give hints of an ancient magnetic field. The regolith was produced by innumerable meteorite impacts through geologic time. In addition, the Moon has recorded four billion years of the Sun's history to a degree of completeness that we are unlikely to find elsewhere.

However, many models formed after the Apollo mission are now being questioned on the basis of global data obtained by Clementine and Lunar Prospector, which were sent to the Moon. In the late 2000s, nuclear spectrometers on Lunar Prospector, SELENE (Kaguya), Chang'E and Lunar Reconnaissance Orbiter spacecraft and Mars Odyssey provided valuable data and enabled new findings. Those lunar and Mars data obtained in the late 1990s and 2000s are being integrated with new and old lunar sample data, to give us new ideas about the nature of the Moon.

The paper is organized as follows. In Section 2, we describe the principle of nuclear spectroscopy that we analyze to determine elemental composition in planetary bodies. Section 3 gives an overview of the nuclear spectrometers used in planetary gamma-rays, neutrons and X-rays. In Section 4 we present nuclear planetary explorations conducted so far. Some results of global abundance maps of the Moon and Mars observed by nuclear spectrometers are also presented. Section 5 includes a description of reduction and analysis of observation data obtained by nuclear spectrometers. Section 6 presents recent advancements in lunar and Martian sciences related to nuclear planetology. Discussion and the implications of the results related to lunar geochemistry are also included.

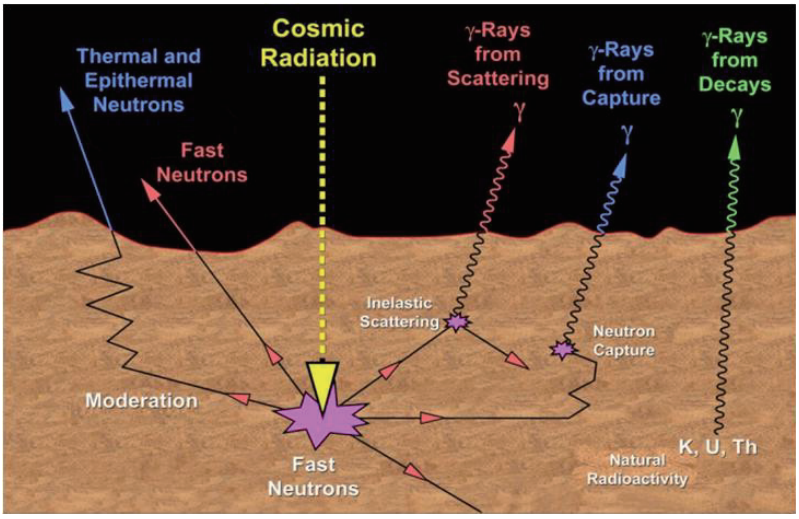

Fig. 1 Schematic drawing of gamma-ray emission from the surface of a planetary body with little or no atmosphere (Photo courtesy of J. Bruckner at MPIC).

The prospect of nuclear planetology and the role of future missions are summarized in the final section.

2 PRINCIPLE OF NUCLEAR SPECTROSCOPY

The spectral analyses of characteristic gamma-rays and neutrons induced by energetic neutrons and of fluorescent X-rays induced by solar X-rays are the most powerful methods for remote and in situ chemical analysis of heterogeneous materials on extraterrestrial bodies. Orbital and in situ measurements of the X-ray, gamma-ray and neutron emission spectra have been used to determine the chemical composition of the surfaces on lunar and planetary bodies.

The main sources of gamma-ray lines used for elemental measurement from orbit are nuclear reactions with all elements induced by fast and thermal neutrons and the decay of the natural long-lived radionuclides and their daughter products (see Fig. 1) (Evans et al. 1993; Feldman et al. 1993, Reedy 1978; Reedy et al. 1983). However, since their source intensities are too weak to make quick spectral analysis, cosmic ray induced gamma-ray and neutron spectra require long acquisition times and are not well suited for detailed evaluation of lunar or planetary materials near the surface using nuclear spectrometers on rovers. Solar induced X-ray fluorescence is also not suited for detailed evaluation, unless the Sun is fairly active in X-rays, as has been done at Mercury and several times at the Moon. Other potential sources of neutrons, X-rays in geochemical measurements, are actively used in radioactive isotope sources, pulsed fusion neutron generators and X-ray generators (Mitrofanov et al. 2009; Akkurt et al. 2005; Parsons et al. 2011; Hasebe et al. 2010).

2.1 Natural Sources of Gamma-Rays for Studying Planets

2.1.1 Natural radionuclides

Many naturally occurring nuclides are radioactive, that is, they spontaneously decay into nuclides of other elements that usually have a lower mass. In remote nuclear planetology, long-lived radioactive

Table 1 Major γ-rays from the Decay of Natural Radionuclides in Lunar Materials $*^{\dagger}$

Element	Nuclide	Energy (MeV)	Yield / Decay	Flux (photons cm^{-2} min^{-1})
K	^{40}K	1.4608	0.1067	2.39
Th	^{208}Tl	2.6146	0.360	2.19
	^{228}Ac	0.9689	0.175	0.66
	^{228}Ac	0.9111	0.29	1.05
	^{212}Bi	0.7271	0.070	0.23
	^{2028}Tl	0.5831	0.307	0.92
	^{228}Ac	0.3384	220	2.5–6.7
	^{212}Pb	0.2386	0.47	0.96
U	^{214}Bi	1.7645	0.159	0.64
	^{214}Bi	1.2381	0.059	0.20
	^{214}Bi	1.1203	0.15	0.48
	^{214}Bi	0.609	0.46	1.12
	^{214}Pb	0.3519	0.37	0.71
	^{214}Pb	0.2952	0.19	0.34

* Assuming the abundances are in ppm: K = 1200, Th = 1.9, U = 0.5; † from Reedy (1978).

nuclei include ^{40}K, ^{87}Rb, ^{138}La, ^{147}Sm, ^{176}Lu, ^{187}Re, ^{232}Th, ^{238}U, ^{235}U and their daughter products. These radioactive isotopes have survived since the beginning of our solar system and are still ubiquitous in planetary materials. However, their concentration in surface materials may vary greatly in different regions. Among them, ^{232}Th and ^{238}U and their daughters, as well as ^{40}K, are important for producing gamma-rays observed in the spectroscopy of extraterrestrial bodies.

The gamma-ray energies, yield/decay and gamma-ray fluxes (photons cm^{-2} min^{-1}) for these nuclides are shown in Table 1. The gamma-ray fluxes calculated from the Moon are assumed to have these elements in given abundances, which are uniformly distributed in terms of depth. Major gamma-ray lines are used to infer the concentration of those radionuclides. The gamma-rays are assumed to be emitted under secular equilibrium among the parent and daughter products. The equilibrium, however, can be disturbed by radon emanation, which leads to a change in the ratio of parent-to-daughter gamma-rays. To model the state of disequilibrium, gamma-ray lines from both the parent and daughter nuclides must be measured.

A. ***Potassium*** ^{40}K

The half-life of ^{40}K is $T_{1/2} = 1.25 \times 10^9$ yr. The 1.461 MeV gamma-ray line from an excited ^{40}Ar is emitted as 0.1048 yield per ^{40}K disintegration.

B. ***Thorium:*** ^{232}Th ***and its daughter products***

The half-life of ^{232}Th is $T_{1/2}$= 1.47 $\times$ 10^{10} yr. Major gamma-ray lines produced by the daughter of ^{232}Th are 2.615 MeV and 0.583 MeV from ^{208}Tl, and 0.911 MeV and 0.969 MeV from ^{228}Ac, and 0.239 MeV from ^{212}Pb. Strong lines of 0.583 MeV and 2615 MeV are, in general, used to derive Th abundance.

C. **Uranium:** ^{238}U ***and its daughter products***

The half-life of ^{238}U is $T_{1/2}$= 4.47 $\times$ 10^9 yr. Gamma-ray lines with energies above 0.200 MeV are emitted in the decay of ^{214}Pb and ^{214}Bi. The most intense lines are 1.765 MeV and 0.609 MeV from ^{214}Bi, and 0.352 MeV from ^{214}Pb. When the 609 keV peak in the gamma-ray energy spectrum observed by a Ge-detector in orbit is used to derive ^{238}U abundances, the peak line experiences interference from the ^{74}Ge sawtooth peak. The gamma-rays in the U-decay chain are made after the decay of 3.8 day for ^{222}Rn, a relatively long time. Radon diffusion could affect the assumption of

uniform distribution by moving the ^{222}Rn before it decays to ^{218}Po, when radon gas could leak from under the lunar ground to its outer surface. The radon (thoron) in the ^{230}Th chain is not expected to diffuse very far, because of its short lifetime of 56 s.

The typical γ-ray lines from K, Th and U are shown in Table 1, along with the fluxes calculated for the given abundances of the Moon, assuming that these elements are uniformly distributed in terms of depth over the Moon. Several γ-rays with a wide range of energies (e.g., 0.2386 and 2.6146 MeV in the Th decay chain) can be used to check the uniformity of the distribution of depth, since their energies show different penetration depths.

2.1.2 Gamma-Rays and neutrons produced by cosmic rays

A planetary body with a very thin or no atmosphere is directly exposed to GCRs. Secondary products, including neutrons and gamma-rays, are continuously produced by the nuclear interactions between the GCR nuclei and the materials in the lunar subsurface. In the field of lunar science, it is very important to know the production rates of these secondary products because the neutrons and gamma-rays emitted from the lunar surface can be used to estimate the elemental abundance of materials in the lunar subsurface (Evans et al. 1993; Reedy et al. 1973; Reedy 1978; Feldman et al. 1993). The composition of the Moon's surface has been investigated using neutron and gamma-ray spectrometers following the launch of Lunar Prospector (e.g., Gasnault et al. 2000). Above all, the recent successful mission of the Japanese lunar orbiter SELENE (Kaguya) equipped with a High Purity Germanium (HPGe) gamma-ray spectrometer reported improved global mapping data describing the composition of the lunar surface (Hasebe et al. 2008; Kobayashi et al. 2010). In order to be able to derive the absolute abundance of elements by nuclear spectroscopy, lunar scientists need a good simulation code for transporting the GCR nuclei and secondary products in the lunar material.

High energy particles capable of producing gamma-rays include GCRs (Simpson 1983; Masarik & Reedy 1994; McKinney et al. 2006; Shikaze et al. 2007) and solar energetic particles (SEPs) (Mewaldt 2006; Reames 1998) associated with large solar flares and/or large-scale coronal mass ejection. SEPs are not considered in this paper because SEPs can occasionally and transiently give rise to great enhancements of particle radiation in space, greatly vary in their fluxes and nuclear compositions from event to event and their energy spectra of the SEPs are generally very steep in comparison with that of GCRs.

The nuclear interaction of GCR particles with lunar materials produces numerous secondary particles. Most secondary charged particles easily lose their energies, so that they have low enough energies to stop and they cannot further induce nuclear reactions. However, as the secondary neutrons do not lose their energies through the process of ionization, they become the major component in the flux of particles capable of exciting gamma-ray emission. The majority of secondary neutrons produced through the nuclear interactions of GCRs have energies above 0.5 MeV. They are further slowed down in the planetary surface to produce thermal neutrons. Neutrons produced from nuclear reactions effectively generate gamma-rays, mainly from nonelastic scattering reactions with fast neutrons, and neutron capture reactions with thermal neutrons (Reedy et al. 1973; Reedy 1978; Evans et al. 1993).

A. ***Galactic Cosmic Rays***

In interplanetary space, CRs consist chiefly of energetic protons with energies above roughly 100 keV, which originate either at the Sun (Solar CRs: SCRs) or in interstellar space (GCRs). GCRs have a typical energy of $\sim$1 GeV and are continuously present, but fluctuate on a variety of time scales. SCRs are produced sporadically in solar flares, and generally have considerably lower energies than GCRs. Their energy spectrum is also a much more rapidly decreasing function of energy. After a solar flare produces SCRs, they are present in the solar system for only a relatively short time and decay away on a time scale of day (low energies) to hours (GeV particles). A planetary

body with little or no atmosphere is directly exposed to these high energy CR particles. Secondary products, such as neutrons and gamma-rays, are continuously produced by the interactions between the CR nuclei and the materials in the lunar subsurface. From the point of neutron and gamma-ray production induced by energetic CR particles, the GCRs on the planetary surface are very important, so here we only describe the GCR nuclei.

The GCRs are high energy nuclei with energies ranging up to $\sim 10^{20}$ eV consisting mainly of protons and He nuclei, and about 1% heavier ($Z > 2$) nuclei (Simpson 1983). GCR particles in the heliosphere are affected by the magnetic fields carried out from the Sun by the solar wind. These interplanetary magnetic fields interact with the GCR particles. The GCR-particle flux reaching the vicinity of the Earth, Moon and Mars correlates inversely with the level of solar activity. Variations in CRs can be directly observed in the inner solar system. The most important periodic variation is the variation of GCRs that is anticorrelated with the 11-year sunspot cycle. The 11-year variations are due to changing magnetic conditions in the heliosphere that influence the penetration of low energy GCRs into the heliosphere. Stronger magnetic fields and an enhanced degree of turbulence reduce their intensity in the heliosphere or prevent them from entering the inner heliosphere because of deflection. More subtle additional variations are observed that are probably linked to the polarity reversal of the heliospheric magnetic field, which occurs at successive sunspot maxima ($\sim$11 years apart) and has a periodicity of approximately 22 years, called the Hale cycle. The intensity of GCR particles varies by factors of 2–3 in energy from 100 MeV/n to 1 GeV/n during a typical 11-year solar cycle. The rates at which the GCR particles produce γ-rays are not constant with time. The flux of GCR particles around the Moon as integrated over all energies and angles and averaged over an 11-year solar cycle is about l.5 particles cm^{-2} s^{-1}.

The accuracy of the GCR spectral data is important from the point of neutron production in the lunar subsurface. Since Simpson's report on the GCR spectra (Simpson 1983), many researchers have used his spectra. However, some recent measurements of GCR spectra and their nuclear composition performed within the framework of the Alpha Magnetic Spectrometer (AMS), Cosmic AntiParticle Ring Imaging Cherenkov Experiment (CAPRICE), Balloon Experiment with a Superconducting Spectrometer (BESS) and Advanced Composition Explorer (ACE) experiments have revealed a number of important discrepancies from Simpson's data (Shikaze et al. 2007; Hayatsu et al. 2008). Recently, Masarik & Reedy (1994), Hayatsu et al. (2008) and Ota et al. (2011) calculated neutron fluxes in the subsurface of the Moon and showed the importance of the modulation factor, the scale factor of energy spectra of GCR nuclei and their chemical composition. Thus, the uncertainties in the GCR spectra may cause an ambiguity in neutron production. The study of a realistic spectrum of GCRs needs a precise estimation of the radiation environment on the Moon. A form of analytical functions describing energy spectra of proton and alpha particles in GCRs has been widely accepted as the means to vary some parameters (Castagnoli & Lal 1980; Masarik & Reedy 1994; McKinney et al. 2006). The 4π GCR flux J (particle/(MeV/n)/cm^2/s) is expressed by

$$J(E,\phi) = C\frac{E(E+2m_pc^2)(E+\chi+\phi)^{-\gamma}}{(E+\phi)(E+2m_pc^2+\phi)}\,,$$

where C is a normalization factor, E (MeV/n) is the kinetic energy of GCR nuclei, ϕ (in units of MV) is the solar modulation parameter to characterize the effect of solar activity, m_p (MeV c^{-2}) is the mass of the proton, c is the velocity of light, $\chi = a\exp(-bE)$, and the remaining parameters, such as a, b, and γ, have been described in detail for protons and alpha particles (Castagnoli & Lal 1980).

In the field of nuclear planetology, it is very important to know the production rates of these secondary products because the neutrons and gamma-rays emitted from the lunar surface can be used to estimate the elemental abundance of the lunar subsurface material (Evans et al. 1993; Reedy et al. 1973; Reedy 1978; Feldman et al. 1993; Kim et al. 2010, 2005).

Table 2 Information of Cross Sections of Inelastic Scattering in Gamma-Rays by Fast Neutrons (Kim et al. 2006)

Reaction	Gamma-ray energy (keV)	Threshold (MeV)	Peak cross section (mb)	Energy of peak (MeV)
^{12}C(n,ng)^{12}C	4438	4.8	450	8.1
^{16}O(n,ng)^{16}O	6128.6	6.6	265	7.5–9.0
^{16}O(n,p)^{16}N	6128.6	10.6	50	11.5
^{16}O(n,npg)^{15}N	5269.2	16.5	40	27.5
^{16}O(n,nαg)^{12}C	4438	12.3	130	19
^{24}Mg(n,ng)^{24}Mg	1368.6	1.4	600	2.5–6.0
^{27}Al(n,ng)^{27}Al	1014.4	1.1	220	2.5–6.7
^{27}Al(n,ng)^{27}Al	2211	2.25	210	7.0–9.5
^{28}Si(n,ng)^{28}Si	1779	1.8	770	4.5–6.0
^{32}S(n,ng)^{32}S	2230.1	2.3	440	6.7–10.0
^{40}Ar(n,ng)^{40}Ar	1460.8	1.5	800	3.0–10.0
^{40}Ar(n,p)^{40}Cl	1460.8	8	20	14.5
^{40}Ca(n,ng)^{40}Ca	3736.5	3.8	130	7
^{56}Fe(n,ng)^{56}Fe	846.8	0.9	1150	6
^{56}Fe(n,ng)^{56}Fe	1238.3	2.1	475	16.5

B. Nonelastic-Scattering Reactions Induced by Fast Neutrons

In a planetary GRS spectrum which is obtained by an HPGe detector system, about a few hundred gamma-ray peaks can be observed (i.e. Mars Odyssey and Kaguya). Among these gamma-rays, a few tens of full energy peaks of prompt gamma-rays induced by either thermal neutrons or fast neutrons have been attempted to be used for elemental mapping. Although most gamma-rays are produced by fast neutrons via inelastic scattering reactions, there are a few different reaction patterns of inelastic scattering reactions such as ^{28}Si(n,nγ)^{28}Si, with the gamma-ray emitted from an excited level of the target nucleus. In a few cases, such as ^{16}O(n, n$\alpha\gamma$)^{12}C, the excited level is in a nucleus that is different from the target nucleus, and the interaction is usually called an inelastic scattering reaction. There are also a few cases in which the gamma-ray is from the decay of a radionuclide, such as the 6129 keV gamma-ray produced by 67% of the decays of the radionuclide ^{16}N (with a half-life of 7.2 s) made by (n,p) reactions with ^{16}O. This reaction is included because it produces a 6129 keV gamma-ray in the Martian atmosphere that is not Doppler broadened due to motion of the excited nucleus as it decays (Evans et al. 2006) and this line could interfere with the measurement of oxygen content of the Martian surface (Kim et al. 2006).

It is important to know the cross sections of inelastic and nonelastic scattering in gamma-rays with respect to the neutron energy. The cross sections associated with inelastic gamma-rays are listed in Table 2. The threshold energy of 15 gamma-rays from nonelastic scattering reactions of a fast neutron has been varied from 0.9 MeV to 16.5 MeV. The excitation functions of these gamma-rays show that the cross sections increase rapidly above the threshold and reach a maximum a few MeV higher in energy. The cross sections then decrease with increasing energy to fairly low values above 20 MeV (Kim et al. 2006). For Mars Odyssey GRS (MOGRS) analysis, cross sections of inelastic gamma-rays were investigated through published references from the National Nuclear Data Center (NNDC) of Brookhaven National Laboratory. For many cases, the cross sections were based on prompt gamma-ray measurements done at Los Alamos Neutron Science Center (LANSCE) using a target many meters from a pulsed spallation-neutron source. The energy of the neutrons is determined by the time that it takes the neutron to travel from the source to the target (Nelson et al. 1991; Bernstein et al. 2001). The cross section data in the table are combined and values are extrapolated from several irradiated targets because in many cases only a few cross sections were

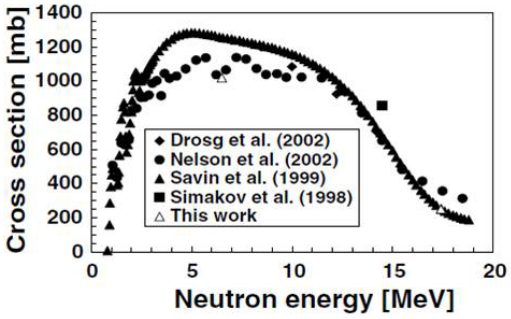

Fig. 2 Cross section as a function of neutron energy for the production of the ^{56}Fe(n,n'γ) 846.8 keV gamma-ray (Castaneda et al. 2007).

reported for the targets irradiated at LANSCE, and they are usually found to be in good agreement with published cross sections (Kim et al. 2006) (e.g. with quasi-monoenergetic neutrons from 6.5 to 64.5 MeV) (Castaneda et al. 2007) (Fig. 2). To estimate production rates of inelastic gamma-rays from a planetary surface, good cross section data as a function of energy are needed. The following equation is used for the estimation of inelastic gamma-rays or radionuclide production

$$P_j(r,d) = \sum_i N_i \sum_k \int_0^\infty \sigma_{jik}(E_k)\Phi_k(E_k,r,d)dE_k,$$

where P_j is the production rate (atoms/min/kg) for j at depth d, d is the depth (g cm^{-2}), r is the radius (cm), N_i is the number of target nuclei (atoms) of element i, and σ is the cross section (cm^2), E is the energy (MeV), and Φ is the secondary neutron or proton flux (particles cm^{-2} s^{-1}) involved in the reaction.

For elemental analysis of MOGRS, only the 1779 keV gamma-ray of ^{28}Si is used routinely and the 2230 keV gamma-ray of ^{32}S is used occasionally. The 4438 keV gamma-ray for ^{12}C is very broad, and the 847 keV gamma-ray of ^{56}Fe is among a series of peaks and features that make it hard to have its peak area determined (Evans et al. 2006). Of the fast neutron reactions with smaller cross sections, occasionally the 6129 keV gamma-ray of ^{16}O, the 1014 and 2211 keV gamma-rays of ^{27}Al, and the 3736.5 keV gamma-ray of ^{40}Ca are used for elemental analyses (Kim et al. 2006). The estimation method of production rates for inelastic scattering in gamma-rays for the MOGRS analysis has been used for MESSENGER GRS in 2011 by the GRS analysis group.

C. *Neutron Capture Reactions*

Neutrons with energies below the first excited level of the nuclei can be elastically scattered by various nuclei until they either escape from the planetary surface or are captured by nuclei. In gamma-ray emission, another important reaction can be described by

$${}^A_Z X + n \rightarrow {}^{A+1}_Z X^* \rightarrow {}^{A+1}_Z X + \gamma,$$

where X^* is the excited state of the nuclei. The gamma-ray emission is prompt and referred to as a prompt capture process. The energy involved in the prompt capture is comparable to the binding energy of the nucleus and thus is generally higher than the energy of the gamma-rays produced by the inelastic scattering. If $X(A{+}1,Z)$ is an unstable nucleus, the gamma-ray is emitted by the β-decay of the radioactive nuclide.

Table 3 Major γ-rays from Nonelastic-scattering Reactions or the Decay of GCR-induced Radionuclides (Reedy 1978)

Reaction	Gamma-ray energy (keV)	Threshold (MeV)	Peak cross section (mb)	Energy of peak (MeV)
^{12}C(n,ng)^{12}C	4438	4.8	450	8.1
^{16}O(n,ng)^{16}O	6128.6	6.6	265	7.5–9.0
^{16}O(n,p)^{16}N	6128.6	10.6	50	11.5
^{16}O(n,npg)^{15}N	5269.2	16.5	40	27.5
^{16}O(n,nαg)^{12}C	4438	12.3	130	19
^{24}Mg(n,ng)^{24}Mg	1368.6	1.4	600	2.5–6.0
^{27}Al(n,ng)^{27}Al	1014.4	1.1	220	2.5–6.7
^{27}Al(n,ng)^{27}Al	2211	2.25	210	7.0–9.5
^{28}Si(n,ng)^{28}Si	1779	1.8	770	4.5–6.0
^{32}S(n,ng)^{32}S	2230.1	2.3	440	6.7–10.0
^{40}Ar(n,ng)^{40}Ar	1460.8	1.5	800	3.0–10.0
^{40}Ar(n,p)^{40}Cl	1460.8	8	20	14.5
^{40}Ca(n,ng)^{40}Ca	3736.5	3.8	130	7
^{56}Fe(n,ng)^{56}Fe	846.8	0.9	1150	6
^{56}Fe (n,ng)^{56}Fe	1238.3	2.1	475	16.5

Major gamma-rays from neutron capture reactions or the decay of captured radionuclides are listed in Table 3. The fluxes of thermal neutrons are influenced by the presence of (a) light elements which rapidly moderate neutrons to thermal energies through elastic scattering and (b) the elements with large absorption cross sections in the material. Therefore hydrogen and carbon affect thermal electrons.

A high concentration of elements with large cross sections effectively absorbs thermal (below $\sim$0.4 eV) and epithermal neutrons (eV–keV) and then decreases their flux. Relatively abundant elements with significantly high neutron absorption cross sections are Fe (2.6 b), Ti (6.1 b), Mn (13.3 b) and Cl (33.2 b). Elements with low neutron absorption cross sections are O (2.7×10^{-4} b), C (3.4×10^{-3} b), N (7.5×10^{-2} b) and Mg (6.3×10^{-2} b). Most minor and trace elements except for Gd (4.89×10^{4} b) and Sm (5.67×10^{3} b) do not strongly affect the properties of thermal-neutron absorption in the planetary surface. Elements with intermediate cross sections are H (0.33 b), S (0.52 b), Na (0.40 b), Al (0.23 b), and Si (0.16 b).

It is noted that the absolute fluxes of gamma-ray lines generated by capture reaction depend on the fluxes of the incident GCRs and are affected by the abundances of light elements. However, the absolute abundance of elements can be derived with the help of measurement data of thermal and epithermal neutron fluxes, because the relative fluxes for neutron-capture gamma-rays can be well calculated.

D. Expected planetary gamma-ray flux

As described above, gamma-rays are produced by the decay of long-lived radioactive elements and by cosmic ray interactions with material on the planetary surface (Fig. 1). Characteristic gamma-rays for each major element in the surface are mainly produced by inelastic collisions with fast neutrons and by thermal neutron capture. In order to illustrate the information provided by gamma-rays, the flux of gamma-rays that do not come from collocations, but rather are leaking away from the lunar surface with discrete energies, are calculated by Reedy (1978) and shown in Figure 3 for an assumed lunar composition. The intensity of the gamma-rays produced by nuclear reactions varies in proportion to the concentration of the elements and the flux of particles that cause the nuclear reactions. Major γ-rays from the decay of natural radionuclides, from nonelastic scattering reactions

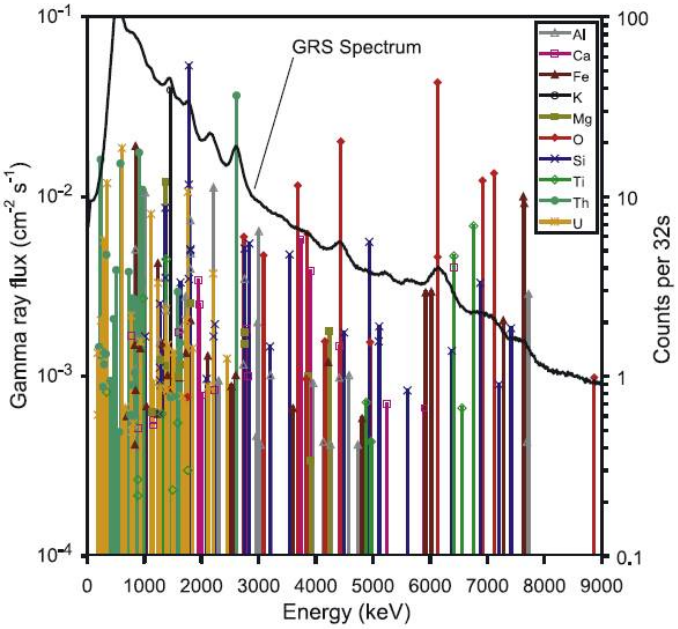

Fig. 3 Fluxes of γ-rays as a function of energy that leak from the lunar surface without changing energy as calculated by Reedy (1978). The source for each major γ-ray is indicated by the symbol at the top of the line. An element or radionuclide producing that γ-ray is indicated above the more intense γ-rays. (Figure from Prettyman et al. 2006a with a measured lunar spectrum.)

or the decay of GCR-produced radionuclides and from neutron capture–reactions or the decay of capture-produced nuclides (calculated by Reedy 1978) are listed in Tables 1, 3, and 4 respectively.

2.1.3 X-rays induced by solar X-rays

Major rock-forming elements (Mg, Al, Si) are very important for identifying types of rocks in a planetary surface. Ti abundance is also important and useful for classification of lunar mare basalts, since it varies from very low-Ti (< 1 wt%) to high-Ti (> 5 wt%), and its regional distribution provides the key to solving the history of mare production and the composition of its interior reservoir. Mg/Fe also gives one of the most important pieces of information about lunar crust and mantle. X-ray fluorescence (XRF) spectrometry aims at mapping the composition of most major elements, especially Mg, Al, Si, Ti and Fe.

The passive X-ray measurement is based on the bombardment of the sample surface with naturally occurring X-rays on the planetary surface. An X-ray detector measures the energy distribution of the X-rays emitted by atoms in the sample. These X-rays result from high energy solar X-rays or charged particles (SCR and GCR), and those processes are referred to as XRF and particle-induced X-ray emission (PIXE), respectively.

XRF is a well-established technique for major elemental analysis in the laboratory. Solar irradiation excites fluorescent emission from the lunar surface. By measuring this emission, while at the same time monitoring the incident solar X-ray emission, we are able to map the absolute elemental abundances of the main rock-forming elements on the Moon. In space, as was shown in the Apollo 15, 16 and Chandrayaan-1 missions (Adler & Trombka 1977; Trombka et al. 2000; Grande et al.

Table 4 Major γ-rays from Neutron-capture Reactions or the Decay of Capture-produced Radionuclides* (from Reedy 1978)

Element	Source^{+}	Energy (MeV)	Yield / Capture	Gamma-ray flux (photons $cm^{-2}min^{-1}$)
H	$^{1}H(n,\gamma)$	2.2233	1.00	0.09
Al	$^{27}Al(n,\gamma)$	7.724	0.30	0.17
	^{28}Al	1.7788	1.00	0.21
Si	$^{28}Si(n,\gamma)$	4.934	0.61	0.34
	$^{28}Si(n,\gamma)$	3.5395	0.66	0.29
Cl	$^{35}Cl(n,\gamma)$	6.111	0.21	0.22
Ca	$^{40}Ca(n,\gamma)$	6.420	0.40	0.24
	$^{40}Ca(n,\gamma)$	1.9427	0.80	0.21
Ti	$^{48}Ti(n,\gamma)$	6.7615	0.40	0.41
	$^{48}Ti(n,\gamma)$	6.419	0.28	0.28
	$^{48}Ti(n,\gamma)$	1.3815	0.82	0.27
Cr	$^{53}Cr(n,\gamma)$	8.884	0.24	0.028
Fe	$^{56}Fe(n,\gamma)$	9.299	0.03	0.09
	$^{56}Fe(n,\gamma)$	7.6457	0.22	0.55
	$^{56}Fe(n,\gamma)$	7.6313	0.24	0.60
	$^{56}Fe(n,\gamma)$	6.019	0.08	0.18
	$^{56}Fe(n,\gamma)$	5.921	0.08	0.18
Ni	$^{58}Ni(n,\gamma)$	8.999	0.37	0.07

*Assuming the following abundances in terms of weight by percent: H=0.1, Al=11, Si=20, Cl=0.2, Ca=10, Ti = 1.4, Cr = 0.3, Fe = 0.9, and Ni = 0.4.
$^{+}$Reaction or radionuclide.

2003), XRF can be used to determine the major-element composition of the several uppermost tens of micrometers of atmosphere-free planetary bodies such as the Moon, Mercury, and asteroids (Adler & Trombka 1977; Trombka et al. 2000; Grande et al. 2003; Okada et al. 1999, 2000; Solomon et al. 2001; Grard & Balogh 2001). However, since intensities and spectral profiles of solar X-rays vary with time, which affects emission profiles of XRF from the planetary surfaces as well, the analysis is complicated by features in the solar spectrum and flux variations. Therefore, mapping of major elemental composition from orbit requires concurrent monitoring of solar X-rays. In addition, localized concentration levels of key minor elements can be detected during a period of solar activity due to a solar flare.

High energy particles can also induce XRF. As is used in the laboratory analysis, a process that uses natural PIXE or electron induced X-rays is expected to take place on the planetary surface (Kamata et al. 1999; Grande 1997). Characteristic X-rays will be identified when the solar activity is high enough to excite XRF.

Surface roughness affects the intensities and spectral profiles of XRF. Most of these planetary surfaces are often covered with regolith whose particle size ranges from a micrometer to a millimeter in diameter with a mean of 70 to 100 μm. The intensities of XRF decrease with larger particle size (rougher surface geometry) and larger phase angles (Okada 2004; Maruyama et al. 2008). This phenomenon is generally present for low energy and small-Z elements.

2.2 Active Source of Neutrons and X-rays

In remote nuclear planetology, GCR particles play an important role in the emission of gamma-rays and neutrons. Since the counting rate, however, is very low because of weak intensity of GCR particles, it takes a long time to achieve a full energy spectrum of gamma-rays with statistically high precision at a specific site. Instead of GCR particles as incident projectiles, the active method of neutron irradiation by use of a pulsed neutron generator enables us to measure major elements

(Mitrofanov et al. 2009, Akkurt et al. 2005; Parsons et al. 2011; Hasebe et al. 2010; Gellert et al. 2006). The active method greatly improves its spatial resolution for surface mapping of gamma-ray and neutron emission with high spectral resolution and high sensitivity along the path of the rover, within about one meter. In the future, a gamma-ray, neutron and X-ray spectrometer system (GNX), combined with active neutron and X-ray irradiation, shall be developed for lunar roving missions.

Advances in nuclear physics and nuclear engineering were immediately applied to nuclear geosciences and planetology. Nuclear spectroscopy applies the method of nuclear radiation detection to geosciences as well as planetology. In general, neutrons are produced by techniques using radioactive sources or pulsed neutron generators (Mitrofanov et al. 2009, Akkurt et al. 2005; Parsons et al. 2011).

2.2.1 An active source of neutrons

In the active method of gamma-ray spectroscopy, potential sources of neutrons for geochemical measurements on extraterrestrial bodies are radioactive sources such as (αn) reactions (e.g.^{241}AmBe) and spontaneous fission isotopes (e.g. ^{252}Cf) (Knoll 2000). Isotopic sources have the advantage of having a long-life and producing a relatively constant flux of neutrons. However, the isotopic sources have several disadvantages. The neutron flux cannot be switched off. Therefore, they must always be contained within a massive shield, though the sources are very light in weight. The energy spectrum of emitted neutrons is broad and its average energy is relatively small.

On the other hand, neutron generators have been evolving into a compact and affordable product. Compact neutron devices that use deuterium–deuterium (D–D) and deuterium–tritium (D–T) reactions have the most widespread use (Knoll 2000). Small neutron generators using the ^{2}D–^{3}T reaction are the most common accelerator. Creating deuterium ions and accelerating these ions into a tritium or deuterium target produces neutrons. Deuterium atoms in the beam fuse with deuterium and tritium atoms in the target to produce neutrons.

$$\mathrm{D + T \rightarrow n + {}^{4}He}, \qquad \mathrm{En = 14.2\ MeV.}$$

$$\mathrm{D + D \rightarrow n + {}^{3}He}, \qquad \mathrm{En = 2.5\ MeV.}$$

Accelerating ^{2}D ions into a ^{3}T target produces neutrons. The ^{2}D+^{3}T reaction has the largest maximum cross section of 5.0 barn at the energy of 130 keV. Neutron emission from the ^{2}D–^{3}T reaction is isotropic with respect to the target. Neutron emission from the D–D reaction has a wider peak in the energy spectrum, and a helium-particle is emitted in the exact opposite direction of the neutron. Advances in neutron generation are focused toward the development of compact and light systems with longer lifetimes and higher outputs (Mitrofanov et al. 2009; Akkurt et al. 2005; Parsons et al. 2011; Hasebe et al. 2010). Reductions in size and weight are mostly driven by the growing demand for planetary applications.

In the case of a generator based on the D-T reaction, it produces pulses of 14 MeV-neutrons available with a number of about 10^{7}–10^{8} particles per second, which depends on electric power consumption, and GRS measures the intensity and time profile of dynamic gamma-rays and neutrons. The short period of operation (about 10 minutes) of the system provides the abundance of major elements in the lunar/martian soil. A line source at 14 MeV can inelastically excite all nuclei and therefore provides a wide range of elements for study of the planets.

A pulsed neutron generator emits neutrons within a short pulse of 100 ns to 10 μs (Akkurt et al. 2005; Parsons et al. 2011). The neutron source permits the gamma-ray discrimination between gamma-rays produced promptly by the inelastic scattering reaction of fast neutrons (γ-ray I in Fig. 4), gamma-rays produced by thermal neutron capture (γ-ray II in Fig. 4), and gamma-rays resulting from delayed activation and natural radioactivity (γ-ray III in Fig. 4). This separation of

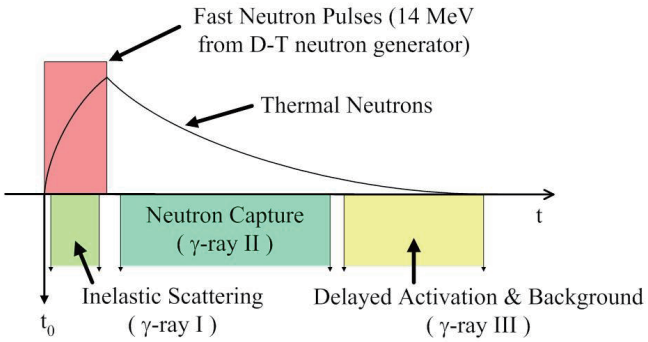

Fig. 4 The timing diagram showing how a population of neutrons changes with time between high-energy neutron pulses and how coincidence gates operate for gamma-ray data acquisition.

gamma-ray data acquisition through prompt coincidence and delayed coincidence methods into optimum specific time windows can be obtained (see Fig. 4).

Gamma-ray spectroscopy with active neutron irradiation for nuclear planetology can be applied for measuring soil composition along a trace and for selecting the most interesting samples of planetary surface material. A future instrument combining GRS and neutron generation can shorten the measurement interval with the use of high counting rate processing for the active method and increase the sensitivity of gamma-ray detection and the scope of chemical elements. The active method will also be applied for a future landing mission on an asteroid, Mars, or even Venus with a very thick atmosphere for measuring the bulk composition of Venus' soil within a volume of about 1 meter from the lander (Mitrofanov et al. 2009).

2.2.2 Active source of X-rays

An X-ray generator is a device (material) used to generate X-rays. Various radiation sources such as X-rays, electrons, α-rays etc. are emitted to strike a target material, creating excited or ionized atoms in the target. Many excited atoms or ions in the target subsequently de-excite to the ground state through the emission of characteristic X-rays. Then, the target can serve as a localized source of X-rays. The X-ray energy depends on the choice of target material. The targets with high-Z produce higher energy X-rays. The incident radiation must have a higher energy than the maximum photon energy expected from the target. Conventionally, an X-ray tube has been used as the X-ray source. These X-rays in the target sample, through photoelectric absorption and the subsequent de-excitation, create their characteristic X-ray spectrum, called fluorescence.

As an alternative to the X-ray tube, a radioisotope, for example ^{241}Am which emits 60 keV gamma-photons, can be used as the source of excitation. α-ray emitting radioactive sources, such as ^{244}Cm and ^{210}Po, are generally used as an XRF source, because they are light-weight, compact sources with stable intensity, and are relatively free from contaminant electromagnetic radiation (forming a continuum background spectrum of X-rays). A ^{244}Cm α-ray emitter was (will be) used in the experiments of Mars missions (Rieder et al. 1997; Gellert et al. 2004; Gellert et al. 2009). Under the severe restriction of resources in space experiments, those radioisotopes have the advantage of convenient half-lives, producing a relatively constant flux of X-rays, though the isotopic sources have disadvantages that the X-ray flux cannot be switched off and there is a risk of spreading radioisotopes at the time of spacecraft launch. In the next subsection, we address conventional X-ray tubes and pyroelectric X-ray generators that were developed in relatively recent years.

A. ***X-ray Tube***

An X-ray tube system including the X-ray tube, high voltage power supply, controller and cooling system can replace radioisotopes in XRF analysis applications. X-rays are generated by fast electrons at a target material such as tungsten. When the electrons are slowed or stopped by the interaction with atoms in the target, X-radiation is produced. The tube cathode (filament) is heated with a low-voltage current. The filament heats up and electrons in the wire become loosely held. A large electrical potential is created between the cathode and the anode by the high-voltage generator. The tube current is controlled by regulating the low-voltage heating current applied to the cathode. The higher the filament temperature, the larger the number of electrons that are emitted.

The high-voltage, generally 10 to 150 kV, between the cathode and the anode affects the electron energy at which the electrons travel and strike the anode. Accelerations produced by higher voltage generate X-rays with higher energy. An increase in the voltage will also result in an increase in the intensity of the radiation. The anode target is commonly made from tungsten, which has a high melting point in addition to a high atomic number. However, cooling of the anode by active or passive means is necessary. Low power tubes are cooled simply with the use of thermally conductive materials and heat radiating fins.

B. ***Pyroelectric X-ray Generator***

Pyroelectric crystals, when heated or cooled, exhibit a change in the polarization proportional to the crystal's pyroelectric coefficient times the magnitude of the temperature change (Rosenblum et al. 1974). Heating a pyroelectric crystal can be the ejection of electrons from the crystal surface and if we accelerate those electrons to high energies and they strike a metallic target, the electrons are sufficiently energetic to create bremsstrahlung and fluorescent X-rays (Rosenblum et al. 1974; Brownridge & Raboy 1999).

An X-ray generator with a pyroelectric crystal (Geuther & Danon 2005) is commercially available. The principle of the pyroelectric X-ray generator is quite different from that of conventional X-ray tubes, and this new device does not require a high-voltage power supply. It can be driven by heating and cooling the crystal with a low voltage. It has characteristics such as low power and periodically changing X-ray intensity. Although these characteristics seem to be disadvantageous to measurement, it can be used for XRF analysis. Quantitative analysis at the percent level can easily be performed with this X-ray source. This X-ray source is suitable for in-situ analysis of lunar and planetary materials, because compact and low-power operation of an X-ray source is a great advantage for portable devices.

Pyroelectric X-ray generator technology has enabled researchers to develop spaceborne, low-power X-ray sources for use in material analysis. In XRF, for example, high-energy sources enable the excitation of the K-shell X-ray peaks for high-Z materials as well as the lower-energy L-shell peaks.

When heated, a pyroelectric crystal exhibits a spontaneous decrease of polarization. Hence, as the temperature increases, an electric field develops across the crystal. The top surface of the crystal gets positively charged and attracts electrons from the low pressure gas in the environment. As the electrons impinge on the surface of the crystal, they produce characteristic X-rays. When the cooling phase starts, the spontaneous polarization increases, and the electrons from the top surface of the crystal are accelerated to energies to create bremsstrahlung and fluorescent X-rays. When the crystal temperature reaches its minimum, the heating phase starts again. The cycle time can be varied from 2 to 5 minutes.

The pyroelectric X-ray generator is very attractive for spaceborne XRF systems, since the source can be turned off after use, requires little shielding, and can be operated with very low power.

C. Advances in X-ray Spectrometry in Space

Carbon nanotubes emitting electrons as a cathode at room temperature, when exposed to an electric field, have been fashioned into an X-ray device. Field-electron emission is used for the extraction of electrons from a noninsulating solid surface through electron tunneling whose process is exponentially affected by the chemical state of the emitter surface. It implies that field-electron emitters must be robust for their wide applications in a non-ultrahigh vacuum where the interaction between the emitter and residual gases is unavoidable. The "carbon nanofibers" as an electron-beam tool satisfy this requirement well (Bonard et al. 2001).

The carbon nanotube emitters also use less energy than conventional X-ray tubes leading to lower operational costs. The potential benefits of a field-electron X-ray source are exciting, since it could serve to miniaturize the entire tube structure (Haga et al. 2004; Sugie et al. 2001). A so-called "miniature X-ray tube" of this kind could provide a finely focused electron beam and hence X-ray images with an ultrahigh resolution, paving the way to new frontiers in X-ray spectroscopy in planetary science.

3 NUCLEAR SPECTROMETER

Throughout this article, the word "radiation" will be used to mean "ionizing radiation" and can refer to either charged particle radiation such as electrons and heavy charged particles, or to uncharged radiation such as X-ray and gamma-ray photons and neutrons, provided that they have enough energy to induce ionization. Here we focus on X-ray, gamma-ray and neutron radiation.

3.1 Gamma-Ray Detector

The three basic interactions of gamma-rays with matter are: the photoelectric effect, Compton scattering, and pair production. The photon is completely absorbed in cases of photoelectric effect and pair production, but only partial energy is deposited in any given Compton scattering. In general, the photoelectric effect dominates in the energy region up to $\sim$200 keV, the Compton effect up to a few MeV and pair production above 5–6 MeV. For a given compound, let N be the number of atoms per unit volume and Z its effective atomic number. The interaction cross sections vary as NZ^5 for the photoelectric, NZ for Compton scattering and NZ^2 for pair production (Knoll 2000).

In selecting a gamma-ray detector, gamma-ray spectroscopy requires accounting for a number of factors including detection efficiency of gamma-rays and energy resolution. In addition, material properties are important to consider whether the detector crystal is hygroscopic, and is rugged with respect to thermal and mechanical shock, and whether a large volume crystal is available.

All semiconductor detectors including compound semiconductor detectors operate as solid state ionization chambers. The choice to use for a specific application depends to a large extent on the energy range of interest. Only the photoelectric effect leads to the total absorption of the incident energy, since a Compton scattered photon or an electron–positron pair (or its interaction products) may escape the detection volume and subsequently not deposit all of their energy within the detector. Thus, it can be seen that for good spectroscopy at gamma-ray energies, one should choose the highest possible Z, since this increases the energy range over which total energy absorption can occur due to the photoelectric effect. However, for compounds, absorption is most influenced by the element with the highest atomic number, rather than the compound's average Z.

3.1.1 Semiconductor detectors

Semiconductor devices have been used as radiation detectors in nuclear, high energy physics, space science and many other fields during recent decades. In these detectors, radiation is measured by means of the number of charge carriers set free in the detector. Ionizing radiation produces free

electrons and holes. The number of electron-hole pairs is proportional to the energy deposited in the detector medium of a semiconductor. As a result, a number of electrons transferred from the valence band to the conduction band, and an equal number of holes created in the valence band are collected at detector electrodes. Under the influence of an electric field, electrons and holes drift to the electrodes. The holes travel in the opposite direction and can also be measured.

A distinguishing feature of semiconductor detectors is the relatively small amount of energy required on average to produce an electron-ion pair (called ε-value); typically, the ε-value for Si is about 3.62 eV ($T = 300$ K), and the ε-value for Ge, 2.96 eV ($T = 77$ K), roughly a factor of ten smaller than that of a typical gas. The intrinsic resolution of these devices is therefore much better than that of gas detectors. Consequently, in semiconductor detectors the statistical variation of the pulse height is small and the energy resolution is high. Moreover, the electrons move so fast that the time resolution is good and the counting rate is high. Compared with gaseous ionization detectors, the semiconductor detector becomes compact in size and light in weight, because of the high density of its semiconductor medium. These features are an advantage under the restriction of resources in space experiments. Here we address the topic of a Ge detector and other semiconductor detectors as semiconductor gamma-ray detectors.

A. ***High-Purity Germanium Detector***

Germanium detectors are widely used for gamma-ray spectroscopy in nuclear physics. Germanium can have a thickness of centimeters with sensitivity, and therefore can be used as a total absorption detector for gamma-rays up to a few MeV, but silicon detectors cannot be thicker than a few millimeters. Techniques for the production of high-purity germanium with impurity levels as low as 10^9 atoms cm^{-3} have been achieved. Large single crystals of germanium are commercially fabricated from high-purity material in which the net dopant concentration is very small. The type of Ge detector manufactured from this ultrapure crystal is called a High-Purity Germanium (HPGe) detector. Impurities in the crystals trap electrons and holes, deteriorating the performance of the detectors.

HPGe detectors commonly use lithium diffusion to make an n^+ ohmic contact, and an implementation of boron to make a p^+ contact. Coaxial detectors with a central n^+ contact are referred to as n-type detectors, while p-type detectors have a p^+ central contact. The implanted p+ contact on the outside is <0.5 μm thick. The n+ and p+ contacts are formed by diffusion of lithium and implantation of boron, respectively. The thickness of these contacts represents a dead layer around the surface of the crystal. The thickness of a typical dead layer is several hundred μm for an Li diffusion layer, and a few tenths of a micrometer for a B implantation layer. Because a large active volume, with a great thickness, is required for the detectors intended for gamma-ray spectroscopy, a large close-ended coaxial crystal is generally used in which only part of the central core in the coaxial cylinder is removed and the outer electrode extends over the outer cylindrical surface.

Radiation damage is induced to the Ge detector by the collision of high-energy particles in space with germanium atoms. The dominant source of radiation damage in the Ge detector mainly arises from protons in the GCRs. A high purity n-type Ge crystal detector is able to withstand more proton/neutron fluence than a p-type crystal. Ge detector, however, must be cooled down to a cryogenic temperature during the operation to reduce the leakage current that can deteriorate the energy resolution. Moreover, cooling the Ge crystal below 90 K, which is a major drawback of Ge detectors for producing spectroscopic data, is also necessary in terms of radiation damage (Quarati et al. 2009; Pirard et al. 2007). If a detector in space is kept colder than about 90 K, this damage is not observed for several years. If the detector is once warmed above this temperature and then cooled to operational temperatures, the damage is prominently observed in the spectra. However, radiation damage can be annealed by heating the detector to high temperatures. Therefore, HPGe detectors have been used in planetary explorations (Hasebe et al. 2008; Boynton et al. 2004; Goldsten et al. 2007).

B. ***Compound Semiconductor Detector***

A semiconductor detector has the potential benefits for the detection of X- and γ-ray radiation. Si and Ge have become standards for detection associated with spectroscopy of energy measurement, and their use for various applications has increased. However, some physical limitations such as the need for ancillary cooling systems, their modest stopping powers and radiation intolerance has led researchers to develop compound semiconductors with a wide band gap. The wide band gap compounds under a wide range of thermal and radiation environments offer the ability to operate and measure over a wide dynamic range of radiations (Knoll 2000; McGregor & Hermon 1997; Del Sordo et al. 2009). Among the compound semiconductors, CdTe and CdZnTe have attracted growing interests in the development of X-ray and gamma-ray detectors of space experiments from sub-keV energy resolution in the soft X-ray band and tens of keV in the gamma-ray. The advantages include good crystal growth technology with adequate homogeneity and purity, as well as high detection efficiency with a high mean atomic number, functionality at room temperature due to wide band gap compound material and good energy resolution. In particular, good room temperature performance is very attractive for X-ray and gamma-ray applications. For these compound semiconductor detectors, modest cooling can reduce the leakage current and thereby improve the energy resolution of these detectors. Additionally, temperature reduction can reduce the noise level of the FET in the preamplifier. In case of CdTe, the leakage current is high enough so that further cooling to –40°C can produce useful improvements in their energy resolution. Compactness is preserved through the use of miniature electrical Peltier coolers that are built into the detector housing and whose presence is virtually invisible to the user. The capability of CdTe/CdZnTe detectors in planetary and astrophysical applications has already been demonstrated with astronomical satellites (Prettyman et al. 2003; Ubertini et al. 2003; Ferrando et al. 2005; Gehrels et al. 2004).

3.1.2 Scintillation Detectors

Scintillation material, or scintillator, is widely applicable in high energy physics, nuclear physics, space physics, nuclear medicine, geological prospecting and other industries. Scintillator is material which emits scintillation light - the property of luminescence when it is excited by ionizing radiation such as a gamma-ray, an X-ray or fast charged particle radiation (Knoll 2000). It reemits the absorbed energy within $\sim 10^{-9}$–10^{-6}s in the form of a small flash of light, typically in the ultraviolet to visible range. The scintillation light is collected by a photodiode or a photomultiplier. The light sensitive detectors produce, for each light pulse, a current pulse which is analyzed in electronic processing equipment. Light pulses emitted by a scintillator are proportional to the energy of the incident beam. This is why scintillation detectors are used for radiation detection and spectroscopy. There are various scintillation materials. The most common scintillators used in gamma-ray detectors are made of inorganic materials. In materials, an impurity called an "activator" is often added.

Some of the properties desirable in a good detector, which is constructed to be a scintillator, are: a high scintillation light yield, a high transparency to its own scintillation light, a high detection efficiency, a high stopping power, a good linearity over a wide range of energy, a short decay time of scintillation, and a good emission spectral range matching the spectral sensitivity of an existing photomultiplier tube (PMT) or photodiode. Ruggedness and good behavior under high temperature may be desirable where resistance to vibration and high temperature is required for such a lunar exploration mission as a rover. The overall signal production efficiency of the detector, however, also depends on the quantum efficiency of the PMT (typically $\sim$30% at peak), and on the efficiency of light transmission and collection which depends on the type of reflector material covering the scintillator and light guides, the length/shape of the light guides, any light absorption, etc. The typical light output when the incident particle is an electron is given as: $\sim$40 photons keV^{-1} for NaI(Tl), $\sim$10 photons keV^{-1} for plastic scintillators, and $\sim$4 photons keV^{-1} for bismuth germinate (BGO, $Bi_4Ge_3O_{12}$). These inorganic scintillators have been used in the field of nuclear planetology.

A. ***Sodium Iodide, Cesium Iodide and Bismuth Germanate Detectors***

Sodium Iodide (NaI) is an alkali halide inorganic scintillator with a relatively high $Z(53)$ from iodine. This results in high efficiency for gamma-ray detection. A small amount of Tl is added in order to activate the crystal, so that it is typically expressed as NaI(TI). Energy resolution of about 6%–7% for the 662 keV gamma-ray from ^{137}Cs is achievable for a 3″-diameter by a 3″-long crystal. The light decay time constant in NaI(Tl) is about 0.23 μs.

CsI also requires a small amount of thallium or a sodium activator for proper operation. CsI has a higher intrinsic efficiency than NaI, but lower than BGO. CsI has a poorer energy resolution than NaI. However, CsI has a much faster pulse light decay and finds use in timing applications but the wavelength of its light is poorly matched to most PMTs. It is also less brittle than NaI and less hygroscopic than NaI, but more than BGO.

BGO is a scintillation crystal that features high density due to the high Z(83) of bismuth. Its high intrinsic efficiency at high gamma-ray energies makes an excellent alternative to NaI. BGO has a fast response and little or no afterglow. Because of its speed of response and high density it is ideal for high energy and high rate gamma-ray measurements. The disadvantage of BGO is its low conversion efficiency (i.e. low light output) which results in poorer energy resolution than an NaI detector. A green fluorescent light has a peak wavelength of 480 nm. With its elevated stopping power, high efficiency scintillation, high count rate and non-hygroscopic properties, BGO is an excellent scintillation material.

These scintillators of NaI(Tl), BGO and CsI(Tl) were used in US Apollo and Lunar Prospector GRSs (Harrington et al. 1974; Feldman et al. 1999), USSR Luna GRS (Surkov 1981) and Chinese Chang'E GRS (Chang et al. 2009).

B. ***Lanthanum Bromide Detectors***

Lanthanum Bromide, or $LaBr_3$(Ce), is one of the new generation of inorganic scintillation gamma-ray detectors (van Loef et al. 2001; van Eijk et al. 2004; Weber 2002). $LaBr_3$ detectors exhibit high light output, high resolution and fast light decay time. These detectors also offer excellent temperature and linearity characteristics. The typical energy resolution at 662 keV is 3% as compared to NaI(Tl) detectors at 7%. The improved resolution is due to a photoelectron yield by a factor of 1.6 higher than that of NaI(Tl). Another advantage of $LaBr_3$ is the nearly flat photoemission over a 70 ° C temperature range ($\sim$1% change in light output). $LaBr_3$ detectors are offered with a super bialkali PMT. Silicon drift detectors (SDD) can be used, which enable designing a compact implementation of the device. The UV enhanced Si diodes provide excellent wavelength matching to the 380 nm emission of $LaBr_3$. Moreover, the SDD is not as sensitive to temperature and bias drift.

$LaBr_3$ can be applied to a spectroscopic detection of gamma-rays and an identification system used in nuclear planetology. The improvements in resolution allow more accurate peak discrimination in ranges where various elements have many overlapping peaks, which leads to better determination of elemental concentration. $LaBr_3$ was flown on CE-2, which also has internal backgrounds from ^{138}La and from ^{227}Ac impurities.

3.2 Neutron Detectors

The neutron detector measures the flux of neutrons emitted from a planetary surface which are produced by the continuous cosmic ray bombardment of the lunar surface (Lingenfelter et al. 1961; Feldman et al. 1993).

GCRs have sufficiently high energy to break up nuclei in the surface materials, releasing high energy neutrons. Those neutrons collide with subsurface material and then are slowed down and absorbed by nuclei of elements in the soil. A part of the neutrons escapes and creates a leakage flux of neutrons. Those neutron energies are widely distributed from very high energy to thermal energy.

Neutron energies in nuclear planetology are often divided into three regions: fast ($E_n > 100$ keV), epithermal (0.5 eV $< E_n <$ 100 keV), and thermal energy ($E_n < 0.5$ eV). Thermal energy is defined as the energy below the cadmium cutoff of about 0.5 eV. The neutron detectors sensitive to the energy distribution of neutrons from the Moon observe them from a spacecraft in orbit or at the surface of a planet. The energy distribution of the neutrons provides information about a surface material, such as its composition, and the content of water or carbon oxides.

3.2.1 Thermal Neutron Detection

As neutrons do not cause ionization, they are generally detected through nuclear reactions that result in prompt energetic particles such as protons, alpha-particles and so on. A material with a large cross section for a thermal neutron is used as the target material or a detector medium. Of importance is the Q-value of the reaction that determines the energy liberated in the reaction of neutron capture (Knoll 2000). The higher the Q-value, the greater is the energy given to the reaction products, and the easier the amplitude discrimination is. Materials commonly used for this purpose are gadolinium (^{157}Gd: 255 kb, 15.7%), boron (^{10}B: 3840 b, 19.8%), lithium (^{6}Li: 940 b, 7.40%) and ^{3}He (5330 b). These materials are most likely to react with thermal neutrons. Those reactions are sufficiently exothermic that the kinetic energy of the reaction products is simply determined by the Q-value of the reaction and does not reflect the very small incoming energy of the thermal energy. In the next subsection, typical reactions such as ^{10}B(n, α), ^{6}Li(n, α) and ^{3}He(n, α) that are used to detect thermal neutrons and the detection methods widely used in nuclear planetology are described (Feldman et al. 1998, 2004).

A. The ^{10}B(n, α) *Reaction*

The reaction of thermal neutrons is written as

$$ {}^{10}_{5}\mathrm{B} + {}^{1}_{0}\mathrm{n} \rightarrow \begin{cases} {}^{7}_{3}\mathrm{Li} + {}^{4}_{2}\alpha & Q-\text{value} = 2.792\ \text{MeV (ground state; } 6\%), \\ {}^{7}_{3}\mathrm{Li}^{*} + {}^{4}_{2}\alpha & Q-\text{value} = 2.310\ \text{MeV (excited state; } 94\%), \end{cases} $$

where the branching indicates that the reaction product, ^{7}Li, can be left either in its ground state or in its first excited state. Thermal neutrons ($\sim$25 MeV) are used to induce the reaction; about 94% of all reactions lead to the excited state but only 6% lead directly to the ground state.

B. The ^{6}Li(n, α) *Reaction*

The (n, α) reaction in ^{6}Li is also a common reaction for thermal neutrons. Here the reaction proceeds only to the ground state of the product and is given as

$$ {}^{6}_{3}\mathrm{Li} + {}^{1}_{0}\mathrm{n} \rightarrow {}^{3}_{1}\mathrm{H} + {}^{4}_{2}\alpha, \quad Q-\text{value} = 4.78\ \text{MeV}. $$

Simple calculation for negligible incoming neutron energy yields the following

$$ E_{{}^{3}_{1}\mathrm{H}} = 2.73\ \text{MeV}, \quad E_{\alpha} = 2.05\ \text{MeV}. $$

The alpha- and triton-particles must be oppositely directed when the incoming neutron energy is small.

C. The ^{3}He(n,α) **Reaction**

The ^{3}He gas is also widely used as a detection medium for neutrons through the reaction

$$ {}^{3}_{2}\mathrm{He} + {}^{1}_{0}\mathrm{n} \rightarrow {}^{3}_{1}\mathrm{H} + {}^{1}_{1}\mathrm{p}, \quad Q-\text{value} = 0.764\ \text{MeV}. $$

For the thermal reaction, the Q-value of 0.764 MeV leads to oppositely directed reaction products with energies

$$ E_{p} = 0.573\ \text{MeV}, \quad E_{{}^{3}_{1}\mathrm{H}} = 0.191\ \text{MeV}. $$

3.2.2 Fast neutron detection

Neutron induced nuclear reactions described above convert neutrons to directly detectable charged particles. All the reactions can be applied to detect fast neutrons. However, the probability of the neutron reaction decreases rapidly with increasing neutron energy. As a rule, fast neutron detectors must employ a modified or completely different detection scheme to yield an instrument with acceptable detection efficiency. The most important additional conversion process for fast neutrons is useful in the case of inelastic neutron scattering. In this interaction, the energy of an incident neutron transfers a portion of its kinetic energy to the scattering nucleus, giving rise to a recoil nucleus. The energy transferred from a fast neutron is not small and the resulting recoil nuclei can be directly detected. The most popular and effective target nucleus is hydrogen. Therefore, the resulting recoil protons are relatively easy to detect and serve as the basis for a wide variety of fast neutron detectors (Knoll 2000; Feldman et al. 2004; Harvey & Hill 1979).

One of the easiest ways to use proton recoil in the detection of a fast neutron is the application of scintillators containing hydrogen. Plastic scintillation material is commonly used to make such a device. The material is relatively inexpensive, and can be tailored to a wide variety of sizes and shapes.

3.2.3 Neutron detectors

A. ***Thermal Neutron*** ^{3}He ***Proportional Detector***

^{3}He, with an absorption cross section higher than that of a boron reaction, provides an attractive and effective detector medium for slow neutrons. Because ^{3}He is a noble gas, the detection medium is used in gaseous form. Therefore its sensitivity to gamma-rays is negligible, providing a very useful neutron detector (Feldman et al. 2004; Mitrofanov et al. 2005).

In an ^{3}He proportional tube, one would expect the total deposition of energy, 764 keV, in the form of kinetic energy of the triton and proton reaction products. Because the range of these products is not always small enough to stop the particle in the detection medium, the wall effect of the proportional tube can be important. In order to reduce the wall effect, the detector can be designed 1) with a large diameter so that most neutron interactions occur far away from the wall, or 2) with a high pressure of ^{3}He gas to reduce the range of the reaction products. Because of the low mass of ^{3}He, the ranges of the reaction products are unusually long and the wall effect is relatively large.

B. ***Fast Neutron Detector***

One of the easiest and most useful methods to detect fast neutrons is to use proton recoil in the plastic scintillator containing hydrogen (Harvey & Hill 1979). A plastic scintillator loaded with ^{10}B is often used for the detection of fast neutrons (Mitrofanov et al. 2005; Feldman et al. 2004). A fast neutron suffers multiple scatterings in the scintillator as described before. The neutron loses its energy through the multiple scatterings. Then a series of recoiling protons deposit the energy nearly equal to the incident energy. All the recoiling protons are produced within a short period of time, typically less than 50 ns, because the fast neutron travels at a significant fraction of the speed of light. The neutron continues to diffuse as a thermal neutron and it is eventually captured by boron nuclei. In the event, 2.3 MeV is released as kinetic energy of heavy charged particles, which gives rise to a scintillation pulse. The average time separation between the light produced by the recoiling protons and the light produced by the boron capture products is mostly the diffusion time of thermal and epithermal neutrons in the scintillator, and is typically around 10–20 μs. Neutron detectors were carried to detect thermal, epithermal and fast neutrons on lunar (Mitrofanov et al. 2005; Feldman et al. 2004) and Mars missions (Mitrofanov et al. 2002).

C. A New Type of Scintillation Neutron Detector

Since a significant gamma-ray flux is usually present in the neutron field, good separation of the gamma-ray and neutron signals is required. This may be achieved by using low-density materials that have low gamma-ray sensitivity, or discrimination based on pulse shape is possible. One effective approach is based on materials containing ^{6}Li which absorbs thermal neutrons and produces ^{3}H + ^{4}He with 4.8 MeV of total kinetic energy. ^{6}LiI crystals doped with Eu, ^{6}Li loaded glass, and particularly ^{6}LiF in combination with ZnS: Ag powder have been successfully developed.

Recently, a core valence (CV) scintillator, Cs_2LiYCl_6 which can be doped with Ce, has been investigated (Knitel et al. 1996; Bessiere et al. 2005; van Eijk et al. 2004). In this scintillator, gamma-rays produce both core valence emission ($\sim$1 ns time scale) and self-trapped-exciton (STE) emission ($\sim$1s time scale), while thermal neutrons produce only the STE emission. Thus, the gamma-ray events can be very effectively discriminated based on their pulse shape. Cs_2LiYCl_6: 0.1%Ce also has the advantage of a very high light output of 71 000 photons/n, and $\sim$22 000 ph/MeV for gamma-irradiation. In this respect, Cs_2LiYCl_6: 0.1%Ce comes just after the best current neutron detector LiF-ZnS: Ag (160 000 photons/n) (Crawford 1993). Moreover, the maximum emission wavelength (370 nm) conveniently matches the maximum sensitivity of bialkali PMTs. The decay is characterized by a τ = 6.5 μs which makes Cs_2LiYCl_6: 0.1%Ce almost competitive with LiI: Eu (decay time of 1.2 μs) or LiF-ZnS: Ag for which the pulse pair resolution is $\sim$2 μs (Bessiere et al. 2005). Therefore, Cs_2LiYCl_6: 0.1%Ce does not enable very fast counting rates compared to other neutron detectors. This scintillator is a promising crystal from the perspective of n-γ discrimination.

3.3 X-ray Fluorescence Spectrometer

3.3.1 Principle of X-ray Fluorescence (XRF)

XRF is the emission of characteristic fluorescent X-rays from a material that has been excited by bombardment with high-energy X-rays. The phenomenon is widely used for elemental analysis (Beckhoff et al. 2006), particularly in the investigation of various materials, and for research in geochemistry and planetary science (Adler et al. 1973; Owens et al. 2008; Gellert et al. 2006). When a material is exposed to X-rays with an energy greater than its ionization potential, ionization of the component atom may take place if the atom is exposed to radiation. The removal of an inner electron of the atom makes the electronic structure of the atom unstable, and electrons in higher orbitals "fall" into the lower orbital to fill the hole left behind. In falling, the energy, which is equal to the energy difference of the two orbitals, is released in the form of a photon. Thus, the material emits radiation with characteristic energy. This phenomenon is called fluorescence. The main transitions are given names: an L→K transition is traditionally called K_α, an M→K transition is called K_β, an M→L transition is called L_α, and so on. Each of these transitions yields a fluorescent X-ray with a characteristic energy equal to the difference in energy of the initial and final orbital. The fluorescent radiation can be analyzed by measuring the energy and its intensity in the energy spectrum of the radiation emitted from sample material. This is the basis of a powerful technique in analytical chemistry. The XRF detectors have been used in the Apollo mission (Adler et al. 1973) and in the Mars mission (Owens et al. 2008; Gellert et al. 2006).

3.3.2 X-ray Detectors

In energy analysis, proportional counters or various types of solid state detectors (PIN diode, Si(Li), Ge(Li), SDD) are used. They all have the same detection principle: An incoming X-ray photon ionizes a large number of detector atoms with the amount of charge produced being proportional to the energy of the incoming photon. The charge is then collected and the process repeats itself for the

next photon. Detector speed is obviously critical, as all charge carriers measured have to come from the same photon to measure the photon energy correctly.

The fluorescence process is inefficient, and the secondary radiation is much weaker than the primary beam. The use of a primary X-ray beam to excite fluorescent radiation from the sample is widely used as a non-destructive analytical technique, and as a process control tool in many extractive and processing industries. In principle, the lightest element that can be analyzed is beryllium, but due to instrumental limitations and low X-ray yields for the light elements, it is often difficult to quantify elements lighter than sodium (Z = 11). Detectors need to have high pulse processing speeds in order to cope with the very high photon count rates that can be obtained. In addition, they need sufficient energy resolution to allow filtering-out of background noise and spurious photons from the primary beam or from crystal fluorescence. In the application to planetary science (Gellert et al. 2006), there are two common types of detectors: gas proportional counters and semiconductor detectors (Knoll 2000).

A. ***Gas Proportional Counters***

They are mainly used for detection of X-rays. The gas is usually krypton or xenon at a pressure of a few atmospheres (Knoll 2000; Policarpo et al. 1972). They are usually applied to wavelengths in the 0.15–0.6 nm range. They are applicable in principle to longer wavelengths, but are limited by the problem of manufacturing a thin window capable of withstanding the high pressure difference. The xenon is ionized by incoming X-ray photons, and the electric field multiplies this charge into a measurable pulse. The methane or hydrogen suppresses the formation of fluorescent photons caused by recombination of the xenon ions with stray electrons. The anode wire is typically tungsten or nichrome with a 20–60 μm diameter. The window needs to be conductive and thin enough to transmit the X-rays effectively. Materials often used are beryllium metal, aluminized PET film and aluminized polypropylene. The pulses are sorted electronically by "pulse height selection" in order to isolate those pulses derived from the secondary X-ray photons from being counted. The gas proportional counter has been used in X-ray astronomy (Andresen et al. 1976; Adler et al. 1973) and lunar exploration (Adler et al. 1973; Andre et al. 1977).

B. ***Semiconductor Detectors***

Semiconductor detectors can be used for an X-ray spectrometer. High-purity silicon wafers instead of Si(Li) have become routinely available. Cooled by the Peltier effect, this provides a cheap and convenient detector. Here we describe a silicon detector, such as a silicon $p-i-n$ (PIN) photodiode and SDD (Knoll 2000).

PIN Silicon Detector

Devices employing silicon semiconductors as the basic detection medium became practically available in the early 1960s. Modern detectors are referred to as semiconductor diode detectors. It has come into widespread use to characterize those devices that are based on electron-hole pair collection from semiconductor media. A silicon detector has a superior energy resolution. Even though silicon has a relatively low atomic number of Z=14, photoelectric absorption of incident photons is still predominant in the soft X-ray regions below 20–30 keV. A simple silicon PIN photodiode is a useful X-ray detector (Knoll 2000). A region with high intrinsic resistivity is given with p and n noninjecting contacts to reduce the leakage current. A typical thickness of 250–300 μm is sufficient to provide useful detection efficiency up to 20–30 keV. The small number of electron-hole pairs generated by a soft energy X-ray requires that the noise level of the detector be reduced to an absolute minimum. These detectors are often cooled to further reduce the leakage current to insignificant levels. Cooling down to –10°C$\sim$ – 30°C, using a compact Peltier cooler, is popular. These PIN Si detectors have found sufficiently useful application in the measurement of fluorescent X-rays.

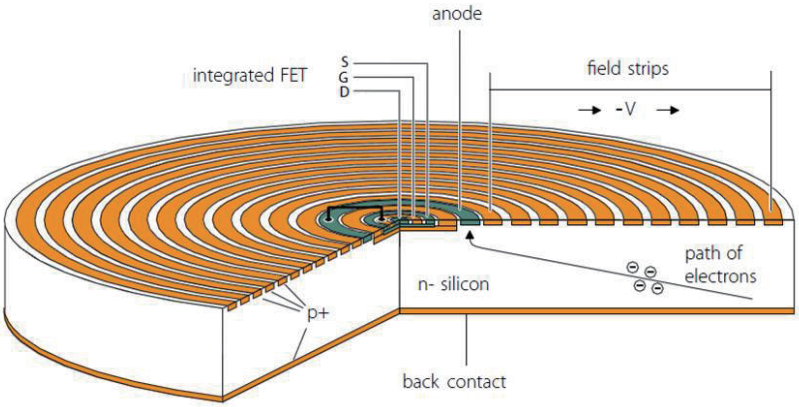

Fig. 5 Schematic Drawing of SDD. It is a circular SDD with a uniform radiation entrance window. The entire thickness of the device is sensitive to radiation. The front end FET with preamplifying electronics is integrated in the center of the ring-shaped anode (*http://www.hll.mpg.de/05_research/res_device-physics.html*).

Silicon Drift Detector

An SDD is a type of photodiode, functionally similar to a PIN Si detector, employing a high purity silicon wafer with a very low leakage current, but with a unique electrode structure to improve performance (Knoll 2000; Lechner et al. 2001, 2004). The major distinguishing feature of an SDD is the transverse field generated by a series of ring electrodes that causes charge carriers to drift to a small collection electrode, when the detector shape is circular (see Fig. 5). The anode centrally located in the circular SDD allows significantly higher count rates coupled with a very low capacitance of the detector. The detector capacitance is always an essentially important factor in determining the noise level of X-ray spectroscopy. The key advantage of the SDD is that it has much lower capacitance than a conventional PIN diode with the same area, therefore, reducing electronic noise at short shaping times.

The small capacitance of a drift detector also leads to an advantage in applications requiring a high counting rate of active fluorescent X-ray spectroscopy combined with an X-ray photon generator. Because the optimal shaping time for minimization of electronic noise shifts to lower values as the detector capacitance is decreased, shorter shaping times are possible that lead to a higher count rate capability for a given degree of pile-up. Combined with improved signal processing, it is possible to maintain the energy resolution even for a high counting rate experiment. An energy resolution of 120–150 eV FWHM at the 5.9 keV Mn K_α line with 25–2.0 μs shaping time can be attained by the SDD with a sensitivity area of 25 mm^2 without cryogenic cooling. For fluorescent X-ray spectroscopy, the SDD has better energy resolution while operating at much higher count rates than a conventional PIN detector (Lechner et al. 2001, 2004; Longoni et al. 2006).

C. Other Semiconductor Detectors

As mentioned before, Ge detectors have an excellent resolution. However, they must be operated at low temperatures (< 90 K) to reduce thermally generated leakage current. In low-noise applications, such as X-ray spectroscopy for low energy deposition in the detector, Si detectors must also be cooled for the same reason. Semiconductor materials with a wider band gap (e.g. > 1.5 eV) are attractive while operating at room temperature, which would probably outweigh the disadvantages

of a wider band gap. A number of semiconductor materials other than Si or Ge have been investigated as radiation detectors.

Among the compound semiconductors, CdTe and CdZnTe have attracted growing interest in the development of X-ray and gamma-ray detectors of space experiments (Owens & Peacock 2004; Toney et al. 1999). Due to their high atomic number Z, high density and wide band gap, CdTe and CdZnTe are considered promising detection media. These detectors have gained great attention from the scientific community interested in the X- and gamma-ray band applications and particularly in the realization of a spectroscopic imager for space and planetary exploration. As demonstrated by several groups in the world working on this technology, many favorable conditions have contributed to CdTe/CdZnTe being regarded as one of the most promising semiconductors for the realization of high performance spectrometers: good crystal growth technology with adequate homogeneity and purity, physical, chemical and thermo-mechanical stability, high mean atomic number and wide band gap are all necessary conditions for obtaining high detection efficiency and functionality at a non cryogenic temperature (Toney et al. 1999; Philps 2006). In particular, good room temperature performance is very attractive for X-ray and gamma-ray applications. The capability of CdTe/CdZnTe detectors in astrophysical applications has already been demonstrated with the European astronomical satellite called the INTErnational Gamma-Ray Astrophysics Laboratory (INTEGRAL) and with the Burst Alert Telescope (BAT) instrument onboard the NASA mission SWIFT (Gehrels et al. 2004).

Diamond detectors have significant advantages, in particular high radiation hardness and very low drift currents. However, they are so expensive and difficult to manufacture that the utilization of diamond as a detector material is still limited to specialized applications. Diamond is an insulating material with a very large band gap of 5.6 eV. At present, diamond detectors are obviously limited to small sizes and they can be operated with a fast response time of several nanoseconds and superior long-term stability. Measurements have demonstrated an energy resolution of 82 keV for room temperature spectroscopy of alpha particles (Canali et al. 1979). Because of their wide band gap, diamond detectors are well suited for operation at elevated temperatures, and their use at 250 °C–300 °C has been reported (Nava et al. 1979). Thin films of diamonds produced by the process of chemical vapor deposition (CVD diamond) are usable as radiation detectors because of their high resistance to radiation damage.

4 NUCLEAR PLANETARY EXPLORATION

4.1 Lunar Nuclear Exploration

4.1.1 Lunar nuclear spectrometer

A. ***Apollo Gamma-Ray Spectrometer***

The Apollo GRSs (AGRSs) were carried on the Apollo 15/16 spacecraft which were launched in 1971/1972. Those missions covered about 22% of the Moon, all within 30° of the lunar equator. The spectrometers were low-resolution NaI(Tl) crystals but produced maps of lunar K, Ti, Fe, and Th (Metzger 1993; Metzger et al. 1973, 1977; Metzger & Parker 1979). The AGRS had a 511-channel gamma-ray spectrometer to determine the composition of the upper 30 cm of the Moon by detecting the 0.2–9 MeV line gamma-rays. The main sensing elements of AGRS, as shown in Figure 6(a), consist of a 7.0 cm by 7.0 cm cylindrical crystal of NaI(Tl) with a 7.6 cm photo multiplier tube, and a plastic mantle for anti-coincidence rejection of charged particles. The crystal was sealed in a stainless–steel can. The detector weighed 3.3 kg, and the electronics weighed 3.2 kg. (Harrington et al. 1974). AGRS was mounted on the end of an 8 m boom. AGRS results helped to settle debates on the global nature of the Moon's composition. They showed that the anorthositic fragments seen in the Apollo 11 soil were the dominant material of the lunar crust, not the KREEP seen in Apollo

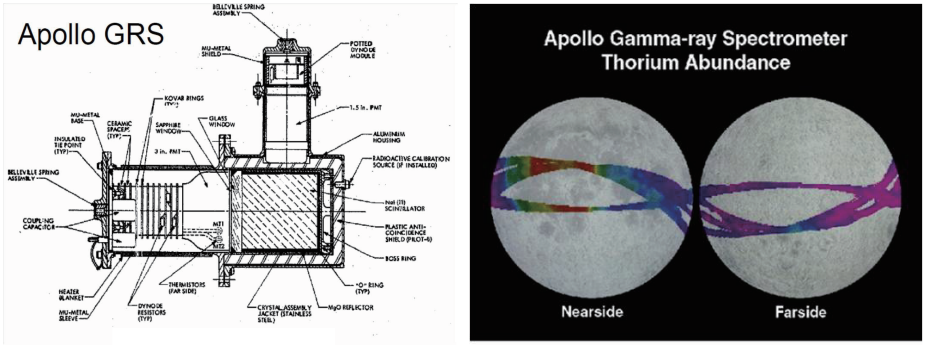

(a) (b)

Fig. 6 (a) The Apollo 15/16 Gamma-ray Spectrometer (from NASA Photo ID: S68-03354 Harrington et al. 1974), (b) the Th abundance measured by Apollo 15/16 GRS (Heiken et al. 1991).

12 and 14 samples, and that the highest concentrations of KREEP are confined to the western maria. The absolute abundances of Th in the highlands had been significant for lunar evolution. The Apollo 15 GRS results also showed that there was a compositional anomaly on the farside, initially called the big backside basin, now called South Pole-Aitken (SPA) basin. The AGRS results helped to establish the Moon's bulk composition, such as its depletion in volatile elements like K. From the Fe surface content, the AGRS data also helped to characterize the thickness and density of the lunar highlands (Haines & Metzger 1980).

The map in Figure 6(b) shows the Th abundance of the Moon. The data are only available for portions of the Moon over flown by Apollo 15 and 16. Red is a high abundance, yellow and green are intermediate abundances, and blue and purple are low abundances. Mare regions on the western part of the lunar nearside show relatively high Th abundance, while mare regions on the eastern part of the lunar nearside have lower Th abundance. The lowest Th abundance is on the lunar farside (Heiken et al. 1991).

B. ***Lunar Prospector Gamma-Ray Spectrometer***

The Lunar Prospector GRS (LPGRS) produced the first global measurement of gamma-ray spectra from the lunar surface, from which were derived the first "direct" measurement of chemical composition for the entire lunar surface. The fundamental purpose of the LPGRS experiment was to provide global maps of elemental abundances on the lunar surface for the natural radioactive decay of elements and major elements in the crust bombarded by GCRs.

Lunar Prospector was designed for a low polar orbit investigation of the Moon including mapping of surface composition and possible polar ice deposits, measurements of magnetic and gravity fields, and study of lunar out-gassing events. The LPGRS as shown in Figure 7 was a small cylinder which was mounted on the end of one of the three 2.5 m radial booms extending from the Lunar Prospector. The orbital altitude was approximately 100 km with a surface resolution of 150 km. It consisted of a BGO crystal surrounded by a borated plastic scintillator (Fig. 7). The gamma-ray energies detected are associated with the element responsible for the emission from the lunar surface material. The precision of elements varies according to each element measured, such as 7% to 15% for U, Th, and K, 45% for Fe, and 20% for Ti (Lawrence et al. 1998).

The LPGRS spectra for the entire Moon and two specific regions are shown in Figure 8. Th abundance measurements of Lunar Prospector are obtained from the LPGRS data by measuring the

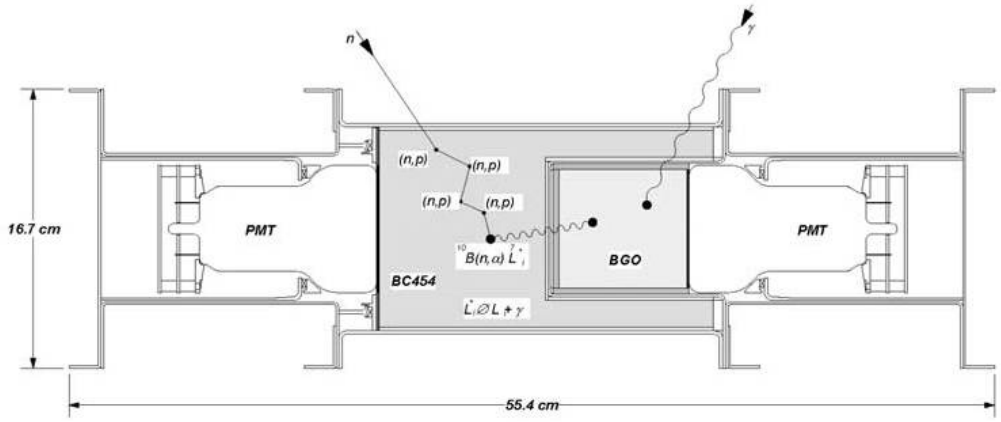

Fig. 7 The GRS on Lunar Prospector (Feldman et al. 2004).

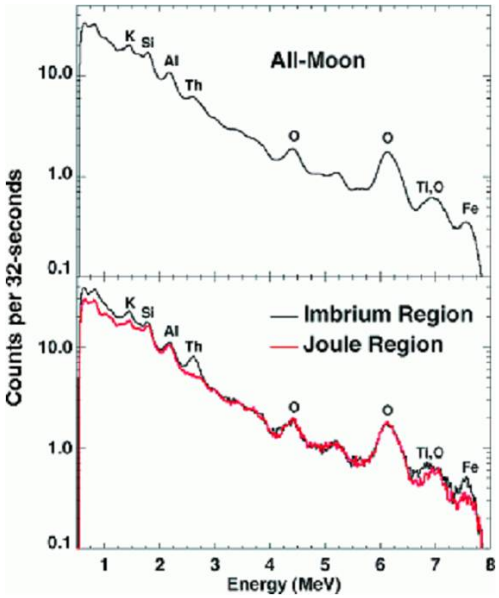

Fig. 8 Lunar Prospector spectra plotted as number of counts per 32 s versus energy. The top panel shows an average of all 356 691 gamma-ray spectra collected during the first 5 months of the mission. The bottom panel shows spectra taken for two regions. The Mare Imbrium and Joule Regions have enriched KREEP and anorthosite, respectively (Lawrence et al. 1998).

counting rate of the 2.6 MeV line produced by the radioactive decay of Th atoms for counting rate data taken over 9-1/2 months from 1998 Jan. 16 to 1998 Oct. 29 (Fig. 9). The data correction of Lunar Prospector includes detector dead time, detector gain, GCR intensity variations and detector response due to latitude variations (Lawrence et al. 1998).

The LPGRS produced the counting rate maps of Th, K and Fe. Th and K are highly concentrated in and around the nearside western maria and less in the SPA basin as can be seen in Figure 8. It

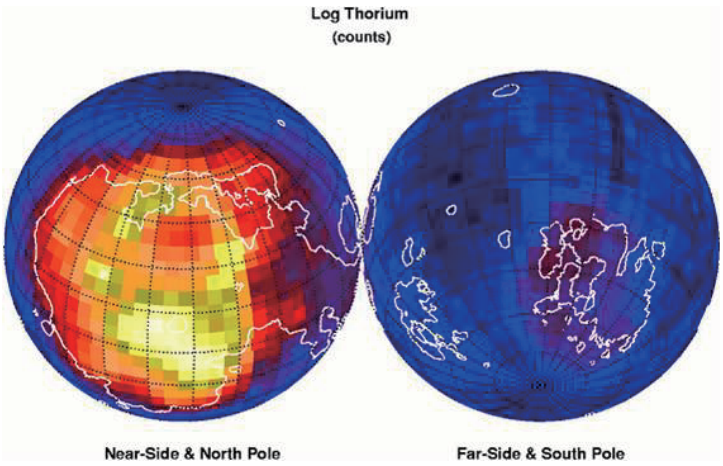

Fig. 9 Two lunar nearside and farside orthographic maps of the Th counting rate obtained by Lunar Prospector are described. The nearside and farside maps are centered on Mare Imbrium and on the antipode to Mare Imbrium, respectively (Lawrence et al. 1998).

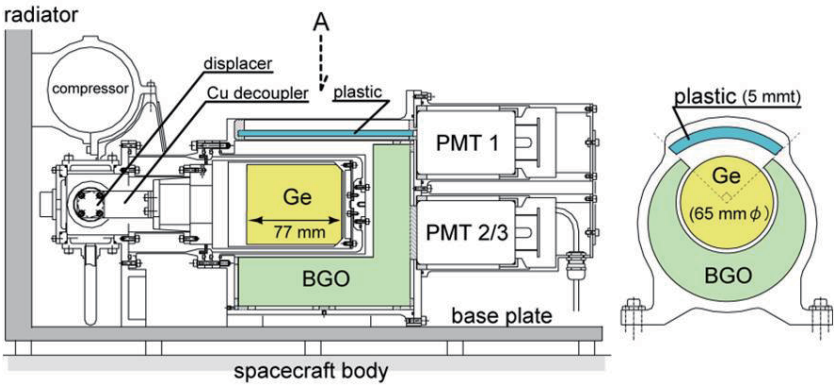

Fig. 10 Schematic drawing of the GRS on Kaguya (Hasebe et al. 2009).

was reported that the counting rate maps of Fe gamma-rays show an Fe distribution on the surface that generally agreed with those from the Clementine and the Lunar Prospector neutron detectors (Lawrence et al. 1998). Various elemental maps of LPGRS were published (Prettyman et al. 2006a). The LPGRS provided maps of the abundances of major oxides, MgO, Al_2O_3, SiO_2, CaO, TiO_2, and FeO and trace incompatible elements, K and Th. The spectral shapes for each elemental constituent were determined by a Monte Carlo radiation transport calculation using new gamma-ray production cross sections for neutron interactions, resulting in improved accuracy compared to results previously submitted to the Planetary Data System. The results of this study include improved accuracy for the abundance of Th and K in the highlands and identification of large regions including western Oceanus Procellarum. The LPGRS result of the high Mg with KREEP-rich regions on the lunar nearside could provide implications for the theory of an early magma ocean (Prettyman et al. 2006a).

C. Kaguya Gamma-Ray Spectrometer

A high precision GRS was carried on Japan's first large scale lunar explorer, SELENE (Kaguya), which was successfully launched by the H-IIA rocket on 2007 Sep 14. This GRS consists of a large Ge crystal as a main detector with massive BGO crystals and a plastic scintillator as anticoincidence detectors (Fig. 10). A Ge detector was firstly used as a main detector in its Kaguya GRS (KGRS) because of its excellent energy resolution. The KGRS has been providing precise global abundance of those elements on the lunar surface by remote sensing and gathering valuable data for the future utilization of lunar resources.

Energy spectra including many clear peaks of major elements and trace elements on the lunar surface have been measured by the KGRS (see Fig. 11). The initial results were observed by KGRS during the period from 2007 Dec. 21 to 2008 Feb. 17. The KGRS data indicate that the region showing the highest count rate of Th, as can be seen in Figure 12(a), extends from Kepler to the Fra Mauro region in the Oceanus Procellarum. Apennine Bench, Aristillus region and the northwestern region of Mare Imbrium are high in terms of thorium count rate. The second high count rate region is located in the SPA basin of the farside. Arago and Compton/Belkovich craters are also enriched in Th (Hasebe et al. 2009; Yamashita et al. 2010).

Maps of the natural radioactive elements (K, U, Th) of KGRS have been published (Yamashita et al. 2010; Kobayashi et al. 2010). A global map of the concentration of uranium on the Moon is shown in Figure 12(b). The KGRS uniquely identified U gamma-ray lines from the Moon with a superior energy resolution of $\sim$1% (Yamashita et al. 2010). It was determined that U-abundances vary up to 2 ppm with an average of about 0.3 ppm. In the case of Th abundance, the average was determined to be about 1.2 ppm. It was also noticed that U/Th ratios varied for the farside of the moon. Also, variation of these elements in the highland area was unexpectedly confirmed (Yamashita et al. 2010). It was found that the present Th distribution on the farside and that on the southern nearside were primarily established at the crystallization stage of the lunar magma ocean. The lowest Th regions are the most probable candidates of the earliest cratons that directly crystallized from the lunar magma ocean, according to the geochemical property of Th during the crystallization stage of the lunar magma ocean. This could be an important discovery in understanding the lunar surface's evolution (Kobayashi et al. 2010). Several major elemental maps are currently being investigated by the KGRS team. These maps will contribute to understanding both chemical abundance of the Moon and evolution of the lunar surface.

D. Gamma-Ray Spectrometers for Chang'E-1 and Chang'E-2

Chang'E-1 is the first Chinese lunar mission which was launched on 2007 October 24. The Chang'E-1 Gamma-ray spectrometer (CGRS) as shown in Figure 13(a) was included in the payload of Chang'E-1 as it orbited at an altitude of 200 km. Specific objectives of the CGRS are to map abundances of O, Si, Fe, Ti, U, Th, K, and perhaps, Mg, Al, and Ca, to depths of about 20 cm.

The Chang'E-2 spacecraft is China's second scientific orbital probe to the Moon and was launched on 2010 October 1. Among seven payloads onboard the spacecraft, a gamma-ray spectrometer (hereafter, CE-2 GRS) manufactured by Purple Mountain Observatory in Nanjing, China, aimed to measure the global element distribution on the Moon. It was the first gamma-ray spectrometer that used a large $LaBr_3$ crystal as its main detector to measure gamma-rays emitted from the lunar surface in the energy range from 0.3 MeV to 9 MeV with the pulse height resolution at room temperature of approximately 4% FWHM at 662 keV. Since CE-2 GRS was mounted inside the spacecraft, a large well-shaped CsI(Tl) crystal was employed in anticoincidence with the main crystal to suppress the Compton effects and reduce the background coming from the GCRs interacting with materials in the spacecraft. The main crystal was read out by a 4-inch diameter PMT while the anticoincidence shield was read out by two 3-inch diameter PMTs. A 512-channel gamma-ray spectrum was recorded after each 3 seconds of accumulation in the 100-km working orbit of the

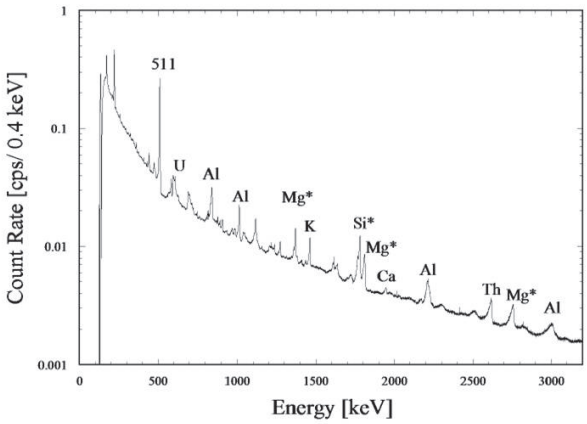

Fig. 11 Energy spectrum of gamma-rays with energies up to 3 MeV measured by KGRS (Hasebe et al. 2009).

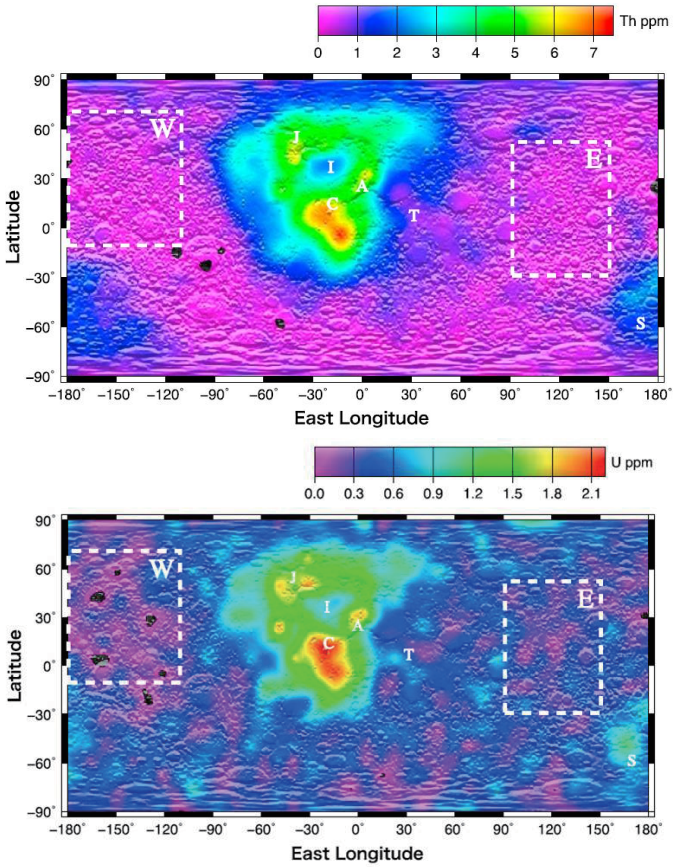

Fig. 12 Global map of Th distribution (*top*) and U-distribution (*bottom*) on the lunar surface measured by KGRS. Their abundances were determined by peak fitting analysis of ^{208}Tl, 2614.6 keV and ^{238}U, 1764.5 keV (Yamashita et al. 2010).

Table 5 The Specifications of the GRS on Chang'E-1/2

Specification	Chang'E-1	Chang'E-2
Main Crystal	CsI(Tl) scintillator (4″)	$LaBr_3$ scintillator (4″)
Anti-Coincidence shield	CsI (30 mm thickness)	CsI (30 mm thickness)
Energy range	0.3 ∼ 9 MeV	0.3 ∼ 9 MeV
Energy resolution	8.3% fwhm@662 keV	3.61% fwhm@662 keV
Spectrum	512 channels	512 channels
Integration time	1, 2, 3s adjustable	1, 2, 3s adjustable
Counting rate	10 kbps	10 kbps
Power dissipation	8.7 W	8.7 W
Mass	31 kg	31 kg
Location	Integrated	Integrated
Orbit	circular polar orbit (200 km)	circular polar orbit (100 km)
Mapping duration	one year	6 months

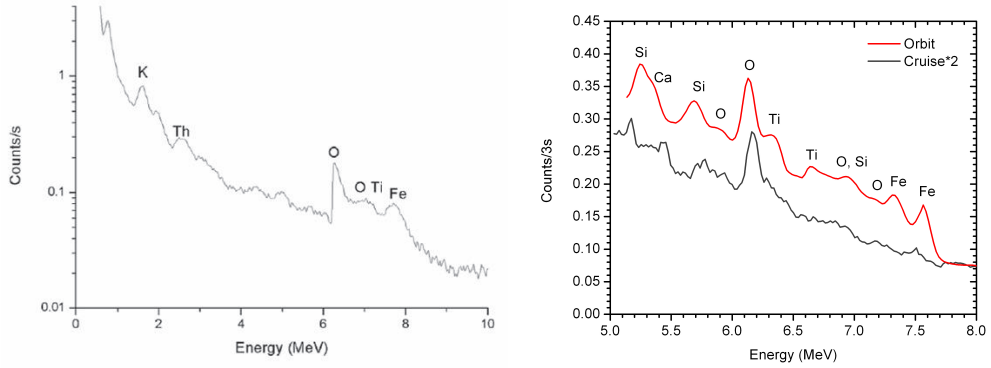

(a) (b)

Fig. 13 (a) The energy spectrum of Chang'E-1's GRS during the first 8 h of 2007 Nov. 28 by the CGRS and Zhu et al. (2010), (b) the energy spectrum of Chang'E-2's GRS during cruise and orbit. The preliminary elemental maps of CGRS-2 have very strong correlation with LPGRS (priv. comm. Zhu 2012; Zhu et al. 2012).

Chang'E-2 spacecraft. In its half-year of detection operation, CE-2's GRS obtained approximately 4500 hours of measurements which could improve our understanding of the elemental distribution on the Moon. After a series of reduction processes, the K, Th, Fe, and Ti maps were derived from the CE-2 GRS measurements. These global maps show great consistency with previous measurements by the GRS on Lunar Prospector, Kaguya, and Chang'E-1. The Al, Mg, O, and Si maps will be given at the end of this year. The specifications of CE-1/2 GRS are shown in Table 5 (priv. comm. Zhu 2012).

The CGRS consists of a GRS and an electronic control box (ECB). The GRS includes central scintillation detectors and a surrounding anticoincidence detector, as well as PMTs. The main GRS is a CsI(Tl) crystal with the dimension of 11.8 cm diameter × 7.8 cm height. It is surrounded on the side and back by a well type CsI(Tl) crystal shield with thickness of about 3 cm (see Fig. 13(a)). The shielding CsI(Tl) counter generates signals by absorption of Compton scattering of gamma-rays from spacecraft and by penetrating charged particles, which inhibit coincident signals from the

central CsI(Tl) counter. Its energy range is from 0.3 to 10 MeV. A sample spectrum of the CGRS data of the Moon is shown in Figure 13(b).

Finally, we describe a high-energy X-γ-ray (30–270 keV) spectrometer (HEX) onboard the Chandrayaan-1 mission. The primary scientific objective of the Chandrayaan-1 mission, launched on 2008 Oct. 22, was to understand the origin and evolution of the Moon based on high resolution selenological and chemical mapping of the Moon. The HEX employed CdZnTe solid-state detectors. HEX has a suitable collimator system providing an effective spatial resolution of 40 km in the low energy region ($<$60 keV). The system includes a CsI anticoincidence system for reducing background and was primarily intended for the study of volatile transport on the Moon using the 46.5 keV γ-ray line from ^{210}Pb decay as a tracer (Goswami & Annadurai 2008).

4.1.2 Lunar Gamma-Ray Spectroscopy

A. Natural Radionuclides

Using gamma-rays from naturally radioactive elements such as K, Th and U to determine absolute abundances is a relatively straightforward process, independent of ground-truth measurements. Since no neutron corrections need to be made to the remotely measured gamma-ray fluxes from orbit, the abundance measurements of these elements in the lunar surface are easier and more reliable than those of major elements such as Fe, Ti, Ca, Si, Mg, Al, O etc.

Gamma-ray fluxes produced by these elements are high enough to be measured from a GRS in lunar orbit. As they are "incompatible" elements, they show similar abundance distributions with each other. The largest flux of gamma-ray lines emitted from the lunar surface is the 1.461 MeV gamma-ray produced by ^{40}K. In spite of this large flux, however, K-abundance is more difficult to measure than the Th-line. In case of the remote gamma-ray measurement by the use of a scintillation detector, the 1.461 MeV K line is not well separated in the gamma-ray spectra. It is close to a number of other large-flux gamma rays such as the 1.368 MeV Mg line. The peak sits on a large gamma-ray background that consists in part of Compton continuum gamma-rays originating from the higher lines, especially from the 2.615 MeV Th line.

Thorium produces a very strong signal in the 2.615 MeV gamma-ray line, which is the second strongest gamma-ray line coming from the lunar surface. The 2.615 MeV gamma-ray is the best separated case in the energy spectra of lunar gamma-rays. Moreover, the 2.615 MeV Th line is located in a spectral region with relatively low gamma-ray background because its energy is rather high in the spectrum produced by radioactive elements. Therefore, the lower energy lines experience interference by the Compton continuum background gamma-rays from the 2.615 MeV Th line, which makes the determination of their fluxes more difficult. In addition to the 2.615 MeV case, other strong Th gamma-ray lines are at 238.6 and 911.2 keV. The 239 keV peak is near the 241.0 keV Th peak that is $\sim$0.1 times as intense as a weak U peak at 242.0 keV. The 911 keV line does not have interferences. These 239 and 911 keV peaks could be used for Th abundance studies.

Uranium produces a number of gamma-ray lines having energies less than 3 MeV. Measurements of U, however, require a high energy resolution and high sensitivity detector because intensities of U gamma-ray lines are much weaker compared to K or Th, and the lines suffer from severe interferences from lines in energy spectra which are only a few keV apart as shown in Figure 14 (Yamashita et al. 2010; Reedy 1978). Conventional gamma-ray detectors used in previous lunar missions of Apollo and Lunar prospector (Harrington et al. 1974; Feldman et al. 1999) had energy resolutions of $\sim$100 keV at 1 MeV and could not uniquely resolve U gamma-ray lines independent of Th and K. The GRS of the Japanese lunar mission SELENE employed a Ge detector that had enough energy resolution, $\sim$1% in full width at half maximum at 1.8 MeV on average throughout the observation, to uniquely identify U lines.

Uranium has its strongest gamma-rays at 609 and 352 keV. However, the 609 keV peak is hard to fit well. The peak is on a big sawtooth peak from ^{74}Ge at 596 keV plus a capture gamma-ray

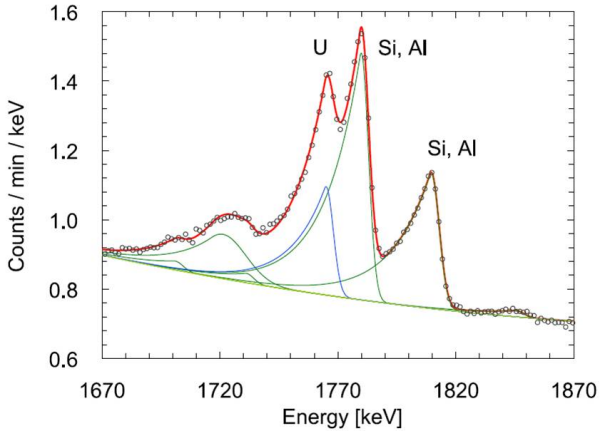

Fig. 14 Peak fitting analysis of gamma-ray lines in the energy spectrum of gamma-rays observed by Kaguya GRS from uranium at 1764.5 keV (After Yamashita et al. 2010).

from ^{73}Ge at 596 keV. The 352 keV U gamma-ray is very close in energy to a ^{56}Fe(n,γ) gamma-ray. That peak is also a part of complex lower-energy weak peaks that makes it hard to estimate the continuum under that peak. Thus, the U gamma-ray at 1765 keV was used to map U in Yamashita et al. (2010). The gamma-ray is emitted as a result of β-decay of ^{214}Bi in the decay chain originating from the decay of ^{238}U (Reedy 1978, 2011). The 1764.5 keV line interferes with a combination of peaks including those from neutron-induced reactions with ^{28}Si and ^{27}Al at 1779.0 and 1808.7 keV respectively, all of which have been successfully removed by peakfitting analysis.

Measurements of K and Th abundances on the lunar surface as shown in Figure 6(b) were firstly obtained using the AGRS (e.g., Bielefeld et al. 1976; Metzger et al. 1977). Maps obtained by these data on the lunar surface are given by Spudis & Pieters (1991) and Metzger (1993). These data provided only 18% coverage over the whole lunar surface. However, many features of the global K and Th distributions were identified. These include the dichotomy in composition of the near-side and far-side, elevated abundances around the crater Aristarchus, the Fra Mauro region, and the Apennine mountains of Imbrium Basin. The western and eastern mare regions (Metzger et al. 1977) have been shown to be roughly the same in terms of the K/Th abundance ratio (K/Th $\sim$400) for KREEP-like materials (Korotev 2000). However, in the Th-poor farside regions, K/Th ranged up to 1800, which is much higher than the near-side values.

The first global maps of K and Th abundances on the lunar surface were reported by Lawrence et al. (1998). Further studies derived absolute abundances of K and Th using low-altitude and both high- and low-altitude lunar-planetary GRS (LPGRS) data (Lawrence et al. 1999, 2000, 2003; Gillis et al. 2004; Warren 2001, 2005; Prettyman et al. 2002a,b, 2006a; Kobayashi et al. 2010; Yamashita et al. 2010; Zhu et al. 2010). Clear peaks from natural radioisotopes of ^{40}K and daughters of ^{232}Th and ^{238}U in the energy spectra of gamma-rays are clearly identified by KGRS. These data delineate the global distributions of key trace elements rich in a component of lunar material called KREEP. The global Th distribution is shown as a typical example. The abundances of the incompatible elements K, Th and U have considerable regional variations over the lunar surface. As can be seen from Figure 9, Figure 12(a) and (b), the nearside tends to record their abundances higher than the farside. In particular, over the Procellarum KREEP terrane (PKT, see Section 6.1.1.1), it is the highest. The SPA terrane also has higher abundances of these elements than the surrounding regions, and the lowest was found in the nearside feldspathic region.

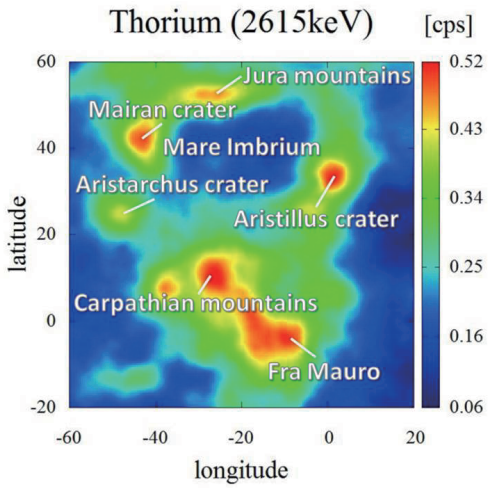

Fig. 15 Intensity map of potassium gamma-rays from the Imbrium basin region. (A) Aristillus crater, (B) Jura mountains, (C) Mairan crater, (D) Aristarchus crater, (E) Carpathian mountains, (F) Fra Mauro (After Hasebe et al. 2010).

These figures present global maps of K, Th and U measured from the Imbium Basin region. Some highly-radioactive regions associated with craters near the rim of Imbrium are seen: e.g., Aristillus and Mairan. Mountains of Jura, Archimedes and Carpathian are also abundant in those elements (see Fig. 15). The wide region from the Carpathian Mountains to Mare Insularum, the Mare Cognitum, Fra Mauro, and the north part of Mare Nubium has very high abundance which makes this region identifiable as composed of ejecta from the Imbrium impact. The abundances of naturally radioactive elements surrounding Copernicus are asymmetric. Relatively high regions also exist near the Aristarchus and highlands north of the Imbrium basin which appears to be Imbrium ejecta. There are regions with high concentrations of radioactivity around the Apennine Bench. Copernicus shows a relatively low abundance of those elements in comparison with the surrounding highest region, which suggests that the lack of a highly-radioactive signature at Copernicus may mean the region happened to be a place where the Imbrium ejecta was lower in those abundances. Ejecta from a large basin such as Imbrium may be rather inhomogeneous in spatial extent.

Despite the fact that most of the lunar highlands have very low K/Th/U abundances, a few locations exist in the lunar highlands that have elevated levels of those abundances. One of these locations is near the craters Compton and Belkovich (60°N, 100°E) (Gillis et al. 2003a). The enrichment suggests this region is dominated by an evolved lithology such as alkali anorthosite (Elphic et al. 2000; Lawrence et al. 2000, 2003; Gillis et al. 2003a).

A global lunar map of U distribution is derived by KGRS for the first time. It was found that U abundances vary up to 2 ppm with an average of $\sim$ 0.3 ppm, while the average Th abundance was $\sim$ 1.2 ppm. From these analyses, significant variation in U/Th ratio was found on the farside of the Moon that had not been reported by previous observations or in lunar materials. KGRS observations suggest that the lunar highland is not as uniform as has been long believed. The U/Th ratio shows small changes between east and west highlands in the farside. However, U is not uniformly distributed in the highlands.

Figure 12(b) reveals a depletion of U in the northern part of the western farside compared to the eastern farside. The Th abundance does not show such variation in those regions.

The correlation between K and Th abundances on the lunar surface determined by KGRS (Kobayashi et al. 2010) is consistent with previous results. The results of the KGRS observations show the ratio K/Th = 346. The result of the KGRS is comparable to the data of lunar materials (K/Th = 397, Korotev 1998), early LPGRS results calibrated by lunar materials (K/Th = 318, Gillis et al. 2004) and the latest results of LPGRS (K/Th = 359–368, Prettyman et al. 2006a).

The maximum K and Th abundances are located near the Fra Mauro region, showing the values averaged in the area of 450×450 km^2 of 2753 ± 401 ppm and 67 ± 1.2 ppm, respectively. The amounts of K and Th in KGRS data analysis are smaller than the values reported by the LPGRS. The maxima of the latest K and Th abundances in the area of 60×60 km^2, 150×150 km^2, and 600×600 km^2 pixels, reported by Prettyman et al. (2006a), were 4400, 3770 and 3300 ppm for K and 11.8, 11.0 and 9.3 ppm for Th, respectively. Comparing the maxima between the KGRS and the LPGRS reported by Prettyman et al. (2006a), the abundances measured by the KGRS are lower by about 20%–30% than those by the LPGRS and are out of the margins of error (Kobayashi et al. 2010).

In the northern farside, K and Th abundances are mostly less than 650 ppm and 1 ppm for 450×450 km^2, respectively. The absolute abundances and their distributions of K and Th in the lunar farside highland are important for checking the Haskin model about the distribution of Imbrium ejecta (Haskin 1998), for deducing the source region of the lunar meteorite with extremely low Th containing clasts of magnesian anorthosites that are believed to be representative of the early lunar crust (Takeda et al. 2006), and for the estimation of the bulk abundance of refractory elements of the Moon (Jolliff et al. 2000; Warren 2005).

B. Major Elements

Prettyman et al. (2002a,b, 2006a) did a comprehensive analysis of high- and low-altitude LPGRS data to derive absolute abundances for major oxides such as MgO, Al_2O_3, SiO_2, CaO, TiO_2, and FeO, and trace incompatible elements such as K and Th of the lunar surface. In this study, absolute abundances were determined largely independently of ground truth; computer simulation and experimental verification of the gamma-ray production and detection process enabled absolute abundances to be derived from the measured LPGRS and Lunar Planetary Neutron Spectrometer (LPNS) data alone. The spectral shapes for individual elements were determined by a Monte Carlo simulation of a radiation transport process in the surface material of the Moon.

Significant results include the improved accuracy for the abundance of Th and K in the highlands and identification of large regions, including western Oceanus Procellarum, that are not well represented by the sample collection, and the association of relatively high concentrations of Mg with KREEP-rich regions on the lunar nearside, which may have implications for the theory of an early magma ocean.

The observations by the neutron spectrometer reflect the presence of Fe and Ti as well as Gd and Sm. The contributions of Fe and Ti are removed using high spatial resolution Clementine spectral reflectance determination of FeO and TiO_2 abundances. The neutron observations also provide constraints on FeO and TiO_2 abundances for some high-Ti locales, but there is a significant disagreement with TiO_2 abundances inferred from Clementine spectral reflectance.

The precision of Mg-data limits their use as a lithologic discriminator of highland rocks. The absence of a high magnesium number indicates that relatively primitive rock types are not present at large scales on the lunar surface. Relatively high concentrations of MgO were found by the LP observation in association with Th-rich regions on the lunar nearside. These Mg and Th-rich data points could represent large-scale surface exposures of magnesian suite rocks, which in turn could have significant implications for the evolution of the lunar mantle. The average magnesium number and abundance of MgO determined by LP for the SPA basin suggest that mantle material is not exposed on a large scale. The basin may consist of a mixture of mantle outcrops and crustal material (Lucey 1998) and/or material from a noritic lower crust (Pieters et al. 2001). The near-side mare

basalt regions have relatively high Mg abundances and relatively low Al, Ca, and Si abundances. In contrast, the far-side highland regions have relatively low Mg abundances and relatively high Al, Ca, and Si abundances.

The remote sensing data described here are generally consistent with sample data and lunar meteorites. Spatial data provided by Lunar Prospector enhance the value of the sample collection, providing added information needed to test theories of lunar evolution.

4.1.3 Lunar Neutron Spectroscopy

Neutron spectroscopy from orbit is used to derive the chemical composition of the lunar surface by measuring a broad range of neutron energies produced by nuclear spallation reactions. These neutrons are generated by nuclear interactions between GCRs and their secondary particles, and constituents of the surface material. An equilibrium velocity distribution is attained as a result of multiple elastic and inelastic collisions. The energy spectrum of those neutrons depends on the elemental composition of the surface material. The neutron energy can practically be divided into three broad ranges of neutron energies that contain compositional information about the lunar surface. The neutrons are referred to as fast neutrons (E >0.6 MeV), epithermal neutrons (0.4 eV < E < 0.6 MeV), and thermal neutrons (E <0.4 eV). Orbital neutron spectroscopy similar to gamma-ray spectroscopy has the limitation of spatial resolution which is around 1–1.5 × the spacecraft's altitude above the planetary surface (Feldman et al. 2000; Kobayashi et al. 2010).

The successful missions to conduct orbital neutron spectroscopic measurements of the lunar surface were the Lunar Prospector mission (Binder 1998) and Lunar Reconnaissance Orbiter (Mitrofanov et al. 2006). The LPNS measured the fluxes of thermal and epithermal neutrons using two ^{3}He gas proportional counters (Feldman et al. 1999, 2004; Maurice et al. 2004). Fast neutrons were measured using signals from the scintillator which was operated as the anti-coincidence counter for the LPGRS (Feldman et al. 1999, 2004).

Gasnault et al. (2001) showed that fast neutron spectroscopy provides average atomic mass of the surface material. Since variations in the atomic mass of lunar material are dominated by variations in Fe and Ti abundances, a global map of fast neutrons looks similar to a combination of the observed Fe and Ti abundances (Gasnault et al. 2001). The flux of thermal neutrons is also highly sensitive to abundance variations of Fe, Ti, Gd and Sm elements across the lunar surface because the cross sections for neutron absorption of those elements are quite large.

Though neutron measurements cannot make individual identification of chemical elements, neutron spectroscopy provides specific elemental abundances. The dynamic range of neutrons is so wide that neutron spectroscopy from orbit provides a very sensitive measure of composition parameters. Moreover, neutrons are very sensitive to hydrogen in the subsurface of a planetary body. As clearly shown by the LPNS, the signals from both epithermal and fast neutrons provide a good way to measure the H content of the lunar surface (Feldman et al. 1998, 2000). Neutron measurements, moreover, provide critical corrections for the analysis of gamma-ray spectroscopic data. Therefore, the simultaneous measurement of gamma-rays and neutrons emitted from a planetary surface, in recent years, has been a standard technique in nuclear planetology.

Natural radioactive nuclides are highly elevated in PKT. An estimation of the surface distribution of rare earth elements (REEs) becomes possible through nuclear spectroscopy of naturally radioactive nuclides because of common aspects of the incompatible elements with the use of neutron measurement. The KGRS, LPGRS and LPNS mapped the global distribution of incompatible elements such as K, Th and U on the lunar surface (Yamashita et al. 2010; Kobayashi et al. 2010; Prettyman et al. 2006a). The REEs, Gd and Sm can be measured by detecting epithermal neutrons (Maurice et al. 2004).

The leakage flux of thermal neutrons from the lunar surface strongly depends on the soil composition. Those materials abundant in elements that absorb thermal neutrons, such as Fe, Ti, Gd and

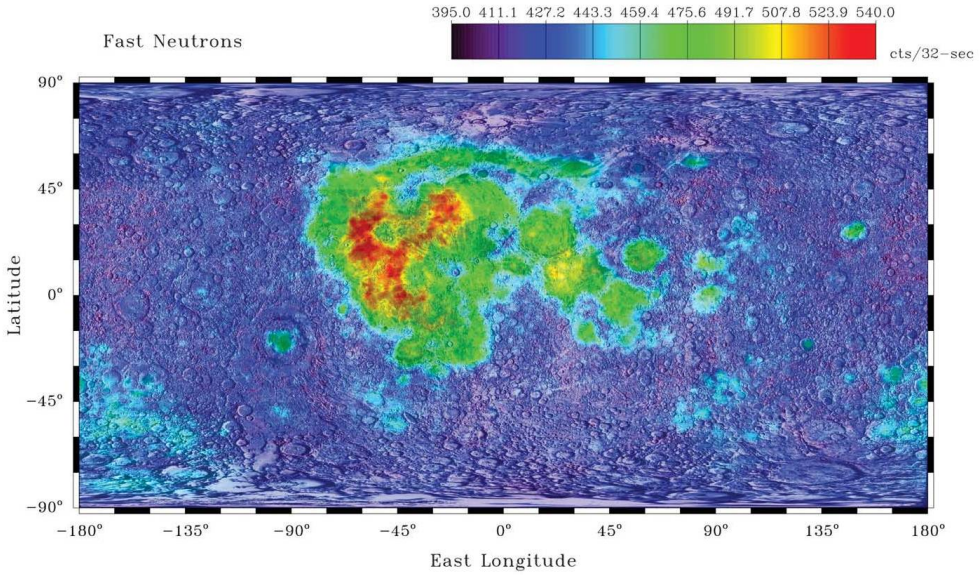

Fig. 16 Global map of fast neutron data, with an optimum smoothness at HWHM = 27 km (unit is counts $32\,s^{-1}$) (Maurice et al. 2004).

Sm, show a lower leakage flux. This is clearly seen in orbital LPNS measurements from the Moon (Fig. 16). The thermal-neutron leakage flux is found to be much lower over the Fe-rich maria than over the Fe-poor highlands, while the epithermal neutron flux is less affected by the presence of such absorbers (Maurice et al. 2004).

The relationship between the epithermal-to-thermal flux ratio and total absorption cross section depends almost entirely on three constituents, Fe, Ti, and the REEs. In general, both REE and Ti concentrations are very low in feldspathic highlands regions. Nuclear spectroscopy can clearly identify and measure the gamma-ray lines from Fe, Ti and Th. If Fe abundance can be determined by gamma-ray spectroscopy, and if the REEs can be constrained by a close correlation with Th as measured by gamma-ray spectroscopy, the Ti abundance can be estimated using the neutron data. After Fe and Ti abundances are estimated, the combined REE concentrations of Gd and Sm can be extracted using this technique. This Ti-detection technique complements that of optical spectral reflectance and gamma-ray spectroscopy.

The first qualitative maps of REE abundance (Gd and Sm) were derived by Elphic et al. (1998). They obtained quantitative estimates using both preliminary Lunar Prospector global FeO abundance based on GRS data, and TiO_2 abundance derived from Clementine UVVIS spectral reflectance data (Elphic et al. 2000). The elemental correlation between LPGRS Th distributions and Clementine TiO_2 ones is good. However, there remains an ambiguous estimate for the TiO_2 abundance showing a factor of two too high, which leads us to reduce the REE contribution in some high-Ti mare basalts (Elphic et al. 2000, 2002; Hasebe et al. 2010).

4.1.4 Lunar X-Ray Fluorescence Spectroscopy

Planetary XRF spectroscopy is the process of measuring the chemical composition of an airless planetary body by observing the characteristic X-ray line emission which results from excitation of the planetary surface material by solar X-rays. The advantage of the XRF includes the ability

to measure elemental ratios and absolute elemental abundances. In addition, XRF measurements provide a better (∼30 km) spatial resolution than gamma-ray and neutron data taken from a similar altitude above the planetary surface (∼150 km), though the spatial resolution of XRF measurements is still broad compared to optical imaging data. The depth sensitivity in the regolith of the XRF technique is in the range of a few to a few tens of microns, which leads us to identify any thin deposit being excavated. Because of the shallow depth response, the XRF technique is complementary to the gamma-ray and neutron techniques that measure compositions down to about 20–30 cm in the regolith. The drawback of XRF is that composition measurements can only be made on the sunlit side of the Moon because of the use of solar X-rays. This limits the potential surface coverage for any XRF mission.

XRF spectrometers were carried on Apollo 15 and 16, Smart-1 (Grande et al. 2007), Chandrayaan-1 (Grande et al. 2009), Hayabusa (Okada et al. 2006) and SELENE (Kaguya) (Okada et al. 2009). However, the only XRF measurements that successfully measured the composition of the lunar surface were the Apollo 15 and 16 XRF instruments (Adler et al. 1973; Clark & Adler 1978; Adler & Trombka 1980; Clark & Hawke 1982; Spudis & Pieters 1991; Yin et al. 1993). They measured the elemental ratios of Mg/Si and Al/Si over 9% of the near-side surface. The results were reported as elemental ratios instead of absolute elemental abundances. Other XRF instruments could not make a map because of small sensitivity due to the radiation damage and low flux of solar X-rays during the solar cycle at solar minimum.

4.2 Mars and Other Nuclear Exploration

The first Martian gamma-ray spectrometer had been incorporated in the Mars Observer. However, the Mars Observer spacecraft had a communication failure on 1993 August 21. This GRS program was restarted with the MOGRS launched on 2001 April 7 and which arrived at Mars on 2001 October 24. The MOGRS conducted a successful mission by determining 20 chemical elements on the surface of Mars, including hydrogen in the shallow subsurface. The MOGRS started its data acquisition with a background measurement for the first six months until May 2002 and its nominal mission about the elemental analysis of Mars started from that time (Boynton et al. 2002). The MOGRS had three spectrometers which are a GRS using an HPGe detector, neutron spectrometers for thermal, epithermal and fast neutrons, and a high-energy neutron detector (Boynton et al. 2002; Feldman et al. 2002; Saunders et al. 2004). Science goals for MOGRS were to understand the origin and geologic evolution of Mars and understanding the distribution of volatiles as well as to find evidence for past climatic variations (Boynton et al. 2004). In order to accomplish these science goals, ratios of bulk elements were measured to constrain the model of planetary formation (Taylor et al. 2006a,b). Also chemical composition of highlands and lowlands as well as regional information about geological provinces were used to understand crust formation and geologic evolution of the surface of Mars (Dohm et al. 2009). A spectrum from the MOGRS was collected every 19.5 s during an orbital cycle of 2 hours at an altitude of 411 km. Until early 2010, Mars Odyssey gamma-ray spectra were collected for over four Martian-years worth of data. The most profound results of MOGRS were finding water in the polar region of Mars as well as in the mid latitude region, producing major elemental maps, and understanding the Martian volatiles and formation of the Martian crust (Boynton et al. 2002, 2007; Taylor et al. 2006a,b). Also, the atmospheric seasonal variation involved in Argon release to the atmosphere and CO_2 thickness change for the polar region were successfully studied (Sprague et al. 2004; Kelly et al. 2006). In addition, confirmation of evidence for an ancient ocean on Mars was possible through the elemental analysis of both natural radioactive elements and Fe, which are associated with water interactions (Dohm et al. 2009).

Besides the Mars Odyssey, various GRS programs were successfully accomplished or are currently being planned for investigation of other planetary surfaces of Venus (Surkov 1977), Mercury (Cheng et al. 1998), Near-Earth Asteroids (Prettyman et al. 2006b), and Ceres and Vesta. The NEAR

spacecraft was successfully launched in February 1996 and has been in orbit around Eros several times. Eros is the largest near-Earth asteroid (Goldsten et al. 1997). This spacecraft maneuvered to within 5.3 km of the surface on 2000 October 26 and finally touched down on the asteroid on 2001 February 12 (Prettyman et al. 2006b). The NEAR GRS was successful in detecting characteristic gamma-rays in the 0.3 to 10 MeV range that are emitted from specific elements in the surface. Gamma-rays induced by GCRs and from natural radioactive elements such as K, Si, Fe, and O were measured using an NaI scintillator detector with a BGO anticoincidence shield (Prettyman et al. 2006b). Also, a recent Messenger GRS (Peplowski et al. 2011a) for Mercury has been successfully collecting gamma-rays from Mercury's surface (Peplowski et al. 2011a). These GRS instruments are much lighter and operate with lower power than previous GRS instruments (Cheng et al. 1998; Prettyman et al. 2003). It is the first interplanetary use of a mechanically cooled Ge detector. Special construction techniques provide the necessary thermal isolation to maintain the sensor's encapsulated detector at cryogenic temperatures (90 K) despite the intense thermal environment near Mercury. The GRS detects gamma-rays in the 0.1 to 10 MeV energy range and the neutron scintillation detectors measure the neutron energy from thermal to 7 MeV (Peplowski et al. 2011a). In the case of GRaND, the gamma-ray and neutron detector of the DAWN mission to Ceres and Vesta, the GRS detector is made of BGO/CdZnTe to detect gamma energy up to 9 MeV (Prettyman et al. 2003). Li-loaded glass and B-loaded plastic neutron detectors measure thermal and epithermal neutron interactions, respectively.

5 DATA REDUCTION

GRS data reduction depends on the detector system because transmission of the data preserves spatial resolution and permits complete flexibility in binning the data according to any desired analysis in terms of time or space. Translating the accumulated pulse height spectra to elemental concentration is complex, requiring knowledge of the relevant background components, the response of the instrument, the geometry of observation, and the production of gamma-rays per unit surface concentration (Pieters & Englert 1993). In the case of low-resolution detectors, response function analysis and energy band analysis are used. For example, NaI and other scintillator detectors broaden the incident gamma-ray lines, and the continuum dominates the spectrum, contributing about 85% of the response, with the precise proportion varying with energy and surface composition (Pieters & Englert 1993). For high-resolution detectors, photo peak analysis is used.

5.1 Response Function of Analysis

The response of a detector to an incident gamma-ray is dictated by the three interaction mechanisms: photo peak absorption, Compton scattering, and pair production, whose relative effectiveness depends on the size, shape, and material of the detector as well as the energy of the gamma-ray. Individual response functions correspond to monoenergetic gamma-rays. A set or library of response functions specific to the low-resolution detector needs to be obtained by measurement with a standard gamma-ray source and Monte Carlo calculation. From one to several gamma-rays may contribute significant emission from a particular element. Individual response functions corresponding to monoenergetic gamma-rays can be added in proportion to their relative intensity to produce a spectrum characteristic of emission from a particular element. This analysis is involved with complexity of the composite discrete spectrum and uses the entire monoelemental response function to characterize a particular element rather than confining the analysis to the area of the photopeak. This technique uses a least-squares fit of the selected library response functions covering the entire energy range of the measurements in the data (Trombka & Schmadebeck 1968). Apollo 16 and Lunar Prospector had low-resolution detectors using NaI and BGO, respectively. The data reduction of these detectors was accomplished using this technique. The library of monoelemental response functions is fitted to the discrete line spectrum by means of a matrix inversion analysis. Subtracting

the total discrete line spectrum from the original spectrum gives a second estimate of the continuum. The process is repeated until a good fit is obtained for both the continuum and the monoelemental response functions.

5.2 Energy Band Analysis

Energy band analysis is associated with low-resolution detectors. For this method, the abundance of a particular element is determined through variations in count rate over a specific portion of the energy spectrum where that element is dominant. This technique is most widely used for the analysis of Th using the energy band from 0.55 to 2.75 MeV. In the energy region above the positron line at 0.51 MeV, up to and including the highest energy line due to natural radioactivity, the 2.61 MeV Th line, the regional differences in count rate are predominantly due to varying concentrations of the radioactive elements Th, U, and K. Since the statistical precision of the total count rate in this region is excellent, the best possible areal resolution can be obtained. The energy band analysis technique analyzes a particular element through variations in count rate over specific portions of the energy spectrum where its effect is strongest (Pieters & Englert 1993). Composition can be obtained by matching a set of net GRS count rates with known surface concentrations. A regression line is defined by the relationship. The perturbing effect of other elements on the band count rate must be evaluated and removed if significant. The energy band analysis employs the integrated count rate over limited energy intervals, does not require separation of the GRS spectrum into line and continuum components, and yields results for one element at a time. This technique can also be used for shorter periods of observation (Pieters & Englert 1993).

5.3 Photo Peak Analysis

A high-resolution detector provides not only better energy resolution, but also peaks in GRS spectra can have a peak to Compton ratio greater than 50, which is about a factor of 10 greater than that for an NaI detector (Pieters & Englert 1993). A high-resolution detector measures peaks that will be resolvable and characterization of the peak is required. MOGRS and SELENE-1 (Kaguya) GRS detectors are made of an HPGe crystal. The number of peaks identified was over 200 (Evans et al. 2002, 2006; Hasebe et al. 2008; Kobayashi et al. 2010). These detectors were calibrated and peak efficiency with respect to energy was investigated. The analysis of photo peaks can be accomplished with peak analysis software. Often the analysis can be done with little user intervention. This analysis is confined to a limited energy range within which one to several elements of interest have photo peaks or escape peak features. The analytic model used to describe the spectral data includes the contributions of photo peaks and/or escape peaks, the continuum and a linear background. The GRS detector for MESSENGER, which was sent to Mercury, is also an HPGe detector. This GRS system will allow us to observe natural radioactive elements and major elements to better understand the surface of Mercury (Peplowski et al. 2011b).

5.4 Spatial Deconvolution Analysis

Spatial deconvolution analysis has been used in GRS data analysis for both Apollo 16 and Lunar Prospector (Pieters & Englert 1993; Lawrence et al. 2007). Because of broad spatial resolution in the GRS data, it becomes difficult to determine the desired elemental abundance of small-scale geologic features. In the case of Apollo 16 data analysis, Aristarchus and its surroundings were the first areas to which the technique of spatial deconvolution was applied (Haines et al. 1978). Besides Aristarchus, regions centered on Mare Imbrium, the Apennine Mountains, Mare Smythii, and the central highlands have also been deconvolved. Each data field has been modeled into about a dozen constructs of varying size and shape. The end product has been not one model, but a family of best

fits that are not distinguishable statistically and show no major variation in model shape. One should note that the improvement in spatial resolution and accuracy is accompanied by 50%–100% loss in precision. The concentration range and uncertainty for a given construct within the family of best fits both decrease with increasing observing time and construct size (Pieters & Englert 1993).

The detailed process of global spatial deconvolution analysis for Lunar Prospector was described using two spatial deconvolution methods: Jansson and Pixon methods (Jansson 1997; Pina & Puetter 1993). Jansson's method is easy to implement in a simple analysis program, but in practice, the iterations are performed to the point where the residual map has the same statistical spread as the noise estimates of the original data. This introduces overfits to the data and risks significant amplification of noise (Lawrence et al. 2007). On the other hand, Pixon's deconvolution technique tries to obtain the smoothest possible image as constrained by both the original data and the data uncertainty (or noise). The Pixon method uses variably sized smooth patches, or Pixon elements, within the image in order to express the information content of the image. This allows successful usage in a variety of image analysis fields, including astronomy, microscopy, and medicine (Puetter et al. 2005). The Th result of spatial deconvolution analysis of Lunar Prospector shows a better result with the Pixon method. The histogram of Pixon residuals shows a mostly Gaussian shape with a width (0.96) that is close to 1 and has an offset that is less than 1% of the standard deviation while the Jansson histogram has a significant negative offset. Both the residual map and histogram show that the Pixon method gives a much more consistent result with respect to the data uncertainties than that from the Jansson result (Lawrence et al. 2007). However, with these techniques, a satisfying determination of Th abundance for specific geological features was not accomplished and complex areas could especially require further investigation with advanced statistical analysis.

6 MAJOR ADVANCES IN LUNAR AND MARS SCIENCE

6.1 The Moon

The Moon is almost unique in the solar system in that it is quite large compared with its primary, the Earth. The average density of the Moon is 3.312 g cm^{-3} which is only about 3/5 that of the Earth. Since lunar surface rocks are essentially the same as those from the Earth, the Moon's interior must somehow be different from Earth's. The Moon has essentially no water and no atmosphere. The dynamic range of temperature in the lunar equatorial region is wide: from –173° shortly before lunar dawn to 127° at midday. Surface temperatures at the lunar pole are much colder, ranging from –258° to –113° due to the very low input of sunlight.

The lunar highlands did not result from an active plate tectonic process. Instead, they simply represent a lack of destruction from bombardments, such as those that formed the lunar basins. The highlands have also been heavily bombarded. However, the large crustal thickness on the farside did not result in lava flows to the surface after impacts and only left large basins. The highest point is on the southern rim of the basin Dirichlet-Jackson (10.75 km) in the highlands on the farside, and the lowest point is inside the Antoniadi crater (–9.06 km) in the SPA Basin (Araki et al. 2009). The lunar highlands are mainly composed of anorthosite which largely includes the mineral feldspar. A recent result of a SELENE (Kaguya) observation shows that anorthosite consisting of nearly 100% anorthosite is widely distributed in the lunar highland crust. It had been conventionally estimated that the lunar highland crust consists of 90% anorthosite and 10% other minerals, wherein pyroxene and olivine also crystallized as well as anorthosite (Ohtake et al. 2009). This implies that the crust of the lunar highland, in the earliest stage of lunar evolution, seems to be formed by materials selectively consisting of only anorthosite.

Basins are different from craters mainly with respect to their size. Basins are lunar impact excavations with diameters of at least 300 km, but craters are smaller than 300 km. Two important basins are the Imbrium Basin and the SPA Basin. The Imbrium Basin was filled with lava and appears as a dark circle on the nearside of the Moon. The SPA Basin on the farside of the Moon is a large impact

crater with a diameter of 2500 km and a maximum depth of 12–13 km, which is the largest known impact crater in the solar system. The impact event that produced this basin could have exposed the upper mantle of the Moon, but more detailed surface analysis is needed to confirm this possibility.

On the face of the Moon, the round, dark, low areas called maria are surrounded by terrane. The lunar basins that contain the maria were probably formed by giant impacts early in lunar history. Those basins were filled with lava by volcanic activity. On the near side of the Moon, the visible maria cover 16% of the surface. The total amount of volcanic material on the lunar nearside covers about 30% of the surface. The rocks of maria closely resemble terrestrial basalts, a type of dark, fine-grained volcanic rock. Many lunar maria are associated with gravitational anomalies called mascons. The strongest mascon anomaly is associated with Mare Imbrium, though they also occur with Serenitatis, Crisium, Humorum, Nectaris and Orientale. It is likely that the lunar crust is thinner below the maria than in other areas, and the dense mantle is close to the surface as a result. These features result from the combination of the increased density of both the surface basalt and the subsurface mantle material.

The Earth, Moon and other planetary bodies in the solar system are continuously bombarded by meteorites and comets which are probably planetesimals left-over from the formation of the solar system. These impacts generate craters that are ten or more times larger than the impacting objects. Most of the lunar surface has remained unchanged for about 4 Gyr. Thus, the solar system's early history of bombardment has been recorded in lunar soils and rocks. The internal form of the crater depends on its size. Small craters ($<$15 km in diameter) are simply bow-shaped depressions. Medium-sized craters, 20–175 km in diameter, have flat floors and a central peak. Craters larger than 175 km have somewhat complex central structures and multiple rings begin to replace central peaks as the size increases.

An interesting and attractive place is the Moon, which records a violent past and has a lot of places to explore. The next step in lunar exploration will be a program of detailed surface explorations and experiments with autonomous and teleoperational robotic explorations before the return of human activity on the Moon.

6.1.1 Lunar Crust

6.1.1.1 Major Crustal Provinces

Both studies of lunar samples and remote sensing data obtained by the Apollo program gave us a broad outline of the nature and geologic history of the Moon. Many previously held beliefs are now being questioned on the basis of global data returned by two US lunar missions, Clementine and Lunar Prospector. In the late 2000s, GRSs on the SELENE (Kaguya) and Chang'E spacecraft confirmed the previous data and gained new findings. Those lunar data obtained in the 1990s and 2000s are being integrated with new and old lunar sample data, to give us new ideas about the nature of the Moon.

As shown in Figure 17, the Moon's crust is divided into three distinct geochemical provinces quite different from the traditional highlands and maria: (1) The PKT, characterized by high Th and Fe, (2) SPA Terrane, which has modest amounts of FeO and Th, and (3) The Feldspathic Highland Terrane (FHT), which includes a somewhat different outer proportion of material (FHT,O); this terrane has low FeO and Th (Jolliff et al. 2000).

These prominent regions on the Moon are defined by chemical characteristics, specifically by the concentrations of FeO and Th. Fe and Th are particularly useful elements, when distinguishing rock types from each other and in monitoring geochemical processes. Mare basalts contain lots of Fe and some Th, but feldspar-rich anorthosites do not contain much of them. Th, one of the incompatible elements, behaves like the REEs that are not incorporated into common minerals. As a result, when

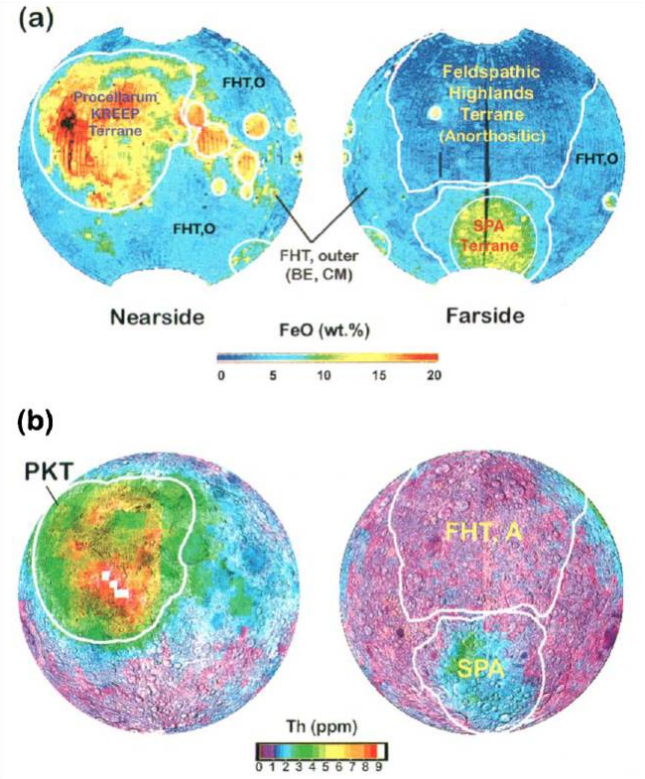

Fig. 17 Three major terranes on the Moon are defined by Jolliff et al. (2000): (1) The PKT, characterized by high Th, (2) SPA Terrane, which has modest FeO and Th, (3) The FHT, which includes a somewhat different outer proportion of material (FHT,O); this terrane has low FeO and Th.

magma crystallizes, Th becomes more abundant in the leftover magma; after the magma ocean has mostly crystallized, it contains about 100 times more Th than the original magma.

Procellarum KREEP Terrane (PKT)

This region is characterized by high K, Th and U concentrations, important components of KREEP, an acronym meaning a lunar chemical component rich in K, rare earth elements (REEs), and P. The PKT is a mixture of assorted rocks, including most of the mare basalts on the Moon, and is characterized by high Th (about 5 ppm on average). This region has also been called the "high-Th Oval Region" and the "Great Lunar Hot Spot." PKT occupies about 16% of the lunar surface. The PKT probably formed when the residual, incompatible-element-rich liquid from the last stages of crystallization of the magma ocean (Taylor & Jakes 1974; Warren & Wasson 1979) intruded into the primitive feldspathic crust. The non-mare parts of the PKT contain 5.4 ppm of Th, 10.6 wt% FeO, and 15 wt% Al_2O_3 (Gillis et al. 2004). These non-mare areas might be contaminated with mare basalts from nearby exposures. Low-K Fra Mauro (LKFM) rocks that were melted upon impact and were found in abundance at Apollo 15 and 17 are associated with the PKT (e.g., Ryder & Wood 1977). They contain 4 ppm Th, 18 wt% Al_2O_3, and 10 wt% FeO (Papike et al. 1998).

The PKT differs from other regions of the Moon primarily by its KREEP-rich geochemistry and extended volcanic history. The Lunar Prospector data demonstrated that the surface abundance of incompatible elements (Th, K, Gd, Sm and the other elements that make up KREEP) are highly

concentrated in this region that encompasses Oceanus Procellarum, Mare Imbrium, and the adjoining mare and highlands (Lawrence et al. 1998, 2000; Elphic et al. 2000). Based on results from Lunar Prospector, the maria exterior to the PKT have Th abundances of ∼2 ppm or less, but the mare regolith within the PKT has Th concentrations between ∼3 and 7 ppm. Highland regions in the PKT, which are inferred to be dominated by Imbrium ejecta, have Th concentrations up to ∼12 ppm. This is consistent with samples that are believed to be derived from this impact basin (Korotev 1998). The Th abundances obtained by the GRS on Kaguya are similar to those of LPGRS (Yamashita et al. 2010; Kobayashi et al. 2010).

In the PKT, the KREEP basalt has an average Th concentration of about 12–13 ppm. This implies that a large portion of the incompatible elements of the Moon (∼30%, Jolliff et al. 2000) are sequestered within this small region of the crust. The origin of the feldspathic upper-crustal component in these breccias that experienced impact-melt is less certain, but one possibility is that this component was similarly derived from the Imbrium target. Under this scenario, the crust of the PKT might best be described as possessing compositionally distinct feldspathic and KREEP basaltic materials, perhaps stratified into the upper and lower crust, respectively (Wieczorek et al. 2006). Many central peaks of the PKT region have broadly anorthositic compositions of $\sim 60 - 90$ vol% plagioclase by spectral analysis (Tompkins & Pieters 1999). Petrological studies of the mafic impact melts suggest that ferroan-anorthositic material might have been absent from both the Imbrium (Spudis et al. 1991) and Serenitatis targets (Ryder et al. 1997). In this case, the feldspathic upper-crustal component in these melt rocks represents a locally derived substrate that was melted and mixed with the primary ejecta of these basins, which provide a possibility that the PKT has a feldspathic chemical component (Korotev 2000).

The PKT reveals viscous relaxation of impact basins. The PKT possesses a high abundance of heat-producing elements of two sites (Apollo 15 and 17). The heat flow of these sites was found to be larger (Langseth et al. 1976). The evidence of higher crustal temperature in the PKT comes from the isostatic state of large impact basins (Neumann et al. 1996). Imbrium, Serenitatis, Grimaldi, and Humorum basins appear to have been in an isostatic state prior to the emplacement of their mare fill (Wieczorek & Phillips 1999). This is consistent with the suggestion of the viscous stress relaxation in the PKT (Wieczorek et al. 2006).

The Procellarum basalts are found to be enriched with incompatible elements based on both LPGRS and KGRS data. The enrichment of incompatible elements and unique volcanic history of the PKT strongly suggest the origin and evolution of this province. The KREEP-rich materials of this region suggest the final dregs of the lunar magma ocean that ultimately accumulated within this region. The crust in this region might have been thinner than typical, perhaps because of a now unrecognizable Oceanus Procellarum impact event. Hydrostatic forces would then have caused KREEP-rich magma sandwiched between the crust and mantle to accumulate beneath this region (Warren 2001). Assuming an average crustal thickness of 40 km for the PKT region, ∼13 km of feldspathic upper crust and ∼27 km of KREEP basalt are estimated. The high abundance of KREEP basalt (∼12.4 ppm Th) could have remained partially molten until at least the time of the Imbrium impact. The slow crystallization of this subcrustal KREEP-basalt layer could have given rise to the Mg and alkali-suite rocks that were likely exhumed by the Imbrium impact event (∼3.9 to 4.4 Gyr). The Imbrium impact event is the last basin forming in the PKT; the Mg- and alkali-suite is not younger than ∼3.84 Gyr (Wieczorek et al. 2006).

The Feldspathic Highland Terrane (FHT) and South Pole-Aitken (SPA) Basin

The FHT is characterized by low FeO (4.2 wt% on average) and very low Th (0.8 ppm). This lunar crust is composed of anothosite and related feldspar-rich rocks that formed about 4460 ±40 Myr (Norman et al. 2003) by flotation from the magma ocean, and represents a pure form of the ancient, primary lunar crust. Jolliff et al. (2000) subdivided the FHT into FHT-A (anorthositic) and FHT-O, which is somewhat richer in FeO and poorer in Al_2O_3 than FHT-A. The LPGRS data indicate that FHT-A has low Th (0.5 ppm) and 4.3 wt% FeO (Gillis et al. 2004). Because FeO is anti-correlated

with Al_2O_3 (Haskin & Warren 1991), this corresponds to an Al_2O_3 concentration of 26.3 wt%. If anorthosite makes up the bulk of this material, most of FHT-A may have lower Th (0.04 ppm) and higher Al_2O_3 (30 wt%–35 wt%). Lunar highland meteorites (Korotev et al. 2003) and lunar granulitic breccias (Cushing et al. 1999) may be representative of the FHT-O. These rocks typically contain 0.4–1 ppm Th, 3 wt%–6 wt% FeO, and 25 wt%–28 wt% Al_2O_3.

The Feldspathic Highland Terrane could have been modified by post-magma-ocean magmatism, because extrusive and intrusive volcanic products are relatively rare in this region. The duration of mare volcanism within the FHT could have been limited primarily to a short period of time within the Imbrian period. The surface of this terrane has been affected by numerous large impact events including the event forming the giant SPA basin. The available evidences may suggest the crust of the FHT becomes more mafic and noritic with depth and the SPA basin could represent the lower crustal materials (Wieczorek et al. 2006).

The SPA basin on the lunar farside has the oldest of the topographically well-preserved lunar impact basins with a diameter of 2100–2500 km and total vertical relief of 12–14 km (Spudis et al. 1994; Wieczorek & Phillips 1999), and it is the largest recognizable impact structure in the solar system. KREEP appears to be low in abundance at this location and divided it into an inner zone (SPA-inner) and an outer one (SPA-outer) (Jolliff & Gillis 2005; Jolliff et al. 2000). The SPA-inner has moderate FeO (average of 10.1 wt%) and Th (1.9 ppm). SPA-outer has less FeO (5.7 wt%) and Th (1.0 ppm). There are no rock samples known to come from the SPA region.

Lucey (1998) indicated that this basin is likely to be a part of a mixture making up the basin floor based on its FeO and TiO_2 concentrations from Clementine data. The absolute FeO concentrations were found to be between $\sim$6 wt% and 12 wt% by the LPGRS, and this indicated that the basin probably penetrated mainly into a noritic lower crust (Pieters et al. 1997, 2001) if mantle rocks are present, or incorporated into the melt sheet if they are not abundant. However, the Clementine multi-spectral data imply that clinopyroxene might be significantly more abundant than previously thought and this suggests a widespread basaltic component mixed with noritic lower crustal materials (Wieczorek et al. 2006). The Th abundance of the SPA basin is about $\sim$2–3 ppm and this is slightly higher than the surrounding highlands ($\sim$1 ppm).

A geophysical model suggests that this basin was not excavated all the way into the mantle which represents approximately 25 km of crustal material. The high-standing topography and inferred crust northeast of this basin has been interpreted as representing the ejecta from an oblique SPA impact (Zuber et al. 1994; Schultz 1997). The SPA could be composed of lower crustal materials and the central peak of Bullialdus is inferred to have a lower crustal origin and it is similar to the floor of this basin. The possibility that the SPA might have excavated into the mantle is still open for further investigation. The floor of this basin could represent a giant impact melt sheet that might have partially differentiated (Morrison 1998) and even if the impact did not excavate into the mantle, this basin could include an impact that melted the underlying mantle (Wieczorek et al. 2006).

6.1.1.2 Crustal Composition and Thickness

The six Apollo missions returned 381.7 kg of lunar rocks or 2196 individual samples, and the Luna missions brought 276 g of lunar regolith to the Earth (Hiesinger & Head 2006). Lunar materials can be classified on the basis of texture and composition into four distinct groups: (1) pristine highland material that contains primordial igneous rocks, uncontaminated by impact mixing; (2) pristine basaltic volcanic rocks including lava flows and pyroclastic deposits; (3) polymict clastic breccias, impact melt rocks, and thermally metamorphosed granulitic breccias and (4) the lunar regolith (Hiesinger & Head 2006).

Pristine highland rocks can be subdivided into two major chemical groups based on their molar Na/(Na+Ca) content versus the molar Mg/(Mg+Fe) content of their bulk rock compositions (Papike et al. 1998). Most highland rocks were forming during the early differentiation of the Moon when upward separation of buoyant plagioclase within a magma ocean produced a thick anorthositic crust.

Taylor et al. (1993) estimated the magnesian-suite rocks make up about 20% of the uppermost 60 km of the crust and the rest is composed of ferroan anorthosite. Non-volcanic rocks and the breccias and regolith derived from them cover about 83% of the lunar surface and it represents over 90% of the volume of the crust. Mare basalts are enriched in FeO and TiO_2, depleted in Al_2O_3, and have higher CaO/Al_2O_3 ratios than highland rocks (Taylor et al. 1991). Mare basalts are enriched in olivine and/or pyroxene, especially clinopyroxene, and depleted in plagioclase compared to highland rocks. KREEP basalts are enriched in incompatible elements and are different from mare basalts, which are formed by remelting or assimilation by mantle melts of late-stage magma-ocean residua, so called urKREEP (Warren & Wasson 1979).

There are two possible interpretations of the Moon's internal structure: (1) just after magma-ocean crystallization and (2) near the end of mare basaltic volcanism. A model with the hemispheric dichotomy in crustal thickness and mare basaltic volcanism represents the crust and mantle as being laterally uniform in composition. The lunar magma ocean is assumed to have a depth of 550 km, and the lower mantle is composed of primitive unmelted materials and a small core is assumed. The sequences of major mineralogy as a function of radius in the mantle (Olivine $\rightarrow$ olivine + pyroxene $\rightarrow$ ilmenite + olivine + Olivine + pyroxene) and crust (plagioclase-rich in upper crust and plagioclase + pyroxene + olivine in the lower crust, as well as the existence of a global KREEP—rich layer at the crust–mantle boundary are a result of a fractionally crystallizing magma ocean. In complex processes, mantle overturn and asymmetric solidification of the magma ocean occurs. The lunar interior at $\sim$3 Gyr is shown in figure 3.1(b) in Wieczorek et al. (2006). This figure shows the distribution of mare basalts and the thickness of the lunar crust.

Seismic data from the lunar surface obtained from the Apollo 12, 14, 15, and 16 stations provide the most direct observation of the crustal thickness. The estimated thickness of Apollo 12 and 14 landing sites were $\sim$60 km (Toksöz et al. 1972, 1974; Nakamura & Koyama 1982). However, recent analysis suggested that the crust of these regions is likely to be between $\sim$27 to 50 km (Khan & Mosegaard 2002; Lognonné 2005). The global crustal thickness estimates show the crust beneath the Apollo 12 and 14 landing sites is thinner than the global average. The inversions for the average crustal thickness using both spatial and spectral techniques suggest an average value of 50 km (Wieczorek et al. 2006). Aoshima & Namiki (2001) obtained crustal thicknesses of $\sim$50 km for basins formed in the PKT, which are basins that satisfy the assumption of a pre-mare isostastic state using localized admittance modeling from the nearside mascons (Wieczorek & Phillips 1999; Hikida & Wieczorek 2007). Also Chenet et al. (2006) estimated crustal thicknesses for 25 locations from seismic data and from comparisons with combined gravity/topography analysis, deriving a mean lunar crustal thickness of 40 $\pm$5 km. Hikida & Wieczorek (2007) employed a polyhedral shape model to circumvent the limitation of the low precision of the farside gravity field to derive an average crustal thickness of $\sim$ 43 km.

The GRSs onboard Apollo 15 and 16 (Trombka et al. 1973; Metzger et al. 1977) and Lunar Prospector (LPGRS) (Lawrence et al. 1998) have shown that the surface of the lunar farside is relatively depleted in Th. However, lunar gamma-ray remote sensing has not been able to specifically determine the Th-distribution in the farside so far, because the Th abundance is very low ($<$1 ppm), approximately a tenth or less of that in the PKT (Jolliff et al. 2000) and the regions with the lowest Th abundance have not been precisely determined on the farside by gamma-ray remote sensing. Kobayashi et al. (2010) recently reported that KGRS has observed the complete lunar surface with the highest energy resolution among all the lunar gamma-ray spectrometers used thus far (Hasebe et al. 2008).

As shown in Figure 18, they defined two regions with the lowest Th abundance on the farside, zone A: Dirichlet-Jackson, Korolev, Hertzsprung, and Orientale, and zone B: the western region of Moscoviense, Mendeleev and Tsiolkovsky-Stark. They showed that those regions coincide with the thickest regions of the crust on the Moon. That is, it shows an inverse correlation between the Th abundance and crustal thickness, when the Th map is superposed on the latest crustal thickness map

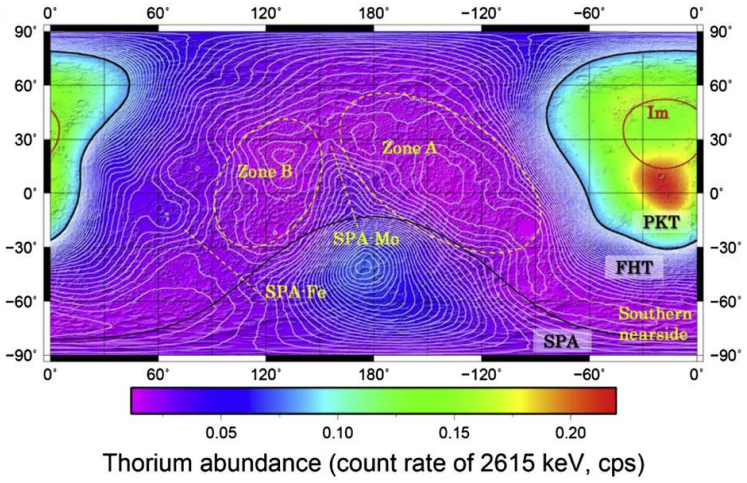

Fig. 18 The distribution of gamma-ray intensity of the Th (^{208}Tl peak at 2615 keV) emitted from the lunar surface measured by KGRS (Kobayashi et al. 2012). The count rate of the 2615 keV gamma-ray peak (counts per second, cps) is displayed, however, it is proportional to Th abundance. The spatial resolution of this map is adjusted to be 900 km. The shaded relief is produced by using Kaguya laser altimeter (LALT) data (Araki et al. 2009).

(Ishihara et al. 2009) calculated by using Kaguya topography and a gravity model (Araki et al. 2009; Namiki et al. 2009). This fact indicates that a large-scale mechanism of crystallization of the lunar magma ocean could be involved in the formation of the lunar farside.

The anorthositic crust composing the lunar highland is believed to be formed in the stage of crystallization from the lunar magma ocean as the result of floatation of low density plagioclase. Th abundance of the anorthositic floatation cumulate depends on Th concentration of the residual liquid, and it generally increases progressively because of the incompatibility of Th. Thus, the earliest craton that crystallized from the lunar magma ocean would have the lowest Th and the degree of crystallization would be related to Th abundance. However, two of the earliest cratons in the northwestern and northeastern regions from the SPA basin seem to be formed directly by crystallization of the lunar magma ocean. The surface Th abundance is inversely correlated to crustal thickness in the latest model of the farside and this is consistent with the geochemical property of Th, which is an incompatible element, during crystallization of the lunar magma ocean (Korotev 1998). The Th abundance of the earliest crust would be lowest according to the crystallization of the lunar magma ocean model (Snyder & Taylor 1993).

6.1.1.3 Petrological Composition

Composition of lunar regolith samples have been investigated by many researchers (McKay et al. 1991; Haskin & Warren 1991; Korotev & Gillis 2001 (Apollo 11); Korotev 1996, 1997 (Apollo 16); Korotev & Kremser 1992 (Apollo 17)). However, there are several problems, such as no Apollo or lunar soil samples for which data are available for all chemical elements (see Fig. 19): As given in the Lunar Sourcebook, there are many samples with fairly detailed and complete analyses, and lunar samples have been measured for only some elements rather than conducting a full investigation of all elements; also the elements had been measured by some laboratories with different techniques, different precisions and systematic errors; measurements of subsamples are not reported, etc (Lucey et al. 2006). Chemical composition of minerals and rocks controlling regolith composition

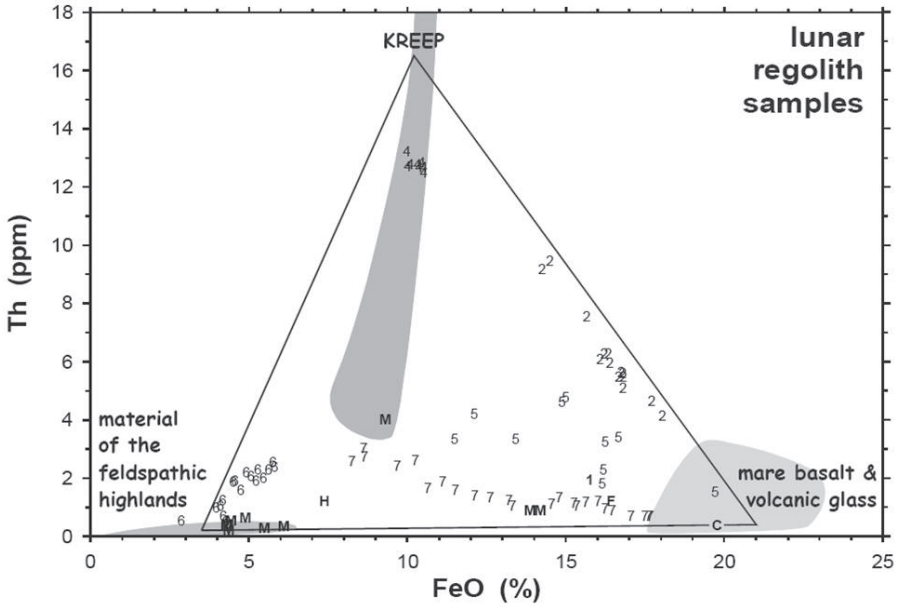

Fig. 19 The Apollo regolith mixing triangle in terms of total Fe as FeO and Th concentrations (Lucey et al. 2006). The numbers stand for Apollo mission numbers, for example: Apollo 17 (7).

was mainly determined by XRF and neutron activation which provide the total concentration of iron regardless of its oxidation state. Since essentially no Fe on the Moon exists as Fe^{3+}, iron concentrations in lunar samples are commonly reported as percent FeO. In the case of lunar breccias and soil from the feldspathic highlands, a significant metallic Fe in the regolith exists, on average, 5.4 ± 1.8 mg g^{-1} of Fe metal ($\sim$0.5 equivalent wt as FeO) (Morris 1980). In mature Apollo 16 soil, there is a high proportion of metal-rich, mafic impact-melt breccias, with about 15% of the iron derived from meteorites (Korotev 1997, 2000) and another 3% being nanophase iron (Morris 1980).

The concentration of Th as a function of FeO(%) has been investigated in terms of the mixing triangle, which shows three distinctive rock types: KREEP, feldspathic highland and mare basalt and volcanic glass (Jolliff et al. 2000). Abundances of Al_2O_3, MgO, TiO_2, CaO, and FeO are also used to classify the three types of lunar regolith. Mare rocks contain much more FeO, MgO, and TiO_2, but less Al_2O_3 and CaO (Fischer & Pieters 1995). Surface mixing cases of KREEP material with volcanic rocks are investigated with Th and FeO. In the case of Apollo 14, Rich concentrations of Th and medium concentrations of FeO ($\sim$12%) are observed. In the case of Apollo 16, both Th ($\sim$10 ppm) and FeO ($<$10%) are clearly seen. For the case of Apollo 15 and 17, a similar pattern of low FeO (mostly) 10% and Th ($\sim$15 ppm) is seen, however FeO content as high as 20% is seen (Korotev & Kremser 1992; Jolliff et al. 1996). This is due to sample collections at various sites such as inside and outside the crater, as well as at the rim of the crater (Jolliff et al. 1996, 1998). Depth profile of the regolith shows the compositional variation. Oxygen and SiO_2 variations in the lunar regolith are from 41% to 47% and from 37% to 48%. For TiO_2 the variation is from close to 0 to about 10% at various FeO% from 4% to mostly 17%. In the case of MgO with low FeO% (5%), variations in MgO% from 4% to 6% are found for mare rocks and samples from Apollo 16. For higher percentage values from about 10% to 17%, FeO(%) and TiO_2(%) variation rises from 8% to 11% (Jolliff et al. 1996, 1998; Korotev 1987).

6.1.1.4 Volcanic activity

The Moon can be regarded as a solitary planetary body that had volcanism resulting from the melting of mantle rocks without recycling the crust. This melting process was caused by the decay of natural radioactive elements and resulted in the production of partial melts, most commonly with basaltic composition (45%–55% SiO_2 and relatively high MgO and FeO contents) (Hiesinger & Head 2006). For the melting process of the Moon, temperatures above 1100°C and depths of about 150–200 km would have been required. Radiometric dating of lunar samples indicated that most volcanism on the Moon ceased approximately 3 Gyr ago. However, crater counts on mare basalt surfaces indicated that some basalt erupted as late as ∼1.2 Gyr ago (Hiesinger et al. 2003). Recent modeling of the thermal evolution of the Moon suggested the growth of a 700–800 km thick lithosphere while the lower mantle and core only cooled 100° C–200°C (Spohn et al. 2001). The zone of partial melting is necessary for the production of basaltic magmas, and the magmas would migrate to depths too great for melts to reach the surface at ∼3.4–2.2 Gyr ago. Lunar Prospector data indicated the extent of a non-uniform distribution of heat-producing elements in the mantle that produced melting during more recent times (Hiesinger & Head 2006).

As shown in Figure 20, the lunar basaltic lava covers about 17% of the lunar surface and 1% of the volume of the lunar crust (Head 1976). Most basalts are located in the nearside basins and form relatively smooth dark areas and they appear to be associated with the distribution of KREEP in Oceanus Procellarum (Wieczorek & Phillips 2000; Haskin et al. 2000a,b). Besides these lava flows, other products of basaltic volcanism, like fire fountaining driven by gas exsolution from erupting lava that is dispersed melt as fine droplets in the form of pyroclastic deposits or volcanic ash (Chou et al. 1975; Delano & Livi 1981; Delano 1986).

Volcanic features on the Moon are identified as lava flows, sinuous rilles, cryptomaria, volcanic centers, domes, sills, shields, cones, lava terraces, and pyroclastic deposits. The absolute dating of specific rock samples indicated that significant periods of time elapsed between basin formation and extrusion of mare basalts into the basin. In the case of Imbrium basin, the basin is thought to be 3.85 Gyr old but the lavas sampled at the Apollo 15 site show the age is 3.3 Gyr and deeper buried samples could be much older (Hiesinger et al. 2000, 2003). The total volume of volcanic products can be used to estimate the amount of partial melting and how much of the lunar mantle was involved in the production of the mare basalts (Head & Wilson 1992). The thickness of basalts on the lunar nearside is determined to be deeper than 1.5 km (Dehon & Waskom 1976). The ponds in the SPA basin were interpreted to be single eruption phases with volumes ranging from 35 to 8745 km^3 and averaging 860 km^3 (Yingst & Head 1997). From a study of 58 mare flow units in the major nearside basins, Hiesinger et al. (2003) found that the range of volumes is 30–7700 km^3. The minimum and maximum average volume of all investigated flow units was estimated to be ∼590 km^3 and ∼940 km^3, respectively. The returned samples revealed the mare volcanism was active at least between ∼3.9 and 3.1 Gyr (Head 1976; Nyquist & Shih 1992), However, some basaltic clasts in older breccias show an onset of mare volcanism prior to 3.9 Gyr (Ryder & Spudis 1980), perhaps as early as 4.2–4.3 Gyr in the Apollo 14 region (Taylor et al. 1983; Dasch et al. 1987; Nyquist et al. 2002).

6.1.1.5 Water at the Polar Regions

M^3 onboard the Chandrayaan-1 discovered water not only at the polar regions but also outside the polar regions by observing the signature of water by an optical instrument (Pieters et al. 2001). In addition, the recent lunar missions of LCROSS and LRO provided several clear evidences for the existence of water in the lunar polar regions (Schultz et al. 2010; Colaprete et al. 2010; Gladstone et al. 2010; Paige et al. 2010; Hayne et al. 2010; Mitrofanov et al. 2010). The successful discovery of water using nuclear technology was accomplished only with the neutron spectrometer on Lunar Prospector and LRO by LEND (Feldman et al. 1998; Mitrofanov et al. 2010). Lunar Prospector's

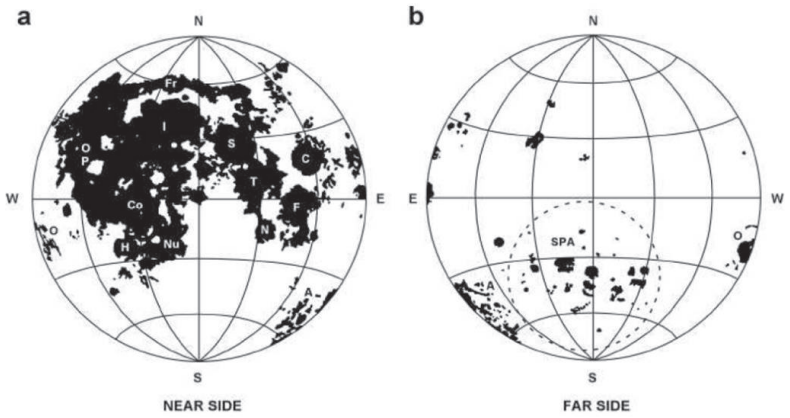

Fig. 20 Map of the distribution of mare basalts on the lunar nearside surface (a) and the farside surface (b). The letters indicate volcanic provinces: A: Australe, C: Crisium, Co: Cognitum, F: Fecunditatis, Fr: Frigoris, H: Humorum, I: Imbrium, N: Nectaris, Nu: Nubium, O: Orientale, OP: Oceanus Procellarum, S: Serenitatis, SPA: South Pole-Aitken, T: Tranquillitatis, after Head (1976).

neutron detector provided this distribution map of water in the polar regions. The abundance of water was determined to be 4.6% and 3.0% for the north polar region and the south polar regions, respectively. The detection limit of the neutron detector on the Lunar Prospector was known to be 0.01% for water. The Lunar Prospector neutron data confirmed that nearly pure water ice is buried beneath as much as 40 cm of dry regolith (Feldman et al. 1998). The Lunar Exploration Neuron Detector onboard Lunar Reconnaissance Orbiter (LRO) also confirmed the existence of water in the polar regions. The impact side of LCROSS inside the Cabeus crater showed the highest concentration of hydrogen in the lunar south polar regions, corresponding to an estimated content of 0.5% to 4.0% water ice by weight, depending on the thickness of any overlying dry regolith layer (Mitrofanov et al. 2010). In the case of Kaguya's GRS, the signature of H, which was a 2223 keV gamma-ray peak in the polar regions, was not clearly identified because of interference by a nearby peak, Al (2212 keV) (Hasebe et al. 2009).

6.1.2 Lunar Mantle

There is no sample identified as the lunar mantle (Wieczorek et al. 2006). The origin of the mantle materials would be related to partial melting deep within the lunar mantle and their compositions reflect that of the mantle at the time they formed. Basalt and volcanic glass compositions combined with experimental petrology can infer the depths of origin and compositions of the mantle source regions (Wieczorek et al. 2006). The major mafic mineralogy (olivine, pyroxene, Fe-Ti oxides) of basalts can be determined from orbit and FeO and TiO_2 as well as other elements such as Th, K, U, Fe, Al, Ca, Mg, etc. which can be determined by the Clementine UVVIS data and GRSs (LPGRS/KGRS), respectively. FeO concentrations of the main mare basalt groups from Apollo and Luna samples range from 15.5% in the aluminous basalts to $\sim$23 wt% in the Luna 24 ferrobasalts, and Apollo 15 olivine basalts have a range of 18 wt%–21 wt%. Concentrations of FeO in the volcanic glasses are slightly higher with a range of 16 wt%–24 wt%, and averaging $\sim$21 wt%. Concentrations of TiO_2 range from $<$1 wt% to 13 wt% in the high –Ti basalts and to 17 wt% in the high-Ti volcanic glasses (Wieczorek et al. 2006). REE content of mare basalt and nonmare crustal materials was a key to understanding the basic relationship between the crust and mantle of the Moon (Taylor

1975). The formation of a negative Eu anomaly can also occur from the crystallization of mafic silicates (McKay et al. 1991). The general variations in REE patterns between mare basalts, feldspathic crustal lithologies and KREEP-rich materials are consistent with the simple magma-ocean scenario (Wieczorek et al. 2006). The divalent and trivalent trace transition metals (ferromagnesian trace elements) are generally compatible with mare basalts. Chromium tends to be enriched in basalts that have the highest Mg/(Mg+Fe) and contain magnesian olivine and spinel, and its concentration decrease in basalts with progressively higher Fe/Mg ratios. Concentrations of Cr are higher in the volcanic glasses (2000–8000 ppm) than in the crystalline basalts (1000–6500 ppm). Ni and Co tend to be correlated inversely with the incompatible element and are in highest concentration in the most primitive olivine-rich basalt, reaching concentrations of 90 and 70 ppm, respectively (Wieczorek et al. 2006). Mare basalts exhibit distinctive mineralogical, chemical and isotopic characteristics that reveal major features of their mantle source. The mineralogical (Fe metal) and chemical (reduced valence states for Fe, Ti and Cr) signatures of the mare basalts reflect extremely low oxygen fugacities. In the crystalline mare basalts, the depth of a negative Eu anomaly increases with increasing TiO_2.

Understanding the trace-element contents of mare source regions is important. One example is that K, U, and Th contribute to remelted mantle materials long after solidification of the magma ocean. Differences in the style of eruption of the volcanic glasses and mare basalts may be related to their volatile contents, depth of origin, and whether or not the sources were undifferentiated and thus volatile-rich, which is related to the cumulated upper mantle (Wieczorek et al. 2006). A recent study showed that some volcanic glasses may have source regions at depths below the differentiated cumulate mantle, and trace-element measurements suggest the possibility that garnet may occur in their residue (Neal 2001). Signatures of high Y and REE are associated with high garnet. Volcanic glasses are associated with the ratio of Sm/Yb being greater than 1 and 1.25 respectively, with KREEP being intermediate. Garnet was a residual component after the cessation of partial melting (Neal et al. 1988, 1989a,b; Neal 2001). The lunar mantle is believed to be extremely dry and volatile poor (Gibson 1977). Its low C content of mare basalts has been attributed to the low C content of their source, the low solubility of diffusion and evaporation (Fogel & Rutherford 1995). The sulfur concentrations of crystalline mare basalts range from an average of 400 ppm in some of the Apollo 15 low-Ti basalts to 2600 ppm in the high-Ti basalts from Apollo 17 (Delano 1986).

Based on the Apollo seismic data, the depth of the upper lunar mantle is roughly 500 km (Khan & Mosegaard 2002). In the transition zone, at a depth of 560 ± 15 km, there is a substantial increase in velocity of P and S waves. (Khan & Mosegaard 2002). The shallow moonquake hypocenters are distributed in the depth range from 50 to 220 km (Khan et al. 2000), confirming that the upper mantle is a source of tectonic activity (Nakamura et al. 1979). Also, the deep moonquake hypocenters have indicated a well-defined source region in the depth range of $\sim$700–1150 km. The Nakamura & Koyama (1982) model demonstrated that there are three layers composing the mantle (a 500 km orthopyroxenite upper mantle, and a garnet-bearing olivine and clinopyroxene mantle below 500 km). The upper mantle shows 95 mol% orthopyroxene and 4 mol% clinopyroxene between the crust and a depth of 270 km, and about 92 mol% orthopyroxene, 4 mol% clinopyroxene, 4 mol% olivine and 1 mol% garnet between 270 and 500 km. For this model, the magnesium number decreased from 84 at the base of the crust to 73.5 at a depth of 270 km. The bulk crustal composition was investigated by Taylor (1982). The transition between the upper and lower mantle occurred near a depth of 600 km. The upper mantle was found to be an orthopyroxenite, containing $\sim$75 wt% othopyroxene, a relatively unconstrained amount of clinopyroxene, trace amounts of olivine, and depending upon depth, either plagioclase or garnet. Above a depth of about 200 km, plagioclase was stable with abundances less than about 10 wt%, and below this depth, garnet was present with abundances near 15 wt%. Below a depth of $\sim$600 km, the mantle seems to be composed of approximately 60 wt% olivine and 40 wt% garnet. The magnesium number is found to increase from $\sim$66 in the crust to $\sim$75 in the upper mantle, and to $\sim$89 beneath a depth of 600 km (Wieczorek et al. 2006).

6.1.3 Bulk Composition

Chemical composition data obtained by remote sensing observations, the Apollo sample returns and lunar seismic data provide important keys to estimate the bulk composition of the Moon. LPGRS measurements of Mg, Al, Ca, Si, and O have provided major elemental maps of the Moon and natural elemental maps of Th and K were published (Prettyman et al. 2006a). The general behavior of the elemental abundance maps shows that the near-side mare basalt regions have relatively high Mg abundances and relatively low Al, Ca, and Si abundances. The far-side highland regions have relatively low Mg abundance and relatively high Al, Ca, and Si abundances. The O abundances do not exhibit much variation with a narrow range of near 44%. In the case of Kaguya GRS measurements, natural radioactive elemental maps of K, Th, and U have been published (Kobayashi et al. 2010; Yamashita et al. 2010). The trends of the natural elemental maps between LPGRS and KGRS are similar to each other.

The crust and mantle of the Moon can be estimated by the bulk composition of the Moon. Th and Al abundances are a key to deciphering the bulk composition and origin of the Moon. The bulk composition of Al_2O_3 and Th abundances are known to be 6 wt% and 125 ppb, respectively (Taylor 1982). A lunar mission with remote sensing techniques would allow us to obtain major oxides and incompatible elements. Some recent mass-balance calculations based on surface remote sensing data were found to be similar to the value estimated by Taylor (1982) (Jolliff & Gillis 2005; Warren & Humphrys 2003).

Recent reanalysis of the Apollo seismic data has revised the crustal thickness at the Apollo 12 and 14 sites down from 60 km to 45.5 km (Khan et al. 2000), 39$\pm$3 km (Khan & Mosegaard 2002), and 30$\pm$2.5 km (Lognonné 2005). The concentration of Al_2O_3 in the lower crust is known to be less feldspathic. The lunar bulk Al_2O_3 abundance in the crust is found to be between at 1.2 wt% and 2.2 wt% for the average thickness of 30 to 60 km. (Wieczorek et al. 2006). Kuskov & Kronrod (1998) presented two best-fit models of chemical composition for mantle seismic velocity layers of (58–270 km, 270–500 km, and $>$500 km) and their concentrations corresponded to 2.5 wt% and 2 wt% for the upper mantle, 3.1 wt% for the middle mantle, and 5.1 wt% and 5.3 wt% for the lower mantle. Assuming a 50 km-thick-crust, a metallic core of radius 350 km, and a constant density mantle, the model of Kuskov & Kronrod (1998) gives the bulk lunar Al_2O_3 abundance of 3.3%$\sim$3.6% whereas the model of Khan et al. (2006) gives 6.8 wt%. By employing the minimum mantle Al_2O_3 abundance of Kuskov and Kronrod and the minimum crustal abundance, the minimum bulk lunar Al_2O_3 concentration is about 45 wt%. This is greater than the value of $\sim$3.6 wt% for the bulk silicate of Earth (Taylor 1992), but is less than the value of 6 wt% that was advocated by Taylor (1982) for the Moon.

Thorium concentrations are found to be less than 1 ppm in the upper crust and about 2 or 3 ppm in the lower crust. Assuming the thickness of the lower crust to be 25 km, its bulk composition is 1 ppm with an uncertainty of 30 ppb (Wieczorek et al. 2006). A plausible range of bulk Th abundance for the PKT is between 4 ppm and $\sim$7 ppm, corresponding to a 50-50 mixture of KREEP basalt and feldspathic materials. Assuming the crust of the PKT is on average 40 km thick, and that it occupies 10% of the surface area of the Moon, an uncertainty of 3 ppm Th for the PKT would correspond to an uncertainty in the bulk Th abundance of the Moon of $\sim$20 ppb. Because the bulk Th abundance is based on remote sensing data, the uncertainty could be as large as a maximum error of $\sim$100 ppb (Wieczorek et al. 2006).

6.2 Mars

The technology of nuclear planetology has been implemented from the beginning of Mars exploration to investigate its surface. From the Viking mission to the very recent Mars Exploration Rover, science payloads that used nuclear technology have played major roles in the investigation of ele-

mental features on the planetary surface. This section summarizes the discoveries of Martian features using the science payloads of gamma-ray, neutron, and X-ray spectrometers.

6.2.1 Mars Geological history and features

With GRS data, it is possible to see very shallow elemental features several tens of centimeters beneath the surface. This depth is much greater when compared to the measurements with an X-ray or optical spectrometer. Using the MOGRS data, major elemental maps of water, Si, Cl, Fe, Th, K, and Ca have been successfully produced, and more detailed maps are currently being investigated by the MOGRS team.

The global elemental maps are useful in understanding geological evolution and current features by comparing with the visible or optical remote sensing data. Most of the Martian surface is covered with dust particles. MOGRS data of silicon show that the Si concentrations mostly vary from 19% to 22%. In the case of Tharsis Montes and Olympus Mons, it was found to be about 18%. The uncertainty in Si data ranged from about 0.3% to 0.6%, and this is due to the difference in attenuation of the signal from the atmosphere. Regions with higher elevation regions tend to have lower uncertainties (Boynton et al. 2007).

In the case of Cl, the regions with substantial concentrations are found to be in the Medusae Fossae Formation (see Fig. 21). This enrichment may be associated with ignimbrite deposits in this area or due to Cl-rich volcanic gases. Also, moderately high amounts of Cl are found to be in Arabia Terra and in a band that follows the dichotomy boundary west of Tharsis Montes (Boynton et al. 2007). It was observed that there was some correlation between Cl and the signature for water in the mid-latitude regions. The highest water concentrations over Arabia Terra, in the Medusae Fossae Formation and near Apollinaris Patera are also associated with high concentrations of Cl. This demonstrates that, except for the region of the Medusae Fossae Formation, formations in other regions could be due to a close relationship between Cl and water through a weathering process (Boynton et al. 2007).

MOGRS data show Fe concentrations distributed from 10% to about 20% with uncertainty of 0.6% to 2.2%. The Fe enrichment in the northern lowlands for the 0 km elevation contour is clearly visible. This could be related to Fe leach from the surface so that it could be ultimately transported to the lowlands via hydrologic activity. This feature can be seen in the terrestrial case. The K and Th concentration on the surface of Mars is distributed from approximately 0.2 to 0.6 (ppm) and 0.1 to 1.0 (ppm), respectively. Also, the K and Th contents are found to be low in areas of young volcanic flows, Hadiaca Patera, the area east-southeast of Elysium Mons, Syria, and Solis Planae. This suggests the early crust formation could have been enriched in incompatible elements with the later magmas being derived from a depleted mantle. The enrichment of K and Th in the northern lowlands corresponds closely to the surface type-2 region (very silica-rich) (Bandfield et al. 2000). Part of this high-K region is masked by a unit to the northwest of Elysium Mons in the area that closely matches the region mapped as a series of lahars (Christiansen 1989).

In addition to gamma-ray data, X-ray analysis of surface investigation has played a major role in unraveling the bulk composition of Mars as well as the geological history of its surface. From the Viking mission, the X-ray spectrometer became a major science payload for surface investigation of a rover or a lander. By providing an active X-ray source, XRF on the Martian surface was also feasible. Having this technique for a rover mission that analyzes various bulk compositions of soil and rocks for geological investigation over short distances is highly desirable.

Table 6 shows the summary of oxides in Mars and Earth (*http://nssdc.gsfc.nasa.gov/planetary/marspath/apxs_table1.html*).

Figure 22 shows the comparison of elemental ratios for various rock and soil samples that were measured by the XRS on the Viking and Pathfinder missions (Rieder et al. 1997).

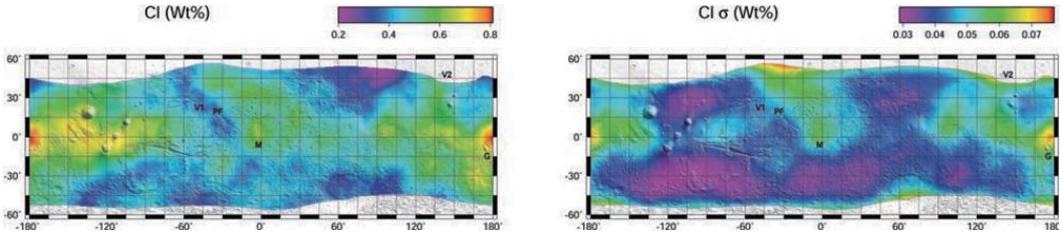

Fig. 21 Cl elemental map (*Left*) and uncertainty map (*Right*) obtained by MOGRS (Boynton et al. 2007).

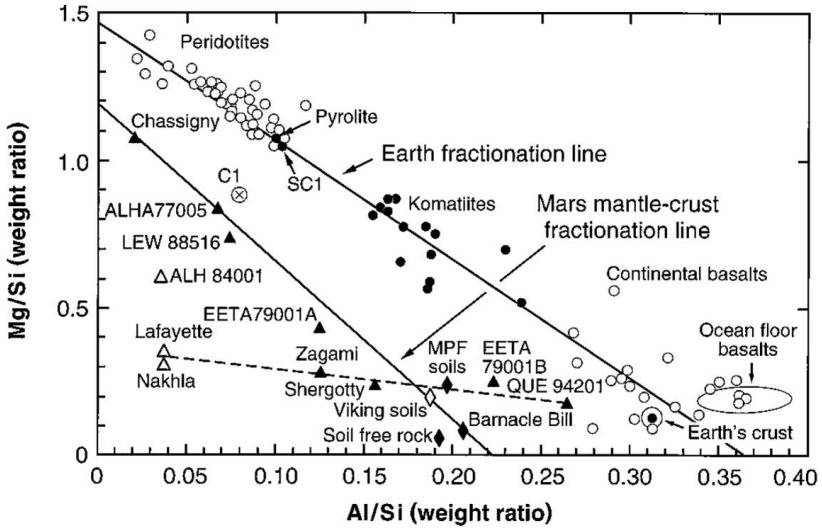

Fig. 22 Mg/Si versus Al/Si diagram of martian meteorites (*filled triangles*), mean values of Viking soils (*open diamonds*), and Pathfinder soils (labeled as MPF soils), as well as Barnacle Bill and calculated "soil-free rock" composition (*filled diamonds*) in comparison with terrestrial samples (Rieder et al. 1997).

Figure 23 shows the Mars Exploration Rover (Opportunity)'s X-ray spectra of rock materials before and after abrading with the Rock Abrasion Tool (RAT) (Gusev Crater) (Gellert et al. 2004). This figure shows both weathered and fresh rock substances, which demonstrate aspects of surface geologic history that might be apparent in the rock.

6.2.2 Water on Mars

Both GRS and neutron spectrometers mounted on Mars Odyssey have confirmed the existence of water equivalent hydrogen at the polar and mid-latitude regions (Boynton et al. 2002, 2007; Feldman et al. 2002). The highest abundance of water equivalent hydrogen obtained by MOGRS for the north and south polar regions and mid latitude was found to be over 90%, 45%, and 7%, respectively (Fig. 24) (Boynton et al. 2002, 2007). The water abundance values obtained from epithermal neutron

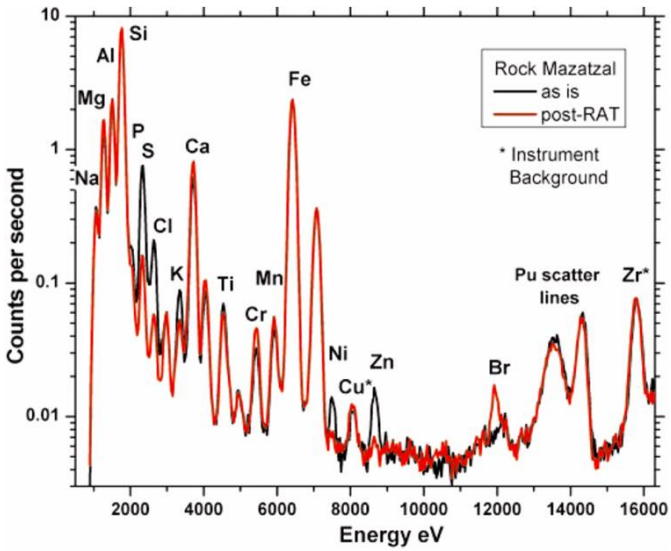

Fig. 23 X-ray spectra of rock material before and after abrading with the RAT (Gusev Crater) (Gellert et al. 2004).

Table 6 Comparison of Oxides for Mars and Earth Samples.

	Mars (weight %)			Earth (weight %)		
Oxide	A-3, Rock	A-5, Soil	SNCs	Continental Crust		Oceanic Crust
	"Barnacle Bill"		Meteorites	Average	Sediments	
MgO	3.1	8.6	9.3 – 31.6	3.1	3.1	7.7
Al_2O_3	12.4	10.1	0.7 – 12.0	15.2	13.0	15.6
SiO_2	55.0	43.8	38.2 – 52.7	60.2	50.0	50.7
K_2O*	1.4	0.7	0.022 – 0.19	2.9	2.0	0.17
CaO	4.6	5.3	0.6 – 15.8	5.5	8.4	11.4
TiO_2	0.7	0.7	0.1 – 1.8	0.7	0.7	1.5
MnO*	0.9	0.6	0.44 – 0.55	0.1	0.1	0.16
FeO	12.7	17.5	17.6 – 27.1	6.05	5.5	9.9
FeO/MnO	14.1	29.2	37.0 – 51.5			

Notes: *Data obtained from *http://nssdc.gsfc.nasa.gov/planetary/marspath/apxs_table1.html*

data are similar to those from GRS, but slightly higher (Feldman et al. 2002). The existence of water in the polar region was discovered by the visible camera from Mars Global Surveyor. The results of MOGRS data confirmed it as hydrogen which is composed of water with the hydrogen gamma-ray peak of 2.223 MeV. With the results from deposits of polar ice by MOGRS, the selection of a landing site of the Mars Polar Lander, Phoenix, was performed. From this landing site, water ice underneath of soil that covered the surface was successfully confirmed.

At present, there is evidence for the existence of water on the surface of Mars. In addition, the existence of a large body of water in the past on Mars has also been confirmed by analyzing MOGRS data for Th, K, and Fe. These elements are found to be enriched in the lowland region of the northern hemisphere where the elevation is 0 km, which is called a shore line. There have been

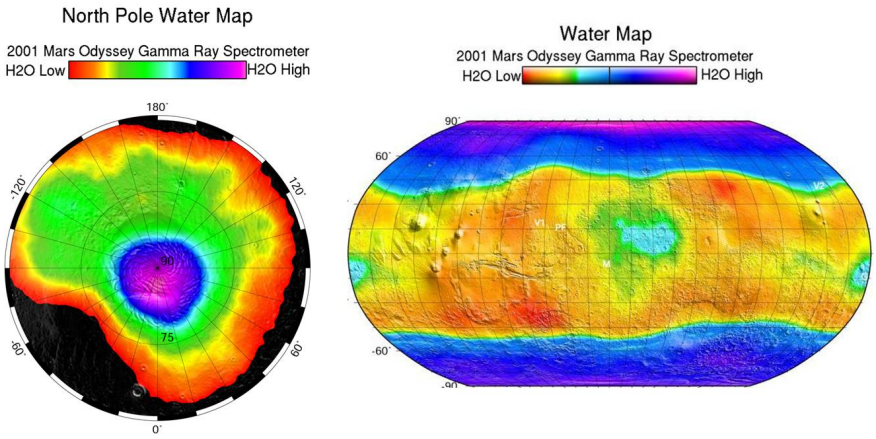

Fig. 24 Water map for Mars North Polar region and global water map obtained by Mars Odyssey GRS (Boynton et al. 2007; (*http://grs.lpl.arizona.edu/latestresults.jsp?lrid=21*).

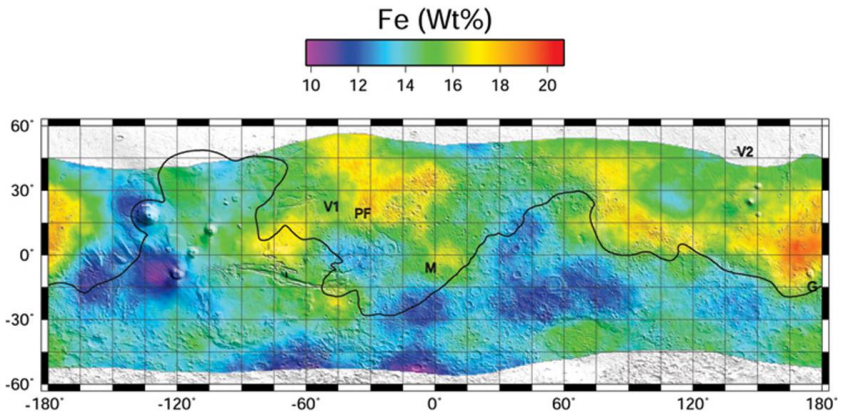

Fig. 25 Global Fe map obtained by MOGRS. Fe is enriched in the lowland area of Acidalia Planitia. Fe could have been transported from the higher terrane to the lowland regions.

three shorelines suggested on Mars. The significantly enriched Th, K, and Fe in the lowland of the northern regions confirmed the possibility of a paleo-ocean on Mars (Fig. 25) (Dohm et al. 2009). This phenomenon possibly occurred because these elements were leached by water and transported downward to lower land areas (Fig. 26). Signatures of ancient water have also been found by APXS data from the Mars Exploration Rover, for example the hydrating minerals in an area with deposits of iron and salt. Also, water equivalent hydrogen in the mid-latitude region where Meridiani Planum is located is found to be at least 7% at present (Boynton et al. 2007). Mars Exploration Rover's Opportunity landed on this region and found hematite, which is known to be formed by the presence

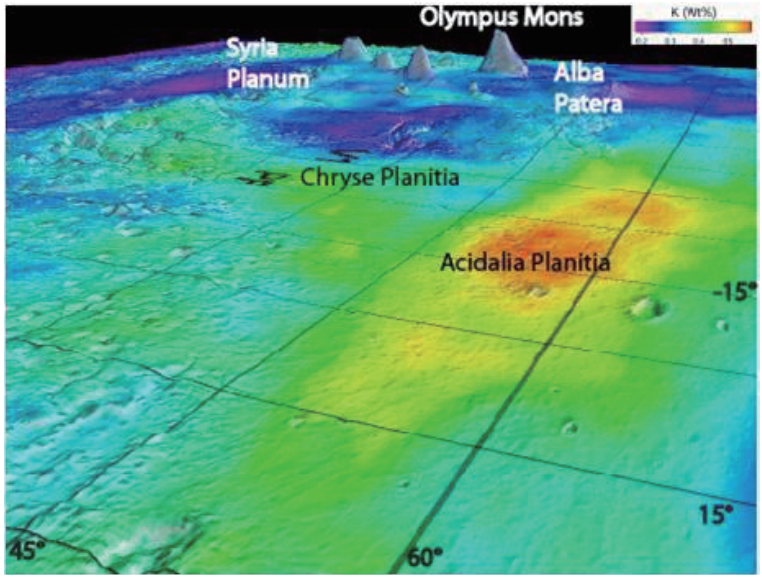

Fig. 26 K is enriched in the lowland area of Acidalia Planitia. K could have been transported from the higher terrane to the lowland regions (Dohm et al. 2009).

of water. Other remote sensing data which are related to signatures of water have been reported by Mars Express. Mars Odyssey's THEMIS has observed surface geological features related to the existence of salt. Also, in Malea Planum, it has also been observed that water vapor increases in the atmosphere during daytime, when the temperature increases.

6.2.3 Atmospheric characteristics

When the cap of CO_2 increases its size in the polar region, the observation of hydrogen gamma-ray flux decreases. Similarly, the naturally radioactive element K also decreases as the CO_2 cap increases. The determination of CO_2 depth was therefore estimated using the signals of H and K in the polar regions. Seasonal variation with CO_2 depth and these nuclides were studied and the variation of CO_2 thickness (g cm^{-2}) ranged from 0 cm to about 25 g cm^{-2}, and K- and H-gamma-ray flux variations with respect to Ls (solar longitude) compared well with the Ames GCM average (Kelly et al. 2006). It was also found that CO_2 increases the flux of thermal neutrons, which creates a related increase of neutron-capture-produced gamma-rays. Therefore, uncertainty in the distribution of H with depth leads to uncertainty in predictions of H-based CO_2 thickness (Kelly et al. 2006). Ar abundance observed by GRS was studied with respect to Ls. During Ls of about 100, the Ar enhancement at the south polar region was observed. This phenomenon arises from the fact that Ar is associated with horizontal meridional mixing in the southern winter (Sprague et al. 2004).

6.2.4 Bulk composition

The K and Th from the MOGRS data are uniformly distributed over Mars. The K and Th variations range from 2000 to 6000 and 0.2 to 1 ppm, respectively. The concentration of Th on Mars does not vary as much as on the Moon. This shows the primary process of differentiation in Mars was not the same as that of the Moon (Taylor et al. 2006b).

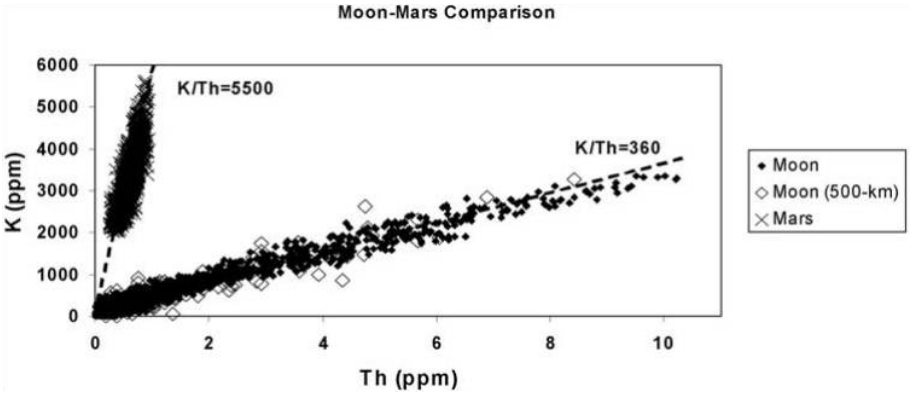

Fig. 27 Th and K abundance on Mars and the Moon (Taylor et al. 2006b).

The GRS data of K and Th provided an understanding of the crustal evolution of Mars. Based on the K/Th ratio of the MOGRS data, Mars seems to have higher K/Th than the Earth. Most terrestrial rocks have a similar, but perhaps slightly greater range of K/Th than do Martian rocks, but show a much greater range in Th and K concentrations. This shows that no extensive differentiation occurred on Mars, and probably little if any melting of the crust happened (Fig. 27) (Taylor et al. 2006a). Terrestrial arc magmas vary widely in K/Th, probably due to fluids rich in H_2O playing an important role in their formation. Although there is no evidence for this in terms of K or Th, and no related data currently exist for Mars, an aqueous process of low-temperature and hydrothermal activity may have affected K/Th on Mars. Figure 27 shows the comparison of K/Th ratios for Mars and the Moon.

6.3 Unanswered Questions

There have been over 40 years of activities related to lunar investigation in the past. With the numerous past lunar missions, the Moon has become one of the best studied planetary objects for humans. However, there are still major unanswered questions which should be solved by future investigations. Wieczorek et al. (2006) described that there are seven unanswered questions.

(1) Is there a surface distribution of KREEP in the underlying crust?
(2) What is the provenance of the magnesian-suite rocks?
(3) What is the composition and origin of the lower crust?
(4) What is the composition of the SPA basin?
(5) What is the composition and depth of the farside and young nearside basalts?
(6) What is the origin and lateral extent of the 500-km seismic discontinuity?
(7) What is the size and composition of the core, and was there ever a core dynamo? (Wieczorek et al. 2006).

Since the late 2000s, there have been several lunar missions: SELENE-1 (Kaguya), Chandrayaan-1, Chang'E-1 & 2, LCROSS, and LRO. Among these missions, the Kaguya mission especially focused on lunar science with 14 science payloads. The remote sensing data could be helpful in finding answers to questions described above by an integrated scientific outcome from the various key lunar datasets from the mission. The other most recent missions are much more focused on finding water on the Moon and preparing for a future manned mission to the Moon. However, most of these questions can be answered by obtaining samples and possibly revisiting the lunar sur-

face for physical experiments. With this goal, the International Lunar Network (ILN) program is an important program to answer some of these questions (ILN report).

The National Research Council (NRC) described eight major science concepts and outlined 35 goals to address the future of lunar science and exploration with regard to the Constellation Program (NRC 2007[1]). This study focuses on Concept 5 with respect to the SPA Basin. Concept 5 states "Lunar volcanism provides a window into the thermal and compositional evolution of the Moon" (NRC 2007). This concept is subdivided into four science goals addressing (1) the origin and variability of lunar basalts, (2) age of lunar basalts, (3) compositional range and extent of lunar pyroclastic deposits, and (4) the flux and evolution of lunar volcanism (Ennis et al. 2010).

In recent years, several investigations on a future sample return mission of SPA were reported with scientific expectations from a sample to be returned from the SPA basin (Gillis et al. 2003b; Ennis et al. 2010; Duke 2003; Jolliff et al. 2003). A new SPA sample return mission could therefore focus on studies of the farside lunar volcanism, determine the origin and variability of lunar basalts, determine the age of the youngest and oldest mare basalts, determine the compositional range and extent of lunar pyroclastic deposits, determine the flux of lunar volcanism and its evolution through space and time, and collect a sample of SPA (Ennis et al. 2010).

7 CONCLUDING REMARKS

In understanding the origin and evolution of celestial objects such as planets, the Moon and asteroids, their elemental composition is very important. Their spatial distribution in terms of concentrations of elements is an important clue for understanding planetary history. To investigate such celestial bodies, we must determine the chemical compositions of their distinctive geologic regions. The Fe and Ti contents of the lunar surface, for instance, contain clues on how the Moon formed, the extent of its initial melting, the compositions of its lava flows, the mechanisms of crater formation, and other interesting facets of lunar history. Ti is an important probe of the magma compositions, because it does not enter most minerals. Instead, it builds up in magma during crystallization, and then its abundance is a good measure of the amount of crystallization that took place before a given rock formed in magma over a large scale. The two elements allow us to distinguish among the known types of lunar rocks, and Ti forms the basis for classifying the basalts that make up the lunar maria.

Aluminum is particularly useful because the lunar crust has lots of it. The problem is that we do not have a clear idea of how much aluminum there is in the mantle of the Moon. Estimates range from 2.5 wt% to 7 wt% Al_2O_3, compared to 4.1 wt% in Earth. Magnesium is also one of the very important elements. It is particularly interesting to study how magma changes in composition as it crystallizes, because it tends to systematically decrease with crystallization. This happens because the first minerals to crystallize tend to take up more Mg than they do Fe, leading to a decrease in the ratio of Mg#.

Natural radioactive elements, like Th and U, are important because we understand their behavior during the formation and subsequent evolution of magma, and because they are refractory elements that condense from gas at a high temperature. If we know the Th- and/or U-concentrations, we can also derive the concentrations of all other refractory elements with similar geochemical behavior, which include the REEs, Zr, Ti, Ca and Al. In addition, these natural radioactive elements are useful as a tracer of crust formation when considering the thermal history of the body since they are an important heat source.

Remote observations conducted during planetary missions have provided us global information about the elemental and mineralogical compositions of planetary surfaces. Remote planetary nuclear spectroscopy, used to investigate the elemental composition and distribution on all surfaces of the body, has achieved significant progress so far. Even such fundamental concepts in planetary evolution, such as a magma ocean and the hemispheric dichotomy of both the Moon and Mars, were

[1] National Research Council 2007, The scientific context for exploration of the Moon, final report.

formulated before remotely-sensed data showed vast areas of the exposed crust. In the near future, advanced nuclear instruments will be equipped on planetary rovers and spectroscopic measurements with higher accuracy will allow a wider scope of elements than those in remote measurements. These future abilities will give us a deeper understanding of those planetary bodies.

After successfully executing missions with unmanned probes that make good use of remote sensing and robot technology, and resolving many technical problems, humans can set foot on these distant bodies. Even in the future, remote observations with high resolution and accuracy are necessary in various scales of the Moon while conducting a global investigation of detailed local properties. As more advanced instruments will be installed on surface rovers, they can better investigate a landing site in terms of rock and chemical composition, mineral composition, as well as conducting a soil and geophysical survey, which will set the stage for a manned survey of the Moon's surface in the future.

Advanced technology required for the lunar probe, which extends to various fields, leads to the development of advanced technologies in energy, materials, information etc. Explorations of the Moon and other planets are vital to the future hopes and dreams of younger generations, leading to future human activities to support science and technology.

Acknowledgements Our great gratitude goes to Wing-Huen Ip at National Central University and M.H. Zhu at the Macau University of Science and Technology for preliminary GRS results by Chang'E-2. This paper is partially supported by the Korea-Japan International Cooperative Research Program funded by the Korean Research Fund (F01-2009-000-100540-0, 10-6303) and KIGAM's Internal Project (12-3612) funded by the Ministry of Knowledge Economy.

References

Adler, I., & Trombka, J. I. 1977, Physics and Chemistry of Earth, 10, 17

Adler, I., & Trombka, J. I. 1980, Chemistry of the Moon: Physics and Chemistry of the Earth, 10 (Pergamon Press), 173

Adler, I., Trombka, J. I., Schmadebeck, R., et al. 1973, in Lunar and Planetary Science Conference Proceedings, 4, 2783

Akkurt, H., Groves, J. L., Trombka, J., et al. 2005, Nuclear Instruments and Methods in Physics Research B, 241, 232

Andre, C. G., Adler, I., Bielefeld, M. J., et al. 1977, Science, 197, 986

Andresen, R. D., Karlsson, L., & Taylor, B. G. 1976, IEEE Transactions on Nuclear Science, 23, 473

Aoshima, C., & Namiki, N. 2001, in Lunar and Planetary Institute Science Conference Abstracts, 32, 1561

Araki, H., Tazawa, S., Noda, H., et al. 2009, Science, 323, 897

Bandfield, J. L., Hamilton, V. E., & Christensen, P. R. 2000, Science, 287, 1626

Beckhoff, B., Kanngießer, B., Langhoff, N., Wedell, R., & Wolff, H. 2006, Handbook of Practical X-Ray Fluorescence Analysis, eds. B. Beckhoff, B. Kanngießer, N. Langhoff, R. Wedell, & H. Wolff. (Berlin: Springer)

Bernstein, L. A., Archer, D. E., Becker, J. A., et al. 2001, Nuclear Physics A, 682, 404

Bessiere, A., Dorenbos, P., van Eijk, C. W. E., Kramer, K. W., & Gudel, H. U. 2005, Nuclear Instruments and Methods in Physics Research A, 537, 242

Bielefeld, M. J., Reedy, R. C., Metzger, A. E., Trombka, J. I., & Arnold, J. R. 1976, in Lunar and Planetary Science Conference Proceedings, 7, ed. D. C. Kinsler, 2661

Binder, A. B. 1998, Science, 281, 1475

Bonard, J.-M., Stöckli, T., Noury, O., & Châtelain, A. 2001, Applied Physics Letters, 78, 2775

Boynton, W. V., Feldman, W. C., Squyres, S. W., et al. 2002, Science, 297, 81

Boynton, W. V., Feldman, W. C., Mitrofanov, I. G., et al. 2004, Space Sci. Rev., 110, 37

Boynton, W. V., Taylor, G. J., Evans, L. G., et al. 2007, Journal of Geophysical Research (Planets), 112, E12S99
Brownridge, J. D., & Raboy, S. 1999, Journal of Applied Physics, 86, 640
Brueckner, J., Koerfer, M., Waenke, H., et al. 1991, IEEE Transactions on Nuclear Science, 38, 209
Canali, C., Gatti, E., Kozlov, S. F., et al. 1979, Nuclear Instruments and Methods, 160, 73
Castagnoli, G., & Lal, D. 1980, Radiocarbon, 22, 133
Castaneda, C. M., Gearhart, D. G., Gearhart, R. M., et al. 2007, Nuclear Instruments and Methods in Physics Research B, 260, 508
Chang, J., Ma, T., Zhang, N., et al. 2009, Journal of the Physical Society of Japan, 78, 26
Chenet, H., Lognonné, P., Wieczorek, M., & Mizutani, H. 2006, Earth and Planetary Science Letters, 243, 1
Cheng, A. F., Farquhar, R. W., & Santo, A. G. 1998, Johns Hopkins APL Technical Digest, 19, 95
Chin, G., Brylow, S., Foote, M., et al. 2007, Space Sci. Rev., 129, 391
Chou, C.-L., Boynton, W. V., Sundberg, L. L., & Wasson, J. T. 1975, in Lunar and Planetary Science Conference Proceedings, 6, 1701
Christiansen, E. H. 1989, Geology, 17, 203
Clark, P. E., & Adler, I. 1978, in Lunar and Planetary Science Conference Proceedings, 9, 3029
Clark, P. E., & Hawke, B. R. 1982, in Lunar and Planetary Science Conference Proceedings, 12, eds. R. B. Merrill, & R. Ridings, 727
Colaprete, A., Schultz, P., Heldmann, J., et al. 2010, Science, 330, 463
Crawford, R. K. 1993, in Society of Photo-Optical Instrumentation Engineers (SPIE) Conference Series, 1737, eds. J. M. Carpenter, D. B. Cline, R. Lanza, & D. F. R. Mildner, 210
Cushing, J. A., Taylor, G. J., Norman, M. D., & Keil, K. 1999, Meteoritics and Planetary Science, 34, 185
Dasch, E. J., Shih, C.-Y., Bansal, B. M., Wiesmann, H., & Nyquist, L. E. 1987, Geochim. Cosmochim. Acta, 51, 3241
Dehon, R. A., & Waskom, J. D. 1976, in Lunar and Planetary Science Conference Proceedings, 7, ed. D. C. Kinsler, 2729
Del Sordo, S., Abbene, L., Caroli, E., et al. 2009, Sensors, 9, 3491
Delano, J. W. 1986, J. Geophys. Res., 91, 201
Delano, J. W., & Livi, K. 1981, Geochim. Cosmochim. Acta, 45, 2137
Dohm, J. M., Baker, V. R., Boynton, W. V., et al. 2009, Planet. Space Sci., 57, 664
Duke, M. B. 2003, in Lunar and Planetary Institute Science Conference Abstracts, 34, eds. S. Mackwell, & E. Stansbery, 1684
D'Uston, C., Thocaven, J. J., Hasebe, N., et al. 2005, in 36th Annual Lunar and Planetary Science Conference, 36, eds. S. Mackwell, & E. Stansbery, 1873
Elphic, R. C., Lawrence, D. J., Feldman, W. C., et al. 1998, Science, 281, 1493
Elphic, R. C., Lawrence, D. J., Feldman, W. C., et al. 2000, J. Geophys. Res., 105, 20333
Elphic, R. C., Lawrence, D. J., Feldman, W. C., et al. 2002, Journal of Geophysical Research (Planets), 107, 5024
Ennis, M. E., Fagan, A. L., Pogue, J. N., et al. 2010, in Lunar and Planetary Institute Science Conference Abstracts, 41, 2512
Evans, L. G., Reedy, R. C., & Trombka, J. I. 1993, Introduction to planetary remote sensing gamma-ray spectroscopy, in Remote Geochemical Analysis: Elemental and Mineralogical Composition, eds. C. M. Pieters, & P. A. J. Englert (Cambridge Univ. Press), 167
Evans, L. G., Boynton, W. V., Reedy, R. C., Starr, R. D., & Trombka, J. I. 2002, in Proceedings of SPIE, 4784, 31
Evans, L. G., Reedy, R. C., Starr, R. D., Kerry, K. E., & Boynton, W. V. 2006, Journal of Geophysical Research (Planets), 111, E03S04

Feldman, W. C., Boynton, W. V., & Drake, D. M. 1993, Planetary neutron spectroscopy from orbit, in Remote Geochemical Analysis: Elemental and Mineralogical Composition, eds. C. M. Pieters, & P. A. J. Englert (Cambridge Univ. Press), 213
Feldman, W. C., Maurice, S., Binder, A. B., et al. 1998, Science, 281, 1496
Feldman, W. C., Barraclough, B. L., Fuller, K. R., et al. 1999, Nuclear Instruments and Methods in Physics Research A, 422, 562
Feldman, W. C., Lawrence, D. J., Elphic, R. C., et al. 2000, J. Geophys. Res., 105, 4175
Feldman, W. C., Maurice, S., Lawrence, D. J., et al. 2001, J. Geophys. Res., 106, 23231
Feldman, W. C., Boynton, W. V., Tokar, R. L., et al. 2002, Science, 297, 75
Feldman, W. C., Ahola, K., Barraclough, B. L., et al. 2004, Journal of Geophysical Research (Planets), 109, E07S06
Ferrando, P., Goldwurm, A., Laurent, P., et al. 2005, in Society of Photo-Optical Instrumentation Engineers (SPIE) Conference Series, 5900, eds. O. Citterio, & S. L. O'Dell, 195
Fischer, E. M., & Pieters, C. M. 1995, J. Geophys. Res., 100, 23279
Fogel, R. A., & Rutherford, M. J. 1995, Geochim. Cosmochim. Acta, 59, 201
Gasnault, O., d'Uston, C., Feldman, W. C., & Maurice, S. 2000, J. Geophys. Res., 105, 4263
Gasnault, O., Feldman, W. C., Maurice, S., et al. 2001, Geophys. Res. Lett., 28, 3797
Gehrels, N., Chincarini, G., Giommi, P., et al. 2004, ApJ, 611, 1005
Gellert, R., Rieder, R., Anderson, R. C., et al. 2004, Science, 305, 829
Gellert, R., Rieder, R., Brückner, J., et al. 2006, Journal of Geophysical Research (Planets), 111, E02S05
Gellert, R., Campbell, J. L., King, P. L., et al. 2009, in Lunar and Planetary Institute Science Conference Abstracts, 40, 2364
Geuther, J. A., & Danon, Y. 2005, Journal of Applied Physics, 97, 104916
Gibson, E. K., Jr. 1977, Physics and Chemistry of Earth, 10, 57
Gillis, J. J., Jolliff, B. L., & Elphic, R. C. 2003a, Journal of Geophysical Research (Planets), 108, 5009
Gillis, J. J., Jolliff, B. L., & Lucey, P. G. 2003b, in Lunar and Planetary Institute Science Conference Abstracts, 34, eds. S. Mackwell, & E. Stansbery, 2065
Gillis, J. J., Jolliff, B. L., & Korotev, R. L. 2004, Geochim. Cosmochim. Acta, 68, 3791
Gladstone, G. R., Hurley, D. M., Retherford, K. D., et al. 2010, Science, 330, 472
Goldsten, J. O., McNutt, R. L., Jr., Gold, R. E., et al. 1997, Space Sci. Rev., 82, 169
Goldsten, J. O., Rhodes, E. A., Boynton, W. V., et al. 2007, Space Sci. Rev., 131, 339
Goswami, J. N., & Annadurai, M. 2008, Acta Astronautica, 63, 1215
Grande, M. 1997, Advances in Space Research, 19, 1609
Grande, M., Browning, R., Waltham, N., et al. 2003, Planet. Space Sci., 51, 427
Grande, M., Kellett, B. J., Howe, C., et al. 2007, Planet. Space Sci., 55, 494
Grande, M., Maddison, B. J., Howe, C. J., et al. 2009, Planet. Space Sci., 57, 717
Grard, R., & Balogh, A. 2001, Planet. Space Sci., 49, 1395
Haga, A., Senda, S., Sakai, Y., et al. 2004, Applied Physics Letters, 84, 2208
Haines, E. L., Etchegaray-Ramirez, M. I., & Metzger, A. E. 1978, in Lunar and Planetary Science Conference Proceedings, 9, 2985
Haines, E. L., & Metzger, A. E. 1980, in Lunar and Planetary Science Conference Proceedings, 11, ed. S. A. Bedini, 689
Harrington, T. M., Marshall, J. H., Arnold, J. R., et al. 1974, Nuclear Instruments and Methods, 118, 401
Harvey, J. A., & Hill, N. W. 1979, Nuclear Instruments and Methods, 162, 507
Hasebe, N., Shibamura, E., Miyachi, T., et al. 2008, Earth, Planets, and Space, 60, 299
Hasebe, N., Shibamura, E., Miyachi, T., et al. 2009, Journal of the Physical Society of Japan Supplement, 78, 18

Hasebe, N. et al. 2010, New Advances in Lunar Exploration (Proc. of International Symposium on Lunar Science ISLS2010, March 25-26, Macau, 84
Haskin, L., & Warren, P. 1991, Lunar Chemistry, in Lunar Sourcebook: A User's Guide to the Moon, eds. G. Heiken, D. Vaniman, & B. M. French (Cambridge Univ. Press), 357
Haskin, L. A. 1998, J. Geophys. Res., 103, 1679
Haskin, L. A., Gillis, J. J., Korotev, R. L., & Jolliff, B. L. 2000a, in Lunar and Planetary Institute Science Conference Abstracts, 31, 1661
Haskin, L. A., Gillis, J. J., Korotev, R. L., & Jolliff, B. L. 2000b, J. Geophys. Res., 105, 20403
Hayatsu, K., Hareyama, M., Kobayashi, S., et al. 2008, Biological Sciences in Space, 22, 59
Hayne, P. O., Greenhagen, B. T., Foote, M. C., et al. 2010, Science, 330, 477
Head, J. W., III 1976, Reviews of Geophysics and Space Physics, 14, 265
Head, J. W., III, & Wilson, L. 1992, Geochim. Cosmochim. Acta, 56, 2155
Heiken, G. H., Vaniman, D. T., & French, B. M. 1991, Lunar Sourcebook - A User's Guide to the Moon (Cambridge Univ. Press), 753
Hiesinger, H., Jaumann, R., Neukam, G., & Head, J. W. 2000, J. Geophys. Res., 105, 29239
Hiesinger, H., Head, J. W., Wolf, U., Jaumann, R., & Neukum, G. 2003, Journal of Geophysical Research (Planets), 108, 5065
Hiesinger, H., & Head, III, J. W. 2006, Reviews in Mineralogy and Geochemistry, 60, 1
Hikida, H., & Wieczorek, M. A. 2007, Icarus, 192, 150
Ishihara, Y., Goossens, S., Matsumoto, K., et al. 2009, Geophys. Res. Lett., 36, L19202
Jansson, P. A. 1997, Deconvolution of images and spectra., 1997, XIV + 514 p., ISBN 0-12-380222-9 (San Diego, CA (USA): Academic Press)
Jolliff, B. L., Rockow, K. M., Korotev, R. L., & Haskin, L. A. 1996, Meteoritics and Planetary Science, 31, 116
Jolliff, B. L., Korotev, R. L., & Rockow, K. M. 1998, Meteoritics and Planetary Science, 33, 581
Jolliff, B. L., Gillis, J. J., Haskin, L. A., Korotev, R. L., & Wieczorek, M. A. 2000, J. Geophys. Res., 105, 4197
Jolliff, B. L., Haskin, L. A., Korotev, R. L., et al. 2003, in Lunar and Planetary Institute Science Conference Abstracts, 34, eds. S. Mackwell, & E. Stansbery, 1989
Jolliff, B. L., & Gillis, J. J. 2005, Meteoritics and Planetary Science Supplement, 40, 5330
Kamata, Y., Takeshima, T., Okada, T., & Terada, K. 1999, Advances in Space Research, 23, 1829
Kato, M., Sasaki, S., Tanaka, K., Iijima, Y., & Takizawa, Y. 2008, Advances in Space Research, 42, 294
Kelly, N. J., Boynton, W. V., Kerry, K., et al. 2006, Journal of Geophysical Research (Planets), 111, E03S07
Khan, A., Maclennan, J., Taylor, S. R., et al. 2006, Journal of Geophysical Research, 111, JE002608
Khan, A., & Mosegaard, K. 2002, Journal of Geophysical Research (Planets), 107, 5036
Khan, A., Mosegaard, K., & Rasmussen, K. L. 2000, Geophys. Res. Lett., 27, 1591
Kim, K. J., Reedy, R. C., & Gasnault, O. 2005, in 36th Annual Lunar and Planetary Science Conference, 36, eds. S. Mackwell, & E. Stansbery, 1900
Kim, K. J., Drake, D. M., Reedy, R. C., Williams, R. M. S., & Boynton, W. V. 2006, Journal of Geophysical Research (Planets), 111, E03S09
Kim, K. J., Reedy, R. C., Drake, D. M., & Hasebe, N. 2010, in Lunar and Planetary Institute Science Conference Abstracts, 41, 2420
Knitel, M. J., Dorenbos, P., de Haas, J. T. M., & van Eijk, C. W. E. 1996, Nuclear Instruments and Methods in Physics Research A, 374, 197
Knoll, G. F. 2000, Radiation Detection and Measurement, 3rd ed. (New York: Wiley), 802
Kobayashi, S., Hasebe, N., Shibamura, E., et al. 2010, Space Sci. Rev., 154, 193
Kobayashi, S., Karouji, Y. Morota, T., et al. 2012, Earth and Planetary Science Letters, 337, 10
Korotev, R. L. 1987, J. Geophys. Res., 92, 411
Korotev, R. L. 1996, Meteoritics and Planetary Science, 31, 403

Korotev, R. L. 1997, Meteoritics and Planetary Science, 32, 447
Korotev, R. L. 1998, J. Geophys. Res., 103, 1691
Korotev, R. L. 2000, J. Geophys. Res., 105, 4317
Korotev, R. L., & Gillis, J. J. 2001, J. Geophys. Res., 106, 12339
Korotev, R. L., Jolliff, B. L., Zeigler, R. A., Gillis, J. J., & Haskin, L. A. 2003, Geochim. Cosmochim. Acta, 67, 4895
Korotev, R. L., & Kremser, D. T. 1992, in Lunar and Planetary Science Conference Proceedings, 22, eds. G. Ryder, & V. L. Sharpton, 275
Kuskov, O. L., & Kronrod, V. A. 1998, Physics of the Earth and Planetary Interiors, 107, 285
Langseth, M. G., Keihm, S. J., & Peters, K. 1976, in Lunar and Planetary Science Conference Proceedings, 7, ed. D. C. Kinsler, 3143
Lawrence, D. J., Feldman, W. C., Barraclough, B. L., et al. 1998, Science, 281, 1484
Lawrence, D. J., Feldman, W. C., Barraclough, B. L., et al. 1999, Geophys. Res. Lett., 26, 2681
Lawrence, D. J., Feldman, W. C., Barraclough, B. L., et al. 2000, J. Geophys. Res., 105, 20307
Lawrence, D. J., Elphic, R. C., Feldman, W. C., et al. 2003, Journal of Geophysical Research (Planets), 108, 5102
Lawrence, D. J., Puetter, R. C., Elphic, R. C., et al. 2007, Geophys. Res. Lett., 34, L03201
Lechner, P., Fiorini, C., Hartmann, R., et al. 2001, Nuclear Instruments and Methods in Physics Research A, 458, 281
Lechner, P., Fiorini, C., Longoni, A., et al. 2004, Advances in X-ray Analysis, 47, 53
Lingenfelter, R. E., Canfield, E. H., & Hess, W. N. 1961, J. Geophys. Res., 66, 2665
Lognonné, P. 2005, Annual Review of Earth and Planetary Sciences, 33, 571
Longoni, A., Fiorini, C., Guazzoni, C., et al. 2006, IEEE Transactions on Nuclear Science, 53, 641
Lucey, P. G. 1998, J. Geophys. Res., 103, 1703
Lucey, P., Korotev, R. L., Gillis, J. J., et al. 2006, Reviews in Mineralogy and Geochemistry, 60, 83
Maruyama, Y., Ogawa, K., Okada, T., & Kato, M. 2008, Earth, Planets, and Space, 60, 293
Masarik, J., & Reedy, R. C. 1994, Geochim. Cosmochim. Acta, 58, 5307
Maurice, S., Lawrence, D. J., Feldman, W. C., Elphic, R. C., & Gasnault, O. 2004, Journal of Geophysical Research (Planets), 109, E07S04
McGregor, D. S., & Hermon, H. 1997, Nuclear Instruments and Methods in Physics Research A, 395, 101
McKay, D. S., Heiken, G. H., Basu, A., et al. 1991, The Lunar Regolith, in Lunar Sourcebook: A User's Guide to the Moon, eds. G. Heiken, D. Vaniman, & B. M. French (Cambridge Univ. Press), 285
McKinney, G. W., Lawrence, D. J., Prettyman, T. H., et al. 2006, Journal of Geophysical Research (Planets), 111, E06004
Metzger, A. E., Trombka, J. I., Peterson, L. E., Reedy, R. C., & Arnold, J. R. 1973, Science, 179, 800
Metzger, A. E., Haines, E. L., Parker, R. E., & Radocinski, R. G. 1977, in Lunar and Planetary Science Conference Proceedings, 8, ed. R. B. Merril, 949
Metzger, A. E., & Parker, R. E. 1979, Earth and Planetary Science Letters, 45, 155
Metzger, A. E. 1993, Composition of the Moon as Determined from Orbit by Gamma-ray Spectroscopy, in Remote Geochemical Analysis: Elemental and Mineralogical Composition, eds. C. P. Pieters, & P. A. J. Englert (Cambridge Univ. Press), 341
Mewaldt, R. A. 2006, Space Sci. Rev., 124, 303
Mitrofanov, I., Anfimov, D., Kozyrev, A., et al. 2002, Science, 297, 78
Mitrofanov, I. G., Sanin, A. B., Kozyrev, A. S., et al. 2005, in 36th Annual Lunar and Planetary Science Conference, 36, eds. S. Mackwell, & E. Stansbery, 1879
Mitrofanov, I. G., Sagdeev, R. Z., Boynton, W. V., et al. 2006, AGU Fall Meeting Abstracts, D1234

Mitrofanov, I. G., Litvak, M. L., Kozyrev, A. S., Sanin, A. B., & Tretyakov, V. I. 2009, in Lunar and Planetary Institute Science Conference Abstracts, 40, 1207
Mitrofanov, I. G., Sanin, A. B., Boynton, W. V., et al. 2010, Science, 330, 483
Morris, R. V. 1980, in Lunar and Planetary Science Conference Proceedings, 11, ed. S. A. Bedini, 1697
Morrison, D. A. 1998, in Lunar and Planetary Institute Science Conference Abstracts, 29, 1657
Nakamura, Y., Latham, G. V., Dorman, H. J., et al. 1979, in Lunar and Planetary Science Conference Proceedings, 10, ed. N. W. Hinners, 2299
Nakamura, Y., & Koyama, J. 1982, J. Geophys. Res., 87, 4855
Namiki, N., Iwata, T., Matsumoto, K., et al. 2009, Science, 323, 900
Nava, F., Canali, C., Artuso, M., et al. 1979, IEEE Transactions on Nuclear Science, 26, 308
Neal, C. R. 2001, J. Geophys. Res., 106, 27865
Neal, C. R., Taylor, L. A., & Lindstrom, M. M. 1988, in Lunar and Planetary Science Conference Proceedings, 18, ed. G. Ryder, 139
Neal, C. R., Taylor, L. A., & Patchen, A. D. 1989a, in Lunar and Planetary Science Conference Proceedings, 19, eds. G. Ryder, & V. L. Sharpton, 137
Neal, C. R., Taylor, L. A., Schmitt, R. A., Hughes, S. S., & Lindstrom, M. M. 1989b, in Lunar and Planetary Science Conference Proceedings, 19, eds. G. Ryder, & V. L. Sharpton, 147
Nelson, R. O., Laymon, C. M., & Wender, S. A. 1991, Nuclear Instruments and Methods in Physics Research B, 56, 451
Neumann, G. A., Zuber, M. T., Smith, D. E., & Lemoine, F. G. 1996, J. Geophys. Res., 101, 16841
Nittler, L. R., Starr, R. D., Weider, S. Z., et al. 2011, Science, 333, 1847
Norman, M. D., Borg, L. E., Nyquist, L. E., & Bogard, D. D. 2003, Meteoritics and Planetary Science, 38, 645
Nyquist, L. E., & Shih, C.-Y. 1992, Geochim. Cosmochim. Acta, 56, 2213
Nyquist, L. E., Bogard, D. D., & Shih, C.-Y. 2002, Radiometric chronology of the Moon and Mars, eds. J. A. Bleeker, J. Geiss, & M. C. E. Huber (Kluwer Academic Publishers), 1325
Ohtake, M., Matsunaga, T., Haruyama, J., et al. 2009, Nature, 461, 236
Okada, T. 2004, in Lunar and Planetary Institute Science Conference Abstracts, 35, eds. S. Mackwell & E. Stansbery, 1927
Okada, T., Kato, M., Fujimura, A., Tsunemi, H., & Kitamoto, S. 1999, Advances in Space Research, 23, 1833
Okada, T., Kato, M., Fujimura, A., Tsunemi, H., & Kitamoto, S. 2000, Advances in Space Research, 25, 345
Okada, T., Shirai, K., Yamamoto, Y., et al. 2006, Science, 312, 1338
Okada, T., et al. 2009, 26$^{\mathrm{th}}$ Inter. Symp. Tech. Space Sci. (Special Issue 7), (*http://archive.ists.or.jp/ upload_pdf/2009-k-39.pdf*)
Ota, S., Kobayashi, S., Sihver, L., Yamashita, N., & Hasebe, N. 2011, Earth, Planets, and Space, 63, 25
Owens, A., Beckhoff, B., Fraser, G., et al. 2008, Analytical Chemistry, 80, 8398
Owens, A., & Peacock, A. 2004, Nuclear Instruments and Methods in Physics Research A, 531, 18
Paige, D. A., Siegler, M. A., Zhang, J. A., et al. 2010, Science, 330, 479
Papike, J. J., Ryder, G., & Shearer, C. K. 1998, Reviews in Mineralogy and Geochemistry, 36, 5.1
Parsons, A., Bodnarik, J., Evans, L., et al. 2011, Nuclear Instruments and Methods in Physics Research Section A: Accelerators, Spectrometers, Detectors and Associated Equipment, 652, 674
Peplowski, P. N., Hamara, D. K., Evans, L. G., et al. 2011a, Potassium and Thorium on the Surface of Mercury: Early Results from the MESSENGER Gamma-Ray Spectrometer, EPSC-DPS2011-1170
Peplowski, P. N., Evans, L. G., Hauck, S. A., et al. 2011b, Science, 333, 1850
Philps, B. 2006, 15th International Workshop on Room-Temperature Semiconductor X- and Gamma-Ray Detectors IEEE Nucl. Sci. Symp.Conf. Rec., 2006, 6 3585
Pieters, C. M., & Englert, P. A. J. 1993, Remote Geochemical Analysis, Elemental and Mineralogical Composition

Pieters, C. M., Tompkins, S., Head, J. W., & Hess, P. C. 1997, Geophys. Res. Lett., 24, 1903
Pieters, C. M., Gaddis, L., Jolliff, B., & Duke, M. 2001, J. Geophys. Res., 106, 28001
Pina, R. K., & Puetter, R. C. 1993, PASP, 105, 630
Pirard, B., Cabrera, J., D'Uston, C., et al. 2007, Nuclear Instruments and Methods in Physics Research A, 572, 698
Policarpo, A. J. P. L., Alves, M. A. F., Dos Santos, M. C. M., & Carvalho, M. J. T. 1972, Nuclear Instruments and Methods, 102, 337
Prettyman, T. H., Feldman, W. C., Lawrence, D. J., et al. 2002a, in Lunar and Planetary Institute Science Conference Abstracts, vol. 33, 2012
Prettyman, T. H., Lawrence, D. J., Vaniman, D. T., Elphic, R. C., & Feldman, W. C. 2002b, in The Moon Beyond 2002: Next Steps in Lunar Science and Exploration, 49
Prettyman, T. H., Feldman, W. C., Ameduri, F. P., et al. 2003, IEEE Transactions on Nuclear Science, 50, 1190
Prettyman, T. H., Hagerty, J. J., Elphic, R. C., et al. 2006a, Journal of Geophysical Research (Planets), 111, E12007
Prettyman, T. H., Barraclough, B. L., Feldman, W. C., et al. 2006b, in 37th Annual Lunar and Planetary Science Conference, eds. S. Mackwell, & E. Stansbery, 2231
Puetter, R. C., Gosnell, T. R., & Yahil, A. 2005, ARA&A, 43, 139
Quarati, F., Brandenburg, S., Buis, E.-J., et al. 2009, Nuclear Instruments and Methods in Physics Research A, 610, 354
Reames, D. V. 1998, Space Sci. Rev., 85, 327
Reedy, R. C., Arnold, J. R., & Trombka, J. I. 1973, J. Geophys. Res., 78, 5847
Reedy, R. C. 1978, in Lunar and Planetary Science Conference Proceedings, 9, 2961
Reedy, R. C., Arnold, J. R., & Lal, D. 1983, Science, 219, 127
Reedy, R. C. 2011, in Lunar and Planetary Institute Science Conference Abstracts, 42, 2405
Rieder, R., Economou, T., Wanke, H., et al. 1997, Science, 278, 1771
Rosenblum, B., Bräunlich, P., & Carrico, J. P. 1974, Applied Physics Letters, 25, 17
Ryder, G., & Wood, J. A. 1977, in Lunar and Planetary Institute Science Conference Abstracts, 8, 826
Ryder, G., & Spudis, P. 1980, in Lunar Highlands Crust, eds. R. B. Merrill & J. J. Papike, 353
Ryder, G., Norman, M. D., & Taylor, G. J. 1997, Geochim. Cosmochim. Acta, 61, 1083
Saunders, R. S., Arvidson, R. E., Badhwar, G. D., et al. 2004, Space Sci. Rev., 110, 1
Schrunk, D. G., Sharpe, B. L., Cooper, B. L., & Thangavelu, M. 2008, The Moon: Resources, Future Development, and Settlement: Second Edition (Springer-Praxis, Second Edition)
Schultz, P. H. 1997, Proc. Lunar Planet. Sci. 28, #1787 (*http://www.lpi.usra.edu/meetings/lpsc97/pdf/1787.PDF*)
Schultz, P. H., Hermalyn, B., Colaprete, A., et al. 2010, Science, 330, 468
Shikaze, Y., Haino, S., Abe, K., et al. 2007, Astroparticle Physics, 28, 154
Simpson, J. A. 1983, Annual Review of Nuclear and Particle Science, 33, 323
Snyder, G. A., & Taylor, L. A. 1993, Proceedings of the NIPR Symposium, Antarctic Meteorite Research, 6, 246
Solomon, S. C., McNutt, R. L., Gold, R. E., et al. 2001, Planet. Space Sci., 49, 1445
Spohn, T., Konrad, W., Breuer, D., & Ziethe, R. 2001, Icarus, 149, 54
Sprague, A. L., Boynton, W. V., Kerry, K. E., et al. 2004, Science, 306, 1364
Spudis, P., & Pieters, C. 1991, Global and Regional Data about the Moon in Lunar Sourcebook: A User's Guide to the Moon, eds. G. Heiken, D. Vaniman, & B. M. French (Cambridge Univ. Press), 595
Spudis, P. D., Ryder, G., Taylor, G. J., Keil, K., & McCormick, K. A. 1991, in Lunar and Planetary Science Conference Proceedings, 21, eds. G. Ryder, & V. L. Sharpton, 151
Spudis, P. D., & Taylor, G. J. 1992, in 2nd Lunar Bases and Space Activities of the 21st Century, eds. W. W. Mendell, J. W. Alred, L. S. Bell, et al., 307 (*http://www.nss.org/settlement/moon/library/LB2-0-*

ContentsAndPrologue.pdf)
Spudis, P. D., Reisse, R. A., & Gillis, J. J. 1994, Science, 266, 1848
Sugie, H., Tanemura, M., Filip, V., et al. 2001, Applied Physics Letters, 78, 2578
Surkov, I. A. 1977, in Lunar and Planetary Science Conference Proceedings, 8, ed. R. B. Merril, 2665
Surkov, I. A. 1981, Advances in Space Research, 1, 21
Takeda, H., Yamaguchi, A., Bogard, D. D., et al. 2006, Earth and Planetary Science Letters, 247, 171
Taylor, S. R., & Jakes, P. 1974, in Lunar and Planetary Science Conference Proceedings, 5, 1287
Taylor, S. R. 1975, Lunar Science - a Post-Apollo View, Scientific Results and Insights from the Lunar Samples (New York: Pergamon Press)
Taylor, S. R. 1982, Planetary science: A lunar perspective, Research supported by NASA. Houston, TX, Lunar and Planetary Institute, 1982, 502
Taylor, S. R. 1992, Solar System Evolution: A New Perspective (Cambridge Univ. Press)
Taylor, L. A., Shervais, J. W., Hunter, R. H., & Laul, J. C. 1983, in Lunar and Planetary Institute Science Conference Abstracts, 14, 777
Taylor, G. J., Warren, P., Ryder, G., et al. 1991, Lunar rocks, in Lunar Sourcebook: A User's Guide to the Moon, eds. G. Heiken, D. Vaniman, & B. M. French (Cambridge Univ. Press), 183
Taylor, L. A., Chambers, J. G., Patchen, A., et al. 1993, in Lunar and Planetary Institute Science Conference Abstracts, 24, 1409
Taylor, G. J., Boynton, W., Brückner, J., et al. 2006a, J. Geophys. Res, 111, E03S10 [printed 112(E3), 2007]
Taylor, G. J., Stopar, J. D., Boynton, W. V., et al. 2006b, Journal of Geophysical Research (Planets), 111, E03S06
Toksöz, M. N., Press, F., Dainty, A., et al. 1972, in Lunar and Planetary Science Conference Proceedings, 3, eds. A. E. Metzger, J. I. Trombka, L. E. Peterson, R. C. Reedy, & J. R. Arnold, 2527
Toksöz, M. N., Dainty, A. M., Solomon, S. C., & Anderson, K. R. 1974, Reviews of Geophysics and Space Physics, 12, 539
Tompkins, S., & Pieters, C. M. 1999, Meteoritics and Planetary Science, 34, 25
Toney, J. E., Schlesinger, T. E., & James, R. B. 1999, Nuclear Instruments and Methods in Physics Research A, 428, 14
Toulmin, P., III, Rose, H. J., Jr., Clark, B. C., Baird, A. K., & Keil, K. 1976, Science, 194, 81
Trombka, J. I., & Schmadebeck, R. L. 1968, NASA Special Publication, 3044
Trombka, J. I., Arnold, J. R., Reedy, R. C., Peterson, L. E., & Metzger, A. E. 1973, in Lunar and Planetary Science Conference Proceedings, 4, 2847
Trombka, J. I., Squyres, S. W., Brückner, J., et al. 2000, Science, 289, 2101
Ubertini, P., Lebrun, F., Di Cocco, G., et al. 2003, A&A, 411, L131
van Eijk, C. W. E., Bessière, A., & Dorenbos, P. 2004, Nuclear Instruments and Methods in Physics Research A, 529, 260
van Loef, E. V. D., Dorenbos, P., van Eijk, C. W. E., Krämer, K., & Güdel, H. U. 2001, Applied Physics Letters, 79, 1573
Vinogradov, A. P., Surkov, Y. A., Chernov, G. M., Kirnozov, F. F., & Nazarkina, G. B. 1966, Cosmic Research, 4, 751
Warren, P. H., & Wasson, J. T. 1979, Reviews of Geophysics and Space Physics, 17, 73
Warren, P. H. 1985, Annual Review of Earth and Planetary Sciences, 13, 201
Warren, P. H. 2001, J. Geophys. Res., 106, 10101
Warren, P. H., & Humphrys, T. L. 2003, in Lunar and Planetary Institute Science Conference Abstracts, 34, eds. S. Mackwell, & E. Stansbery, 2034
Warren, P. H. 2005, Meteoritics and Planetary Science, 40, 477
Weber, M. 2002, Journal of Luminescence, 100, 35

Wieczorek, M. A., & Phillips, R. J. 1999, Icarus, 139, 246
Wieczorek, M. A., & Phillips, R. J. 2000, J. Geophys. Res., 105, 20417
Wieczorek, M. A., & Zuber, M. T. 2004, Journal of Geophysical Research (Planets), 109, E01009
Wieczorek, M. A., Jolliff, B. L., Khan, A., et al. 2006, Reviews in Mineralogy and Geochemistry, 60, 221
Wilhelms, D. E., McCauley, J. F., & Trask, N. J. 1987, The Geologic History of the Moon, U.S. Geol. Surv. Proc. Paper 1348
Yamashita, N., Hasebe, N., Reedy, R. C., et al. 2010, Geophys. Res. Lett., 37, L10201
Yin, L. I., Trombka, J. I., Adler, I., & Bielefeld, M. 1993, X-ray Remote Sensing Techniques for Geochemical Analysis of Planetary Surfaces, in Remote Geochemical Analysis: Elemental and Mineralogical Composition, eds. C. M. Pieters, & P. A. J. Englert (Cambridge Univ. Press), 199
Yingst, R. A., & Head, J. W., III 1997, Journal of Geophysical Research (Planets), 102, 10909
Zhu, M.-H., Ma, T., & Chang, J. 2010, Planet. Space Sci., 58, 1547
Zhu, M. H., Ma, T., Chang, J., et al. 2012, Goldschmidt Conference Abstracts. Mineralogical Magazine, 2278
Zuber, M. T., Smith, D. E., Lemoine, F. G., & Neumann, G. A. 1994, Science, 266, 1839